

---

# Studying Polymeric Materials with Mesoscopic Models. Focus: Multiscale Properties

---

Max Planck **Graduate Center**   
mit der Johannes Gutenberg-Universität

**Jianrui ZHANG**

Dissertation  
zur Erlangung des Grades eines  
"Doctor rerum naturalium (Dr. rer. nat)"  
der Fachbereiche:  
08-Physik, Mathematik und Informatik,  
09-Chemie, Pharmazie und Gerwissenschaften,  
10-Biologie,  
Universitätsmedizin  
der Johannes Gutenberg-Universität

Angfertigt am Max-Planck-Institut für Polymerforschung  
Mainz, July 2020

**Erstgutachter:**

Prof. Dr. Kurt Kremer

Max-Planck-Institut für Polymerforschung

**Zweitgutachter:**

Prof. Dr. Björn Baumeier

Eindhoven University of Technology

**Datum der mündlichen Prüfung:**

21.09.2020

# Declaration of Authorship

I hereby declare that I wrote the dissertation submitted without any unauthorized external assistance and used only sources acknowledged in the work. All textual passages which are appropriated verbatim or paraphrased from published and unpublished texts as well as all information obtained from oral sources are duly indicated and listed in accordance with bibliographical rules. In carrying out this research, I complied with the rules of standard scientific practice as formulated in the statutes of Johannes Gutenberg University Mainz to insure standard scientific practice.

PhD candidate:

---



# Abstract

Mesoscopic models are constructed to accurately describe large-scale features of polymeric systems. Yet many properties, what we call multiscale properties, of polymeric systems are affected by features on both large and small scales. In this thesis, we address selected questions demonstrating what mesoscopic models can do to understand the multiscale properties of polymeric systems.

We employ a model which is typical for mesoscopic simulations and investigate two representative multiscale properties of polymeric systems. The employed mesoscopic model defines polymer architectures with a worm-like chain model. A quadratic functional of local density fields is used to define the non-bonded interactions. The functional-based non-bonded interactions are incorporated into particle-based simulations by using a particle-to-mesh scheme. The model is used as a framework for off-lattice Monte-Carlo simulations.

The first representative multiscale property studied in this thesis is charge transport within emissive active layers of polymeric light-emitting diodes. We compare charge transport in two types of multi-component active layers, which are called blend-based or BCP-based active layers. These two types of active layers contain blends or block copolymers (BCPs) formed by semiconducting and insulating homopolymers or blocks. We use the mesoscopic model to simulate morphologies of active layers under conditions mimicking processing at different temperatures or compositions. Because active layers in PLEDs are usually disordered layers, we identify the disordered morphologies by analyzing structure factors and hysteresis loops. The disordered morphologies of blend-based and BCP-based active layers are characterized and compared through local composition analysis. The properties related to charge transport within two types of active layers are compared through a simple percolation analysis of the morphologies. The influence of mesoscopic description in our model on the properties related to charge transport is discussed. The most important result is that the morphologies near the order-disorder transition in BCP-based layers tend to have stronger local segregation than the equivalent blend-based layers. By linking morphologies with macroscopic electric conductance, we can qualitatively predict through the mesoscopic model that the processing temperature has stronger impact on electric conductance in BCP-based than blend-based layers. The above differences between the two types of layers increase as the relative concentration of insulating polymers (blocks) increases.

Subsequently, we focus on another multiscale property, the behavior of knots in homopolymer melts. We clarify to what extent the mesoscopic model describes the knotting properties. This is investigated by comparing the results obtained from the mesoscopic model with that of a reference bead-spring model. The bead-spring model takes into account the excluded volume around beads and describes the generic structural and conformational features of polymer melts at all length scales. Therefore, one can obtain reliable reference data on knots from the bead-spring model. We consider different reference melts obtained from the bead-spring model, which contain chains with different stiffness and lengths. The mesoscopic model is parameterized to accurately reproduce the mesoscopic features of these reference melts. Then structure and conformational properties of melts generated by our mesoscopic model are discussed on both small and large scales. After that, we compare the knotting properties obtained from two models. Based on the comparison, we further discuss the ability of mesoscopic model to describe the knotting properties of polymer melts. The main conclusion in this study is that mesoscopic models can accurately reproduce the knotting properties of homopolymer melts when the characteristic length scale describing chain stiffness is substantially larger than the size of excluded volume along the backbone of polymer chains.

*Dedicated to my husband*

*Mr. Chao Liu*

*for his moral, continual, unrelenting support...*





# Contents

<b>Declaration of Authorship</b>	<b>iii</b>
<b>Abstract</b>	<b>v</b>
<b>1 Introduction</b>	<b>1</b>
<b>2 Mesoscopic modeling of polymers with soft potentials</b>	<b>7</b>
2.1 Philosophies of coarse-graining . . . . .	7
2.2 Top-down models based on density functional theory . . . . .	12
2.3 Realization in particle-based simulations . . . . .	19
2.4 Simulation method . . . . .	25
2.5 Insights from self-consistent field theory and random phase approximation . . . . .	27
<b>3 Disorderd morphology in blend-/BCP-based PLED</b>	<b>41</b>
3.1 Introduction . . . . .	41
3.2 Model description . . . . .	44
3.2.1 Mapping strategy . . . . .	44
3.2.2 Material-specific parameters and systems studied . . . . .	46
3.2.3 Non-bonded interactions . . . . .	49
3.2.4 Simulation protocol . . . . .	50
3.3 Location of disordered phase . . . . .	52
3.3.1 RPA spinodals . . . . .	52
3.3.2 Order parameters . . . . .	57
3.4 Sub-lattice polymer packing . . . . .	58
3.5 Local composition in blends and BCP . . . . .	59
3.6 Percolation analysis . . . . .	63
3.7 Summary and outlook . . . . .	70
<b>4 When can soft models describe polymer knots?</b>	<b>75</b>
4.1 Introduction . . . . .	75
4.2 Qualitative insights from a free energy model . . . . .	77

4.3	Model description . . . . .	81
4.3.1	The reference bead-spring model . . . . .	81
4.3.2	Mesoscopic model . . . . .	82
	Mapping strategy . . . . .	82
	Non-bonded potential . . . . .	84
	Simulation details . . . . .	85
4.4	Knot detection . . . . .	85
4.5	Structural and conformational properties . . . . .	89
4.6	Properties of knots in mesoscopic models . . . . .	98
4.7	Summary and conclusions . . . . .	104
5	Summary and conclusions	109
	Appendix: Results for dilution 1:2	113
	Acknowledgements	115
	Bibliography	117

# List of Abbreviations

<b>3D</b>	Three-Dimensional
<b>BCP</b>	Block Copolymer
<b>CG</b>	Coarse-Grained
<b>COM</b>	Center of Mass
<b>DBI</b>	Direct Boltzmann Inversion
<b>DFT</b>	Density Functional Theory
<b>FH</b>	Flory-Huggins
<b>LJ</b>	Lennard-Jones
<b>MC</b>	Monte-Carlo
<b>MDMO-PPV</b>	Poly[2-methoxy-5-(3',7'-dimethyloctyloxy)-1,4-phenylenevinylene]
<b>MEH-PPV</b>	Poly[2-methoxy-5-(2-ethylhexyloxy)-1,4-phenylenevinylene]
<b>MF</b>	Mean-Field
<b>MH</b>	Mark and Helfrich
<b>MW</b>	Molecular Weight
<b>ODT</b>	Order-Disorder Transition
<b>PBC</b>	Periodic Boundary Condition
<b>PLED</b>	Polymeric Light-Emitting Diode
<b>PM</b>	Particle-to-Mesh
<b>PMF</b>	Potential of Mean Force
<b>PMMA</b>	Poly(methylmethacrylate)
<b>PPV</b>	Poly(p-phenylene vinylene)
<b>RPA</b>	Random Phase Approximation
<b>WLC</b>	Worm-Like Chain



# Chapter 1

## Introduction

Nowadays, polymeric systems are attracting significant attention of researchers and are central of a wide range of applications<sup>1-4</sup>. Therefore, there is an increasing demand on optimizing and developing novel polymeric systems to achieve better performance<sup>5</sup>. The optimization and development rely on a precise understanding of relationships between material structure, processing conditions, and properties of interest. Simulation methods have been proven to be efficient tools for predicting the structure-process-properties relations<sup>6</sup>, and have been used to provide insights from molecular level for understanding material properties, and guiding the design of novel materials<sup>5,7,8</sup>.

In this thesis, we focus on particle-based simulation methods. They can be classified into atomistic and coarse-grained (CG) simulation methods. The key difference between these two groups of methods is the resolution with which the studied system is represented. Atomistic simulations explicitly consider all the atoms, and each atom is treated as an interacting site. In CG simulations, several atoms or even molecules are represented by a CG bead, which is the interacting site in CG systems. Accordingly, atomistic simulations are necessary when one wants to investigate properties related to atomistic details. For example, atomistic simulations are useful for understanding detailed interactions, e.g., hydrogen bonding and polymer-solvent interactions<sup>9</sup>. Apart from that, atomistic simulations also can be used to generate input information for the parameterization of CG models.

However, the ability of atomistic models to deal with polymeric systems is restricted by their accessible length and time scales<sup>10-16</sup>, which are on the order of  $10^{-10} - 10^{-7}$  m and  $10^{-9} - 10^{-6}$  s<sup>17</sup>, respectively. Polymeric systems

frequently involve length and time scales larger than the scales that are accessible by atomistic models. For instance, when phase behavior of polymer blends is studied, the domain size can be on the order of millimeters, and the formation of such large domains may take several minutes or even hours<sup>18</sup>. To study polymeric systems involving large spatial scales or slow processes, one can use drastically CG mesoscopic models. In this case, large amounts of atoms are lumped into CG beads, and these models are designed to reproduce mesoscopic features or properties of studied systems. The validity of drastic coarse-graining relies on the fact that many properties on large scales reflect the synergy of a large amount of molecules. Therefore one can intuitively expect that microscopic details of molecular architectures and interactions become less important for these properties. Actually, it is already theoretically proven that some properties are controlled by universal laws, which do not depend on microscopic details<sup>19</sup>.

Because of the significantly reduced amount of degrees of freedom, the potentials of mesoscopic models are soft<sup>20–22</sup>. Both the reduced degrees of freedom and soft potentials facilitate the sampling during simulations. Therefore, mesoscopic models can be used to study various problems in polymeric systems<sup>23</sup>. One important application of mesoscopic models is studying the universal equilibrium behavior of polymeric systems<sup>24–27</sup>, especially of systems containing molecules with complex architectures<sup>28,29</sup>. Besides, benefiting from the efficiency of mesoscopic models, one can simulate systems on experimental scales or under various experiment-relevant conditions<sup>30,31</sup>. Then we can gain important insights for interpreting experiments, based on a molecular-level description provided by mesoscopic simulations<sup>24</sup>. One can also use these models to investigate the dynamical questions related to the phase formation or non-equilibrium phenomena in polymeric systems<sup>32–34</sup>.

As researchers apply mesoscopic models to study a broader range of polymeric systems, new challenges arise. One important challenge is that, the ability of mesoscopic models to describe multiscale properties in polymeric systems is unclear. The so-called multiscale properties do not simply reflect a synergy of a large amount of molecules, but are determined by phenomena on multiple scales. Namely, the effect of microscopic features can propagate to the behavior of these properties on mesoscopic and even macroscopic scales. However, mesoscopic models always provide simplified description on small scales. For instance, the local liquid structure in mesoscopic models is very crude. Motivated by this challenge, we study in this thesis two topics

that involve multiscale properties. By employing a model which is typical for mesoscopic simulations, we want to provide some useful insights for understanding the ability of mesoscopic models to describe these properties. The first topic deals with an important technological application. The other topic focuses more on the mesoscopic modeling itself and is of significant fundamental and methodological interest.

In the first topic, we consider a typical organic electronic device, the polymeric light-emitting diode (PLED). A PLED<sup>35</sup> is formed by several functional layers sandwiched between two electrodes. The main layer is the emissive active layer containing semiconducting polymers, within which the light is generated through a radiative recombination of electrons and holes<sup>36</sup>. The prerequisites for this recombination<sup>37</sup> are the injection and transport of charge carriers (electrons and holes). Frequently, it is the transport of charge carriers within active layers which significantly influences the performance of PLEDs<sup>38,39</sup>.

The charge transport within active layers is affected by features on multiple scales. The materials forming active layers of PLEDs are normally in amorphous phase. The charge transport then operates via the move of charge carriers along the chains and the transfer of charge carriers between adjacent chains<sup>40</sup>. The charge transport along or between chains is highly influenced by the fine microscopic features within active layers, e.g., chemical details, local molecular packing<sup>41</sup>. Besides, to obtain conductive active layers, there should be a mesoscopic, or even macroscopic network of pathways that allows the charge carriers to travel from one side of active layers to the other. The structure of this network of pathways highly depends on the mesoscopic or macroscopic distribution of semiconducting molecules, or equivalently morphology, within the active layer.

Having understood that charge transport within active layers is a multiscale property, we design a study of multi-component active layers, which contain amorphous mixtures of semiconducting and insulating polymers. Based on a mesoscopic model, we first simulate the morphologies within active layers on experimental scales. Then the charge transport within active layers is studied based on these morphologies. However, the local liquid structure within these morphologies is simplified. Therefore, we cannot extract from the morphologies the necessary information<sup>41</sup>, e.g., reorganization energy, electronic coupling elements, site energies, etc., for considering the local

move and transfer of charge carriers through rigorous kinetic Monte-Carlo simulations<sup>42</sup>. Instead, we describe the move and transfer of charge carriers on local scales through a simple phenomenological transport model. Based on the simulated morphologies and the simplified description of local charge transport, we are able to study the network of pathways within active layers. The active layers with different dilutions and annealing temperatures are considered, mimicking layers processed under different conditions in real experiments. The influence of the coarse representation of polymer chains on the results is discussed.

In the second topic, we focus on knotting properties of polymer melts. In our daily life, we routinely encounter knots in ropes and cables. Within the microscopic scales, macromolecules also frequently form knots and these knotted molecules have attracted increasing interest from scientists in different fields<sup>43</sup>. For example, it is of interest for polymer physicists to understand the effect of knots on conformational and dynamical properties of polymers<sup>44,45</sup>.

Since the first simulation of knots formed in closed polymer chains conducted by Vologodskii and coworkers in 1974<sup>46</sup>, most of simulations of knots formed in polymers are restricted to single chain systems. Simulation of knotting behavior in many-chain polymeric systems are sparse. There is only one recent study<sup>47</sup> which investigates the knotting behavior in homopolymer melts. One of the reasons hindering the investigation of knotting properties in many-chain polymeric systems is the limited computational efficiency of available models. Knot formation in polymeric systems is a rare phenomenon and occurs more frequently in longer chains<sup>47</sup>. Therefore, to study knotting properties in many-chain systems, one needs to simulate large systems containing long chains, and consequently computational efficient models are necessary, e.g., mesoscopic models. However, the ability of mesoscopic models to describe knotting properties in these systems is unclear. This is because the knotting behavior in many-chain polymeric systems is influenced by factors on both local and mesoscopic scales<sup>47,48</sup>. For the moment, one has to employ models reproducing key features on both local and mesoscopic scales, e.g., hard-core bead-spring model, to study knotting behavior in many-chain polymeric systems. The low computational efficiency of these models imposes restrictions on the systems that one can simulate.



To understand how well the mesoscopic models describe the knotting properties in many-chain systems, we focus on homopolymer melts. Benefiting from earlier simulations where the knotting properties of polymer melts have already been analyzed by using a hard-core bead-spring model<sup>47</sup>, we generate mesoscopically equivalent melts with a typical mesoscopic model. The knotting properties obtained from the mesoscopic model are compared with reference data. Several reference melts containing chains with different lengths and stiffness are considered.

Studying knotting properties of polymer melts with a model that is typical for mesoscopic simulations is interesting from a fundamental point of view. After we understand whether, or under which conditions mesoscopic models reproduce the knotting behavior of polymer melts, we can use mesoscopic models to address various open questions related to behavior of knots in different multi-chain systems.

The content of this thesis is organized as follows. In Chapter 2, we first introduce general concepts, definitions, and technical details of our modeling and simulations. The studies of the first and second topic are presented in Chapter 3 and 4, respectively. In both chapters, after providing a detailed introduction to the topic, the parameterization of our mesoscopic model is discussed. Before the discussions of multiscale properties, other properties or observables which are necessary for the interpretation of results are analyzed. Chapter 5 provides a short summary.



## Chapter 2

# Mesoscopic modeling of polymers with soft potentials

## 2.1 Philosophies of coarse-graining

The essential concept of coarse-graining is to focus on only a small number of relevant molecular features and ignore unnecessary atomistic details<sup>49,50</sup>. Therefore, coarse-grained (CG) models replace one or more atoms<sup>51–54</sup> with an effective large particle. The process of replacing groups of atoms into large particles, also called CG sites, is named "mapping-procedure"<sup>55–57</sup>. Given an atomistic configuration, a mapping scheme  $\mathbf{M} = (\mathbf{M}_1, \dots, \mathbf{M}_{N_{\text{CG}}})$  defines coordinates of  $N_{\text{CG}}$  sites from coordinates of the grouped atoms.  $\mathbf{M}_I$  scheme defines coordinate of the  $I$ -th CG site  $\mathbf{R}_I$ ,  $I \in [1, N_{\text{CG}}]$ . If  $I$ -th CG site represents  $m_I$  atoms with coordinates  $\mathbf{r}_{li}$ ,  $i \in [1, m_I]$ , then  $\mathbf{R}_I = \mathbf{M}_I(\mathbf{r}_{I1}, \dots, \mathbf{r}_{Im_I})$ .  $\mathbf{M}_I(\mathbf{r}_{I1}, \dots, \mathbf{r}_{Im_I})$  is typically a linear combination of  $\mathbf{r}_{li}$ , i.e.  $\mathbf{M}_I(\mathbf{r}_{I1}, \dots, \mathbf{r}_{Im_I}) = \sum_{i=1}^{m_I} c_{li} \mathbf{r}_{li}$ . Here the value of coefficients  $c_{li}$  are constant and positive. Generally, coefficients  $c_{li}$  are defined in a way that the position of  $I$ -th CG site is the center of mass or geometry of the grouped  $m_I$  atoms<sup>56</sup>.  $N_{\text{CG}}$  mapped CG sites specify a CG configuration. Notice that several atomistic configurations may be mapped onto one single CG configuration.

The strategy for choosing a mapping scheme, such as how many atoms should be combined into one CG site and how many types of CG sites are needed, depends on studied systems and properties. Nonetheless, the mapping strategy is, to some extent, flexible. For example, one CG site in a CG representation of a polymeric system can represent one carbon atom with its

bonded hydrogen atoms<sup>58</sup>, one repeat unit (several carbon atoms along backbone)<sup>59</sup>, or even an entire molecule<sup>60</sup>. The flexibility of mapping strategy provides more possibilities for describing complex systems and processes on large length or time scales<sup>61</sup>.

Having defined the CG representation of a target atomistic system, the potential between CG sites can be formally defined from the framework of statistical mechanics using the concept of the potential of mean-force (PMF)<sup>62,63</sup>. Considering that one mapped CG configuration corresponds to several configurations in the atomistic model, the probability of observing a CG configuration is equal to the sum of probabilities of observing corresponding atomistic configurations. Accordingly, we can write,

$$P_{\text{CG}}(\{\mathbf{R}_I\}) = \int P_{\text{AT}}(\{\mathbf{r}_i\}) \delta(\mathbf{M}(\{\mathbf{r}_i\}) - \{\mathbf{R}_I\}) d\{\mathbf{r}_i\} \quad (2.1)$$

with  $\{\mathbf{R}_I\} = \{\mathbf{R}_1, \dots, \mathbf{R}_{N_{\text{CG}}}\}$  denotes a CG configuration and is described through the collection of all the coordinates of CG sites  $\mathbf{R}_I$  in the CG configuration. Similarly,  $\{\mathbf{r}_i\}$  denotes an atomistic configuration described by all the coordinates of atoms  $\mathbf{r}_i$  in the atomistic configuration.  $P_{\text{CG}}(\{\mathbf{R}_I\})$  and  $P_{\text{AT}}(\{\mathbf{r}_i\})$  is the probability of observing the configuration  $\{\mathbf{R}_I\}$  or  $\{\mathbf{r}_i\}$  in the CG or atomistic system, respectively. The definitions of configurational probabilities  $P_{\text{CG}}(\{\mathbf{R}_I\})$  and  $P_{\text{AT}}(\{\mathbf{r}_i\})$  in the canonical ensemble are,

$$P_{\text{CG}}(\{\mathbf{R}_I\}) = \frac{e^{-\beta U_{\text{CG}}(\{\mathbf{R}_I\})}}{Z_{\text{CG}}}, \quad P_{\text{AT}}(\{\mathbf{r}_i\}) = \frac{e^{-\beta U_{\text{AT}}(\{\mathbf{r}_i\})}}{Z_{\text{AT}}} \quad (2.2)$$

where  $\beta = 1/k_{\text{B}}T$ .  $U_{\text{AT}}(\{\mathbf{r}_i\})$  is the potential used in the atomistic model and  $U_{\text{CG}}(\{\mathbf{R}_I\})$  is the PMF for CG configuration  $\{\mathbf{R}_I\}$ .  $Z_{\text{AT}}$  and  $Z_{\text{CG}}$  stands for the partition function defining total number of states for an atomistic and CG system, respectively. From eqs. 2.1 and 2.2, we can find the potential of mean force  $U_{\text{CG}}(\{\mathbf{R}_I\})$  as below:

$$U_{\text{CG}}(\{\mathbf{R}_I\}) = -k_{\text{B}}T \ln \int e^{-\beta U(\{\mathbf{r}_i\})} \delta(\mathbf{M}(\{\mathbf{r}_i\}) - \{\mathbf{R}_I\}) d\{\mathbf{r}_i\} + C \quad (2.3)$$

where  $C = \ln(Z_{\text{CG}}/Z_{\text{AT}})$  and  $C$  is a constant number. For the reason that partition functions  $Z_{\text{CG}}$  and  $Z_{\text{AT}}$  are fixed values at a given thermodynamic state, as defined by the parameters of canonical ensemble.

The CG model based on PMF can exactly reproduce all structural properties of the mapped atomistic model that can be observed within the accessible

length-scales of the CG model. However, eq. 2.3 is a configuration-dependent function. For most systems, it is impossible to evaluate the integral and calculate  $U_{\text{CG}}(\{\mathbf{R}_I\})$ . In practice, we can only employ certain approximations to PMF<sup>55,64–68</sup>. Up to now, a variety of strategies defining functions approximating PMF in CG models are developed for different systems and questions. Due to the diversity of these strategies, it is not easy to classify them into different categories. One conventional classification of these modeling strategies includes two types, "bottom-up" and "top-down"<sup>22,56,69</sup>. One considers CG models as "bottom-up" models when they are parameterized through microscopic information obtained from systems with finer resolutions<sup>65,67,70–72</sup>, e.g., classic atomistic models. In contrast, "top-down" models are tailored to reproduce certain macroscopic information<sup>73–77</sup>, such as structural, dynamic, or thermodynamic properties. Though it should be noted that the boundary between "bottom-up" and "top-down" models is becoming increasingly blurred because the number of CG models combining both approaches is increasing. The models used in this thesis are constructed with a "top-down" approach. To motivate this choice, we summarize these two approaches, "bottom-up" and "top-down", in the next paragraphs.

The simplest and most straightforward method for constructing "bottom-up" models is direct Boltzmann inversion (DBI)<sup>55,78</sup>. It can be used to derive both bonded and non-bonded potentials in CG models.

DBI defines bonded potentials in CG models such that the conformational statistics of molecules is the same as reference atomistic models. The conformation of molecules is frequently characterized by their internal degrees of freedom, including bond length  $r$ , bending angle  $\theta$ , and torsion angle  $\phi$ . Assuming that different degrees of freedom are uncorrelated, one can define independent probability distributions  $P_{\text{CG}}(r, T)$ ,  $P_{\text{CG}}(\theta, T)$ ,  $P_{\text{CG}}(\phi, T)$ . Here  $T$  is temperature, through which we emphasize that the distributions are temperature-dependent. These distributions can be obtained by sampling reference atomistic configurations according to the given mapping scheme. Then one obtains a bonded potential for individual degree of freedom by inverting Boltzmann distribution functions,

$$\begin{aligned}
 U_{\text{CG}}(r, T) &= -k_{\text{B}}T \ln \frac{P_{\text{CG}}(r, T)}{r^2} + C_r \\
 U_{\text{CG}}(\theta, T) &= -k_{\text{B}}T \ln \frac{P_{\text{CG}}(\theta, T)}{\sin(\theta)} + C_\theta \\
 U_{\text{CG}}(\phi, T) &= -k_{\text{B}}T \ln P_{\text{CG}}(\phi, T) + C_\phi
 \end{aligned} \tag{2.4}$$

where  $C_r$ ,  $C_\theta$ , and  $C_\phi$  are constant numbers shifting minimum of potentials to zero. Importantly, for CG models containing separated bonded and non-bonded potentials, the above distributions should be sampled from single atomistic molecules without non-bonded interactions to avoid double counting of long range intra-chain interactions<sup>79–82</sup>.

Similarly, nonbonded potentials  $U_{\text{CG,nb}}(r)$  are obtained from Boltzmann inverse of given radial distributions  $g(r)$  sampled from atomistic models,

$$U_{\text{CG,nb}}(r) = -k_B T \ln g(r) \quad (2.5)$$

However, the above potential can only reproduce precisely  $g(r)$  for highly diluted systems<sup>83</sup>. Otherwise, the radial distribution in CG models based on  $U_{\text{CG,nb}}(r)$  deviates from target  $g(r)$  due to strong correlations between different types of interactions. In this case, the iterative Boltzmann inversion method<sup>55</sup> is needed, which optimizes  $U_{\text{CG,nb}}(r)$  through an iteration scheme,

$$U_{\text{CG,nb}}^{i+1}(r) = U_{\text{CG,nb}}^i(r) + k_B T \ln \frac{g_i(r)}{g(r)} \quad (2.6)$$

where  $i$  indicates iterative step and  $g_i(r)$  is the radial distribution in CG models based on potential  $U_{\text{CG,nb}}^i(r)$  at step  $i$ .

It should be noted that  $g(r)$  also depends on the thermodynamic state, e.g., temperature, pressure, composition, etc. At a given state the pair potential, which exactly reproduces the target radial distribution, is unique<sup>84</sup>. Though there might be other pairwise potentials resulting in similar radial distributions with hardly noticeable errors. Hence it is useful to consider additional constraints to  $U_{\text{CG,nb}}(r)$ . For example, one can refine  $U_{\text{CG,nb}}(r)$  in a way that it also reproduces other thermodynamic properties<sup>55,65,85</sup>, such as pressure, compressibility, etc.

It can be seen that "bottom-up" models are always state-dependent<sup>86</sup>. This means that a "bottom-up" model may not be applicable to a state point different than the state chosen for the construction. As a result, it is a challenging task for "bottom-up" models to describe phenomena involving variation of composition, density, or temperature<sup>69,87</sup>. Besides, the construction of "bottom-up" models can be restricted by difficulties in developing atomistic models for complex systems, where the necessary microscopic information for model construction is unknown. Moreover, the inaccuracy of "bottom-up"

potentials increases as the CG model becomes cruder. Therefore, "bottom-up" approaches are not suitable for the studies involved in this thesis, where we want to simulate large systems or phase behavior of complex systems.

As an alternative, one can manually insert desired macroscopic properties into CG models through "top-down" approaches<sup>31,88,89</sup>. These approaches are valid due to the universality in long-wavelength behavior of polymeric systems, which means that some properties are described on large scales by universal laws, and the microscopic details are encapsulated into numerical prefactors of these generic expressions. Consequently, CG models can qualitatively reproduce these properties if their potentials describe the relevant features entering the universal laws<sup>74</sup>.

Accordingly, "top-down" models frequently employ drastically coarse-grained representations. Their potentials contain only minimal interactions describing relevant features of desired macroscopic properties. The forms of these interactions are typically constructed simply according to physical principles or intuitions. Therefore, the resulting "top-down" models are usually generic and can represent a class of materials. These models are very useful for understanding general physical concepts of polymeric systems. For example, pioneering studies of polymer dynamics with a generic bead-spring model<sup>51</sup> have validated the Rouse and tube model. A single "top-down" model can be used to address a broad range of questions. Matsen and Schick<sup>90</sup> predicted the universal phase diagram of flexible di-block copolymers by using a Edwards-type potential<sup>91</sup>, which takes into account only the limited compressibility and immiscibility between distinct species. It should be noted that, in order to quantitatively reproduce desired macroscopic properties, one needs to properly parameterize the potentials of "top-down" models.

Compared with "bottom-up" models, "top-down" models have several advantages. First of all, "top-down" models are beneficial for investigating complex systems since such models simplify the description of complex systems by only focusing on aspects relevant to problems of interest. Furthermore, due to relatively simpler CG representation and potentials, one can perform simulations with "top-down" models on experimental length- and time-scales. For example, a recent study<sup>33</sup> employed a "top-down" model for di-block copolymers and simulated phases in battery electrolytes with

system size on the order of micrometers. Importantly, it is possible to incorporate more chemical specificities into "top-down" models by using sophisticated molecular architectures or interactions<sup>92</sup>. Full atomistic details in "top-down" models also can be restored through hierarchical back-mapping<sup>93-95</sup>, which offers an opportunity for considering samples with atomistic details on experimental length- or time- scales.

## 2.2 Top-down models based on density functional theory

One of the key questions related to the construction of "top-down" models is how to define the interactions so that they reproduce desired macroscopic properties. A convenient way is to define them through functionals of collective variables. This ideal is referred to as a functional-based approach. In functional-based models describing polymeric systems, one separates bonded and non-bonded interactions. The functional-based approach is used to define the non-bonded interactions  $H_{\text{nb}}$ . The bonded interactions  $H_{\text{b}}$  describing the chain connectivity and architectures are defined explicitly based on coordinates of CG sites. In order to illustrate main features of functional-based "top-down" models, it is convenient to consider the configurational part of the partition functions of CG systems in the canonical ensemble,

$$Z(N_{\text{CG}}, V, T) \propto \int d\mathbf{R}_1 \dots d\mathbf{R}_{N_{\text{CG}}} \exp \left[ - \underbrace{f_{\text{b}}(\mathbf{R}_1, \dots, \mathbf{R}_{N_{\text{CG}}})}_{\beta H_{\text{b}}} - \underbrace{\int d\mathbf{r} f_{\text{nb}}[\hat{\xi}(\mathbf{r}; \mathbf{R}_1, \dots, \mathbf{R}_{N_{\text{CG}}})]}_{\beta H_{\text{nb}}} \right] \quad (2.7)$$

where  $\int d\mathbf{R}_1 \dots d\mathbf{R}_{N_{\text{CG}}}$  indicates integration over all possible realizations of coordinates  $\mathbf{R}_{\text{I}}$  in the CG system. Bonded interaction  $H_{\text{b}}$  is a function defined explicitly through coordinates of CG sites  $\mathbf{R}_{\text{I}}$ . Non-bonded interaction  $H_{\text{nb}}$  is a functional of collective variable  $\hat{\xi}(\mathbf{r}; \mathbf{R}_1, \dots, \mathbf{R}_{N_{\text{CG}}})$ . The value of  $\hat{\xi}$  at position  $\mathbf{r}$  is obtained based on coordinates of CG sites  $\mathbf{R}_{\text{I}}$  in CG systems. Therefore



$H_{nb}$  is still a particle-based interaction and the fundamental degrees of freedom in the functional-based models are particle coordinates, not collective variables.

The functional-based approach simplifies the definition of "top-down" models. It is because the interactions derived from functional-based approach allow us to perform mean-field estimations for the thermodynamic properties of CG models<sup>96,97</sup>. The estimated thermodynamic properties are expressed through functions depending on the parameters and forms of functional-based interactions. By comparing with known thermodynamic properties of target systems, one can determine appropriate parameters reproducing desired thermodynamic properties. In some cases, one may find that the defined functional-based interactions are too simple, and the known macroscopic properties cannot be reproduced by simply tuning parameters. Then the definition of interactions needs to be further improved. A conceptual illustration of the procedure defining a functional-based "top-down" model is shown in Fig. 2.1.

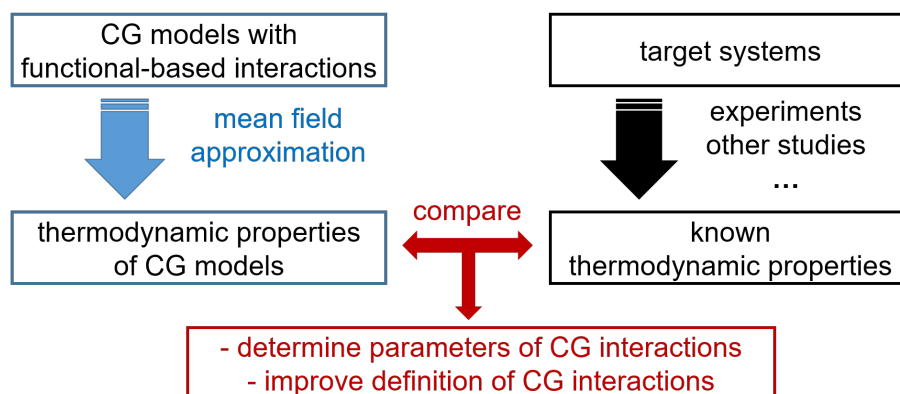


FIGURE 2.1: Procedures for parameterizing and refining a functional-based "top-down" model.

In principle, the determination of functional-based interactions follows the general logic of defining "top-down" models. The interactions are formed by functional-based terms describing necessary features reproducing desired macroscopic properties. There are different functional-based terms that can describe mutual repulsion between CG sites, incompatibility between distinct components or local packing effect, etc. Different questions can be investigated by using different combinations of functional-based terms. Therefore functional-based interactions can be defined in a modular way. The modularity of functional-based interactions provides an opportunity for the

systematic development of these models. Up to now, functional-based models have been developed for a broad range of systems, including homopolymers<sup>98</sup>, polymer blends<sup>99,100</sup>, block-copolymers<sup>101</sup>, liquid-vapor systems<sup>102</sup>, liquid crystals<sup>103,104</sup>, lipid bilayers<sup>105–107</sup>.

The forms of functional-based terms are usually empirically defined. One convenient way of defining these terms is to employ similar forms that are used in theoretical field-based models for polymeric systems<sup>7,91,96</sup>. Among the existing theoretical field-based models, the excess free energy functional of local densities  $F_{\text{DFT,ex}}[\bar{\rho}(\mathbf{r})]$  in classical density functional theory (DFT)<sup>108,109</sup> is frequently used as the template for defining the basic functional-based term describing mutual repulsion between particles, resulting DFT-based models. These models can benefit from vast knowledge accumulated by studies of polymers based on classical DFT<sup>107,110,111</sup>. However, there are several points about DFT-based models that need further clarification.

Firstly, the functional-based terms should not include components associated with translational and conformational entropy. The reason is that  $H_b$  in DFT-based models explicitly defines the molecular architectures. To avoid double counting, one must exclude components associated with translational and conformational entropy in the non-bonded functional-based interactions. This is the reason why the excess free energy functional  $F_{\text{DFT,ex}}[\bar{\rho}(\mathbf{r})]$ , which ignores the contribution of ideal gas in the total intrinsic Helmholtz free energy functional, is chosen as the template. Besides, the functional-based terms and the templating functionals are conceptually different. Because the functional-based terms depend on configuration-dependent instantaneous density fields  $\hat{\rho}(\mathbf{r}; \mathbf{R}_1, \dots, \mathbf{R}_{\text{NCG}})$ , whereas the templating functionals depend on equilibrium average density field  $\bar{\rho}(\mathbf{r})$ . For example, even though  $H_{\text{nb}}$  of a CG system includes a term having same form as  $F_{\text{DFT,ex}}[\bar{\rho}(\mathbf{r})]$ , the excess free energy of the CG system can differ from the value given by  $F_{\text{DFT,ex}}[\bar{\rho}(\mathbf{r})]$ . For this reason, the functional-based interactions can only approximately reproduce the desired macroscopic properties.

In the following, we will introduce typical interactions  $H_b$  and  $H_{\text{nb}}$  used in DFT-based models. The simplest case, binary homopolymer blend, is taken as an example to illustrate the forms of these interactions. Extending the example of homopolymer blends to other multi-component systems is straightforward. In this thesis, we also study di-block copolymer (di-BCP) systems

with same forms of interactions that are used to describe blend systems.

Generic chain models, such as Gaussian chain model, wormlike chain model, are frequently used to define bonded interactions  $H_b$  in drastically CG models. By tuning parameters of these generic bonded interactions, one can retain certain chemical specificity, e.g., end-to-end distance, persistence length, bond length, etc. Developing  $H_b$  from known atomistic chain models is necessary when more chemical details are needed and follows the standard procedure in the "bottom-up" approaches. An example, the DBI method, has been discussed in the section 2.1. Below we only discuss two frequently used generic chain models.

The choice of generic chain models is closely related to the chain structure one wants to describe. To describe a fully flexible chain formed by uncorrelated CG segments, we can use the Gaussian chain model. This model assumes that the bond length  $b_\alpha$  follows Gaussian distribution,

$$P(b_\alpha) = \left( \frac{3}{2\pi a_\alpha^2} \right)^{3/2} \exp \left( -\frac{3b_\alpha^2}{2a_\alpha^2} \right) \quad (2.8)$$

resulting in an average bond length  $\langle b_\alpha \rangle = a_\alpha$ . For chains of springs, the bonded interaction  $H_b$  is defined as,

$$\beta H_{b,\alpha} = \frac{3}{2a_\alpha^2} \sum_{i=1}^{n_\alpha} \sum_{s=1}^{N_\alpha-1} [\mathbf{r}_{\alpha,i}(s+1) - \mathbf{r}_{\alpha,i}(s)]^2 \quad (2.9)$$

where  $\alpha = A, B$  denotes the type of species in the binary blend.  $n_\alpha$  is number of chains of type  $\alpha$ .  $N_\alpha$  is number of beads per chain for chains of type  $\alpha$ .  $\mathbf{r}_{\alpha,i}(s)$  is the coordinate of  $s$ -th CG bead in  $i$ -th chain with type  $\alpha$ . With Gaussian chain model, the local features of polymer chains cannot be correctly described, but one can reproduce properties of chains on large scales, such as mean-squared end-to-end distance  $\langle R_{e,\alpha}^2 \rangle = (N_\alpha - 1)a_\alpha^2$ <sup>112</sup>.

For chains with intrinsic rigidity, we can employ the wormlike chain (WLC) model. WLCs are formed by CG segments with fixed lengths. The bonded interaction  $H_b$  is defined as,

$$\beta H_{b,\alpha} = -\epsilon_\alpha \sum_{i=1}^{n_\alpha} \sum_{s=1}^{N_\alpha-2} \mathbf{u}_{\alpha,i}(s+1) \cdot \mathbf{u}_{\alpha,i}(s) \quad (2.10)$$

here  $\epsilon_\alpha$  is a dimensionless parameter and defines stiffness of  $\alpha$ -type chains.  $\mathbf{u}_{\alpha,i}(s)$  is the unit bond vector along  $s$ -th bond of  $i$ -th chain with type  $\alpha$ .

WLC model can quantitatively reproduce more characteristic length scales of polymer chains than the Gaussian chain model. Many characteristic length scales of polymers are defined in terms of the angular correlation of the bending angle along the polymer backbone, i.e.,  $\langle \cos \theta_\alpha \rangle$ <sup>113</sup>. For WLCs, the angular correlation  $\langle \cos \theta_\alpha \rangle$  can be predicted based on the bonded parameter  $\epsilon_\alpha$ <sup>114</sup>, i.e.,

$$\langle \cos \theta_\alpha \rangle = G(\epsilon_\alpha) \equiv \frac{1 - \epsilon_\alpha^{-1} + e^{-2\epsilon_\alpha} (1 + \epsilon_\alpha^{-1})}{1 - e^{-2\epsilon_\alpha}} \quad (2.11)$$

where  $\theta_\alpha$  is the angle between the neighboring bond vectors of chains with type  $\alpha$ .

Then one can calculate the persistence length  $l_{p,\alpha}$  of WLCs according to its definition,

$$l_{p,\alpha} = g(b_\alpha, \epsilon_\alpha) \equiv b_\alpha / |\ln G(\epsilon_\alpha)| \quad (2.12)$$

The above definition of persistence length is valid for WLCs formed by segments with the same length  $b_\alpha$ . For WLCs containing segments with different lengths, e.g., copolymer chains, one can divide WLCs into parts with same segmental length, and then apply the above equation separately for each part. For the parts with the same  $b_\alpha$ , eq. 2.12 provides a one-to-one relationship between  $l_{p,\alpha}$  and  $\epsilon_\alpha$ . The desired persistence length can be reproduced by using the bonded parameter  $\epsilon_\alpha$  predicted by the eq. 2.12.

Another important characteristic length scale of polymer chains is the mean-squared end-to-end distance  $\langle R_{e,\alpha}^2 \rangle$ . For WLCs formed by segments with the same length  $b_\alpha$ ,  $\langle R_{e,\alpha}^2 \rangle$  is defined as,

$$\langle R_{e,\alpha}^2 \rangle = b_\alpha^2 \sum_{i=1}^{N_\alpha-1} \sum_{j=1}^{N_\alpha-1} \langle \cos \theta_\alpha \rangle^{|i-j|} \quad (2.13)$$

According to eq. 2.11 and the sum of geometric series,  $\langle R_{e,\alpha}^2 \rangle$  can be rewritten as,

$$\begin{aligned} \langle R_{e,\alpha}^2 \rangle &= h(N_\alpha, b_\alpha, \epsilon_\alpha) \equiv \\ &\equiv (N_\alpha - 1) b_\alpha^2 \left[ \frac{1 + G(\epsilon_\alpha)}{1 - G(\epsilon_\alpha)} - \frac{2G(\epsilon_\alpha)}{N_\alpha - 1} \frac{1 - G(\epsilon_\alpha)^{N_\alpha-1}}{(1 - G(\epsilon_\alpha))^2} \right] \end{aligned} \quad (2.14)$$

Then one can reproduce the desired  $\langle R_{e,\alpha}^2 \rangle$  by using the  $\epsilon_\alpha$  predicted by the

above equation. Same as the persistence length, one can also predict the bonded parameter  $\epsilon_\alpha$  for WLCs formed by segments with different lengths by dividing WLCs into several parts.

In addition, because WLCs are formed by segments with fixed lengths, WLC model can conserve the desired bond lengths and contour length  $L_\alpha$ . The contour length  $L_\alpha$  of WLCs with same bond length  $b_\alpha$  is defined as,

$$L_\alpha = f(N_\alpha, b_\alpha) \equiv (N_\alpha - 1)b_\alpha \quad (2.15)$$

It is straightforward to extend the eq. 2.15 to WLCs with different bond lengths.

The ability of reproducing multiple characteristic length scales of polymer chains makes it convenient for WLC model to reproduce the key features of molecular architectures in a flexible way. For example, the same molecular features can be reproduced by conserving either  $L_\alpha$  and  $l_{p,\alpha}$ , or  $L_\alpha$  and  $\langle R_{e,\alpha}^2 \rangle$  of the mapped chains. Though it should be noted that the formulas for  $l_{p,\alpha}$  and  $\langle R_{e,\alpha}^2 \rangle$ , i.e., eqs. 2.12 and 2.14, are only valid for ideal chains. The simulated  $l_{p,\alpha}$  or  $\langle R_{e,\alpha}^2 \rangle$  of interacting WLCs can deviate from the values given by the above equations. Therefore, in order to quantitatively reproduce the desired  $l_{p,\alpha}$  or  $\langle R_{e,\alpha}^2 \rangle$  in multi-chain systems, further refinement of  $\epsilon_\alpha$  is necessary.

For non-bonded interactions  $H_{nb}$ , the minimal interactions describing polymer blends include a mutual repulsive interaction between all CG sites and an interaction describing incompatibility between distinct components. A DFT-based interaction is widely used for describing mutual repulsion between CG sites. It takes the form,

$$\beta F_{\text{rep}}[\hat{\rho}_A(\mathbf{r}), \hat{\rho}_B(\mathbf{r})] = \frac{\kappa}{2\rho_0} \int d\mathbf{r} [\hat{\rho}_A(\mathbf{r}) + \hat{\rho}_B(\mathbf{r})]^2 \quad (2.16)$$

where  $\hat{\rho}_\alpha(\mathbf{r})$  denotes instantaneous local density field of species  $\alpha$  at position  $\mathbf{r}$ . For simplicity, here we adopt a shorter notation for instantaneous density field than  $\hat{\rho}(\mathbf{r}; \mathbf{R}_1, \dots, \mathbf{R}_{N_{\text{CG}}})$  and omit the arguments  $\{\mathbf{R}_I\}$ . The dependence of instantaneous local density field on CG configurations  $\{\mathbf{R}_I\}$  is implicitly included in the hat symbol.  $\rho_0$  is reference density and is usually set to be the average particle density in systems.  $\kappa$  is a finite non-negative coefficient, which controls the strength of compressibility. Lower  $\kappa$  result in

more compressible systems. The form of this interaction is motivated by the second-order expansion of the excess free energy functional in DFT.

The interaction defined in eq. 2.16 is sufficient for a generic description of liquids with limited compressibility. The isothermal compressibility  $\kappa_T$  of a binary homopolymer blend without incompatibility between distinct components can be predicted through a simple mean-field estimation,

$$\frac{1}{k_B T \kappa_T} = \frac{n_A + n_B}{V} + \frac{\kappa}{\rho_0} \bar{\rho}_0^2 \quad (2.17)$$

where  $\bar{\rho}_0 = \sum_{\alpha} n_{\alpha} N_{\alpha} / V$  is the average particle density, with  $V$  denoting the volume of CG system. The detailed discussion on derivation of eq. 2.17 can be found in the section 2.5. Based on eq. 2.17, one can find appropriate value of  $\kappa$  according to desired isothermal compressibility, or evaluate isothermal compressibility of a CG system based on an empirical value of  $\kappa$ . In general, large  $\kappa$  is required in order to achieve realistic isothermal compressibility of polymer liquids<sup>111</sup>, typically found in the range  $10^{-9}$  to  $10^{-10} \text{ Pa}^{-1}$ <sup>115</sup>. However, larger  $\kappa$  result in less compressible systems, and consequently the relaxation time of these systems is longer. Moreover, high  $\kappa$  may lead to additional artifacts. For example, in the simulations based on particle-to-mesh schemes, a high  $\kappa$  enhances the registration of particles at the interfaces of lattice<sup>116</sup> (see section 2.3). Therefore one needs to balance between these aspects when choosing the value of  $\kappa$ .

DFT-based interaction also can capture asymmetries in bead volume. For example, Steinmueller et. al.<sup>117</sup> introduce a prefactor  $\gamma$  to consider different volume of A and B species in polymer blends, and the corresponding  $F_{\text{rep}}[\hat{\phi}_A(\mathbf{r}), \hat{\phi}_B(\mathbf{r})]$  takes the form,

$$\beta F_{\text{rep}}[\hat{\phi}_A(\mathbf{r}), \hat{\phi}_B(\mathbf{r})] = \frac{\kappa \rho_0}{2} \int d\mathbf{r} [(1 - \gamma)\hat{\phi}_A(\mathbf{r}) + (1 + \gamma)\hat{\phi}_B(\mathbf{r}) - 1]^2 \quad (2.18)$$

where instantaneous local volume fraction is defined as  $\hat{\phi}_{\alpha}(\mathbf{r}) = \hat{\rho}_{\alpha}(\mathbf{r}) / \bar{\rho}_0$ . The prefactors  $1 \pm \gamma$  are the normalized average volume of A or B beads. Particularly,  $1 - \gamma = V_{A,0} / V_0$  and  $1 + \gamma = V_{B,0} / V_0$ . Here  $V_{\alpha,0} = 1 / \rho_{\alpha}$  is the average volume of a bead of type  $\alpha$  with average density  $\rho_{\alpha}$ .  $V_0 = 1 / \bar{\rho}_0$  is the average bead volume in the blend system with average density  $\bar{\rho}_0$ . When  $\gamma = 0$ , the interaction defined in eq. 2.18 is equivalent to the form defined in eq. 2.16, where the average volume for the two components is same, i.e.,  $V_{A,0} = V_{B,0} = V_0$ . If  $\gamma > 0$ , the average volume of A segments,  $(1 - \gamma)V_0$ , is

smaller than that of B segments,  $(1 + \gamma)V_0$ .

The interaction describing incompatibility  $F_{\text{mix}}[\hat{\rho}_A(\mathbf{r}), \hat{\rho}_B(\mathbf{r})]$  can be defined based on Flory-Huggins (FH) theory<sup>97,118,119</sup>. The repulsion between distinct species is considered as a energy penalty of contacts between unlike CG sites,

$$\beta F_{\text{mix}}[\hat{\rho}_A(\mathbf{r}), \hat{\rho}_B(\mathbf{r})] = \frac{\chi}{\rho_0} \int d\mathbf{r} \hat{\rho}_A(\mathbf{r}) \hat{\rho}_B(\mathbf{r}) \quad (2.19)$$

The parameter  $\chi$  controls the degree of incompatibility between distinct components, hence it is correlated with thermodynamic conditions, e.g. temperature. In order to model specific thermodynamic conditions, one needs to quantify the state-dependence of  $\chi$  parameter, e.g.  $\chi(T)$ . In the simplest case, the variation of  $\chi$  only reflects enthalpic effects, and a simple  $\sim 1/T$  scaling is expected. However, in drastically coarse-grained systems, a single coarse-grained configuration is underpinned by a large number of averaged-out microstates. In this case,  $\chi$  is only a "bare" parameter of the pairwise interaction<sup>120</sup>, and a nontrivial state-dependence is expected<sup>121–123</sup>.

There also exists other forms of interactions describing the incompatibility. One example of these interactions is given below<sup>124</sup>,

$$\beta F_{\text{mix}}[\hat{\rho}_A(\mathbf{r}), \hat{\rho}_B(\mathbf{r})] = \frac{\chi}{\rho_0} \int d\mathbf{r} [\hat{\rho}_A(\mathbf{r}) - \hat{\rho}_B(\mathbf{r})]^2 \quad (2.20)$$

The two forms of  $F_{\text{mix}}[\hat{\rho}_A(\mathbf{r}), \hat{\rho}_B(\mathbf{r})]$  in eqs. 2.19 and 2.20 both allow us to simulate phase behavior in multi-component systems and provide qualitatively same results. In this thesis, we use the  $F_{\text{mix}}[\hat{\rho}_A(\mathbf{r}), \hat{\rho}_B(\mathbf{r})]$  defined in eq. 2.19, which is the typical form used in field-based models, and can be directly linked with FH description.

## 2.3 Realization in particle-based simulations

In order to perform particle-based simulations with interactions discussed in the previous section, one must define an operator projecting coordinates in a CG configuration onto values of the instantaneous density fields at position  $\mathbf{r}$ , i.e., define  $\hat{\rho}_\alpha(\mathbf{r})$ . There are two types of schemes for defining  $\hat{\rho}_\alpha(\mathbf{r})$  in particle-based systems, particle-to-mesh (PM) schemes and schemes based on density distribution functions. In the following, these two types of schemes will be

discussed based on the non-bonded interaction used in this thesis,

$$\beta H_{\text{nb}} = \frac{\kappa}{2\rho_0} \int d\mathbf{r} [\hat{\rho}_A(\mathbf{r}) + \hat{\rho}_B(\mathbf{r})]^2 + \frac{\chi}{\rho_0} \int d\mathbf{r} \hat{\rho}_A(\mathbf{r}) \hat{\rho}_B(\mathbf{r}) \quad (2.21)$$

The first term corresponds to an isotropic repulsion defined in eq. 2.16, and the second term takes the form of interaction describing incompatibility in eq. 2.19.

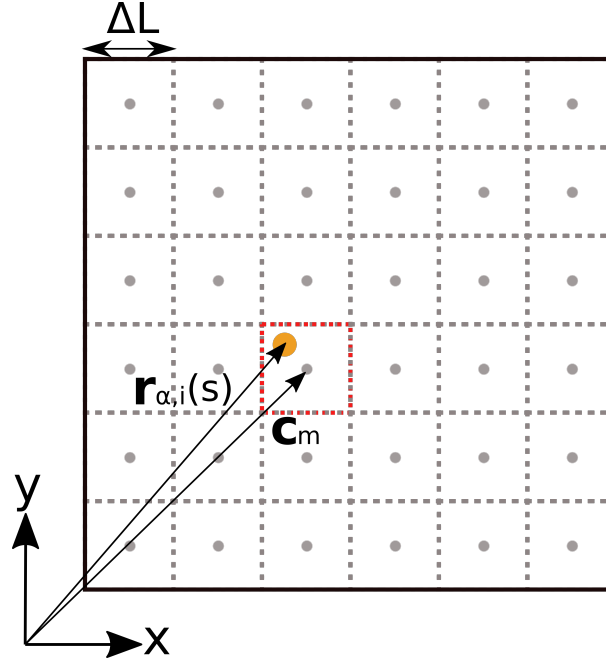


FIGURE 2.2: Illustration of the particle-to-mesh scheme for a 2D system.

PM schemes<sup>125,126</sup> discretize continuum space by a lattice and approximate the instantaneous local density fields with densities at lattice nodes. A schematic drawing for a 2D system is shown in Figure 2.2. The system is discretized into a lattice with spacing  $\Delta L$ . Then we can immediately know the number of nodes  $N_{\text{node}}$  and the position of each node  $\mathbf{c}_m$ ,  $m \in [1, N_{\text{node}}]$ . Given a CG configuration, the instantaneous local density at node  $\mathbf{c}_m$  is defined as,

$$\hat{\rho}_\alpha(\mathbf{c}_m) = \frac{1}{C} \sum_{i=1}^{n_\alpha} \sum_{s=1}^{N_\alpha} \Pi[\mathbf{r}_{\alpha,i}(s), \mathbf{c}_m] \quad (2.22)$$

where  $C$  is a constant number which depends on lattice structure. For three-dimensional (3D) cubic lattice,  $C = \Delta L^3$ .  $\Pi[\mathbf{r}_{\alpha,i}(s), \mathbf{c}_m]$  is an assignment function and determines the density contribution from a particle located at  $\mathbf{r}_{\alpha,i}(s)$  to a certain node  $\mathbf{c}_m$ . It is set to be  $\Pi[\mathbf{r}_{\alpha,i}(s), \mathbf{c}_m] \in (0, 1]$  when there is a density contribution from the particle to the node, and is zero otherwise. The



definition of the assignment function must fulfill the normalization condition, i.e.  $\sum_{m=1}^{N_{\text{node}}} \Pi[\mathbf{r}_{\alpha,i}(s), \mathbf{c}_m] = 1$ .

In PM schemes, the underlying nodes are only used to calculate instantaneous local densities  $\hat{\rho}_\alpha(\mathbf{c}_m)$  based on a given assignment function, while particles still diffuse in the continuum space. The  $H_{\text{nb}}$  is calculated by substituting  $\hat{\rho}_\alpha(\mathbf{c}_m)$  for  $\hat{\rho}_\alpha(\mathbf{r})$  in eq. 2.21 and replacing integration  $\int d\mathbf{r}$  with a summation over all nodes  $\sum_{m=1}^{N_{\text{node}}} \Delta L^3$ . Then  $H_{\text{nb}}$  takes the following form:

$$\begin{aligned} \beta H_{\text{nb}} = & \frac{\kappa}{2\rho_0\Delta L^3} \left[ \sum_{i=1}^{n_A} \sum_{s=1}^{N_A} \sum_{j=1}^{n_A} \sum_{t=1}^{N_A} U(\mathbf{r}_{A,i}(s), \mathbf{r}_{A,j}(t)) + 2 \sum_{i=1}^{n_A} \sum_{s=1}^{N_A} \sum_{j=1}^{n_B} \sum_{t=1}^{N_B} U(\mathbf{r}_{A,i}(s), \mathbf{r}_{B,j}(t)) \right. \\ & \left. + \sum_{i=1}^{n_B} \sum_{s=1}^{N_B} \sum_{j=1}^{n_B} \sum_{t=1}^{N_B} U(\mathbf{r}_{B,i}(s), \mathbf{r}_{B,j}(t)) \right] + \frac{\chi}{\rho_0\Delta L^3} \sum_{i=1}^{n_A} \sum_{s=1}^{N_A} \sum_{j=1}^{n_B} \sum_{t=1}^{N_B} U(\mathbf{r}_{A,i}(s), \mathbf{r}_{B,j}(t)) \end{aligned}$$

with

$$U(\mathbf{r}_{\alpha,i}(s), \mathbf{r}_{\alpha',j}(t)) = \sum_{m=1}^{N_{\text{cell}}} \Pi[\mathbf{r}_{\alpha,i}(s), \mathbf{c}_m] \Pi[\mathbf{r}_{\alpha',j}(t), \mathbf{c}_m] \quad (2.23)$$

Eq. 2.23 demonstrates that  $H_{\text{nb}}$  based on PM schemes is expressed through a pairwise non-bonded potential  $U(\mathbf{r}_{\alpha,i}(s), \mathbf{r}_{\alpha',j}(t))$ . There is an energy contribution to  $H_{\text{nb}}$  only when two particles,  $\mathbf{r}_{\alpha,i}(s)$  and  $\mathbf{r}_{\alpha',j}(t)$ , are assigned to the same node, in which case  $\Pi[\mathbf{r}_{\alpha,i}(s), \mathbf{c}_m] \Pi[\mathbf{r}_{\alpha',j}(t), \mathbf{c}_m] \neq 0$ . The magnitude of the contribution, i.e., strength of repulsion, is controlled by the ratio  $\kappa/\rho_0\Delta L^3$ , or  $\chi/\rho_0\Delta L^3$ . The lattice space  $\Delta L$ , which defines distances between nodes, can be understood as the range of interactions for particles. There is no strict rules for choosing the value of  $\Delta L$ . Considering that  $\Delta L$  is the smallest physical length-scale in models based on PM schemes,  $\Delta L$  is chosen in an empirical way such that it is not significantly larger than the length-scales that characterize the physical phenomena related to the studied problems. The characteristic length-scales for different studied problems can be the width of the interface in multi-component systems, the length of Kuhn segments describing chain stiffness, Edwards correlation length, etc. On the other hand,  $\Delta L$  determines the average number of interacting particles  $\eta$  for a given system with average density  $\bar{\rho}_0$ , i.e.,

$$\eta = \bar{\rho}_0 \Delta L^3 \quad (2.24)$$

In order to benefit from the close connection between  $H_{\text{nb}}$  and field-based functionals and to parameterize  $H_{\text{nb}}$  based on mean-field estimations, relatively large  $\eta$ , equivalently large  $\Delta L$ , are preferred. However, for specific purposes, it is also possible to employ a small  $\eta$ <sup>30</sup>. In this thesis, both small and large  $\eta$  will be considered, see chapters 3 and 4.

The assignment function is another important element in PM schemes and enters eq. 2.23 explicitly. There are different ways to define the assignment function  $\Pi[\mathbf{r}_{\alpha,i}(s), \mathbf{c}_m]$ , and the definition of  $\Pi[\mathbf{r}_{\alpha,i}(s), \mathbf{c}_m]$  has a direct impact on the behavior of the system. The simplest and also the most popular assignment function is zeroth-order  $\Pi_0[\mathbf{r}_{\alpha,i}(s), \mathbf{c}_m]$ . It assigns each particle to only one node, which is the nearest to the particle. The definition is as follows,

$$\Pi_0[\mathbf{r}_{\alpha,i}(s), \mathbf{c}_m] = \begin{cases} 1 & \text{for } -\Delta L/2 \leq d_v < \Delta L/2 \\ 0 & \text{otherwise} \end{cases} \quad (2.25)$$

where  $d_v = |\mathbf{r}_{\alpha,i}(s) - \mathbf{c}_{m,v}|$ , ( $v = x, y, z$ ) are the distances between a particle located at  $\mathbf{r}_{\alpha,i}(s)$  and a node at  $\mathbf{c}_m$  along  $x, y, z$  directions. Obviously,  $\Pi_0[\mathbf{r}_{\alpha,i}(s), \mathbf{c}_m]$  may assign many particles to a single node. As shown in fig. 2.2, every particle within the cell marked red will be fully assigned to the node  $\mathbf{c}_m$ . These particles in the same cell are regarded as overlapping particles, because they can move freely and overlap with each other in that cell without changing the  $H_{\text{nb}}$ . The overlaps lead to unrealistic liquid structure on length-scales smaller than  $\Delta L$ , which has no physical significance. It is for this reason that  $\Delta L$  is the smallest physical length-scale in CG models based on PM schemes.

It should be emphasized that the overlaps between CG site, i.e., softness of potentials, also exist in mesoscopic models with traditional pairwise potentials. In fact, softness is a natural outcome of projecting multiple microstates into a drastically coarse-grained configuration<sup>127</sup>. This is because the atomistic structures underlying CG sites can interdigitate with each other without violating the hard excluded volume of atoms. Softness in mesoscopic models can substantially reduce the relaxation time of polymers and further expand the length- and time-scales that one can explore. Yet softness indeed results in unrealistic liquid structure on length-scales smaller than the range of soft potentials, e.g.,  $\Delta L$  in models based on PM schemes. Realistic liquid structure on the scale of CG units can be reproduced when soft models are developed in a systematic and complex way, e.g., blob-based models<sup>128,129</sup>.

Besides, CG models based on PM schemes are translationally non-invariant. Namely,  $H_{\text{nb}}$  is non-invariant after the whole system makes a translational movement with respect to the fixed lattice. The translationally non-invariant nature of PM schemes induces registration problems at lattice cells and consequently anisotropy. This can be seen from non-uniform distribution of particles within the cells. It has been suggested that the registration with lattice can be reduced by using higher-order assignment functions<sup>130</sup>. However, the implementation of higher-order assignment functions is more computationally demanding, because higher-order assignment functions associate each particle with multiple nodes. Additionally, higher-order assignment functions lead to the problem of self-interactions. By definition, self-interactions are included in  $H_{\text{nb}}$  defined in eq. 2.23. For the zeroth-order assignment function, the contribution of self-interactions is a constant energy off-set, which does not change the behavior of systems. However, the self-interactions in  $H_{\text{nb}}$  based on higher-order assignment functions are complex functions depending on particle coordinates<sup>131</sup>, which must be subtracted. Otherwise, the registration problem will be enhanced<sup>131</sup> compared to models based on  $\Pi_0[\mathbf{r}_{\alpha,i}(s), \mathbf{c}_m]$ .

In this thesis, it is sufficient for us to use the simple zeroth-order assignment function. We implement the PM scheme based on the zeroth-order assignment function into a standard Monte-Carlo algorithm<sup>132</sup>. Depending on the studied problems, we can employ both local and non-local moves, such as flip<sup>133,134</sup>, reptation<sup>135,136</sup> (details see section 2.4). With the help of PM schemes, it is convenient to calculate energy change after each move in Monte-Carlo simulations, because one only needs to consider the energy change at a few affected nodes. For example, the number of affected nodes after a flip move is either zero or two. In contrast, in models with classic pairwise potentials, one needs to construct neighbor list containing positions of interacting particles for every particle. During simulations, the neighbor lists need to be updated after every single step, and then one calculates energy change by considering all the particles in the affected lists. This is the most expensive part in simulations based on classic pairwise potentials. The advantage of PM schemes becomes more pronounced when one needs to simulate systems containing a large number of particles. Therefore PM schemes are important tools for simulating large or dense systems.

Instead of approximating instantaneous local density  $\hat{\rho}_\alpha(\mathbf{r})$  with densities at discretized nodes, we can also define  $\hat{\rho}_\alpha(\mathbf{r})$  in continuum space to retain

the translational invariance and isotropicity. This approach<sup>92,103</sup> assigns a density distribution function  $W(\mathbf{r}_{\alpha,i}(s) - \mathbf{r})$  to each particle with coordinate  $\mathbf{r}_{\alpha,i}(s)$ . The instantaneous local density at position  $\mathbf{r}$  is the total contribution of all the particles in the system,

$$\hat{\rho}_\alpha(\mathbf{r}) = \sum_{i=1}^{n_\alpha} \sum_{j=1}^{N_\alpha} W(\mathbf{r}_{\alpha,i}(s) - \mathbf{r}) \gamma_{\alpha,i}(s) \quad (2.26)$$

Similar to the assignment function in PM schemes, the density distribution function  $W(\mathbf{r}_{\alpha,i}(s) - \mathbf{r})$  should be normalized so that the contribution of each particle to the whole space is unity,

$$\int d\mathbf{r} W(\mathbf{r}_{\alpha,i}(s) - \mathbf{r}) = 1 \quad (2.27)$$

The non-bonded interaction  $H_{\text{nb}}$  in eq. 2.21 can be accordingly rewritten as,

$$\begin{aligned} \beta H_{\text{nb}} = & \frac{\kappa}{2\rho_0} \left[ \sum_{i=1}^{n_A} \sum_{s=1}^{N_A} \sum_{j=1}^{n_A} \sum_{t=1}^{N_A} u(|\mathbf{r}_{A,i}(s) - \mathbf{r}_{A,j}(t)|) + 2 \sum_{i=1}^{n_A} \sum_{s=1}^{N_A} \sum_{j=1}^{n_B} \sum_{t=1}^{N_B} u(|\mathbf{r}_{A,i}(s) - \mathbf{r}_{B,j}(t)|) \right. \\ & \left. + \sum_{i=1}^{n_B} \sum_{s=1}^{N_B} \sum_{j=1}^{n_B} \sum_{t=1}^{N_B} u(|\mathbf{r}_{B,i}(s) - \mathbf{r}_{B,j}(t)|) \right] + \frac{\chi}{\rho_0} \sum_{i=1}^{n_A} \sum_{s=1}^{N_A} \sum_{j=1}^{n_B} \sum_{t=1}^{N_B} u(|\mathbf{r}_{A,i}(s) - \mathbf{r}_{B,j}(t)|) \end{aligned}$$

with

$$u(|\mathbf{r}_{\alpha,i}(s) - \mathbf{r}_{\alpha',j}(t)|) = \int d\mathbf{r} W(\mathbf{r}_{\alpha,i}(s) - \mathbf{r}) W(\mathbf{r}_{\alpha',j}(t) - \mathbf{r}) \quad (2.28)$$

Here  $u(|\mathbf{r}_{\alpha,i}(s) - \mathbf{r}_{\alpha',j}(t)|)$  is a pairwise potential and physically corresponds to the overlapping volume between a pair of density distributions. The form of  $u(|\mathbf{r}_{\alpha,i}(s) - \mathbf{r}_{\alpha',j}(t)|)$  can be found analytically for certain density distribution functions  $W(\mathbf{r}_{\alpha,i}(s) - \mathbf{r})$ . In top-down models,  $W(\mathbf{r}_{\alpha,i}(s) - \mathbf{r})$  are usually defined through simple generic forms, assuming spherical uniform or Gaussian distributions. More advanced distributions are necessary for studying asymmetric particles e.g., ellipsoidal particles.

For most systems, a uniform distribution function is sufficient to describe pairwise interactions and is also computationally convenient<sup>92,131</sup>. The corresponding pairwise potential takes the form<sup>131</sup>,

$$u(r) = \begin{cases} \frac{3}{8\pi\sigma^3} \left(2 + \frac{r}{2\sigma}\right) \left(1 - \frac{r}{2\sigma}\right)^2 & \text{for } r \leq 2\sigma \\ 0 & \text{otherwise} \end{cases} \quad (2.29)$$

where  $r = |\mathbf{r}_{\alpha,i}(s) - \mathbf{r}_{\alpha',j}(t)|$ .  $\sigma$  is the radius of spherical density distribution and the range of interactions is  $2\sigma$ . The magnitude of  $\sigma$  can be chosen to provide reasonable number of interacting particles, or to reproduce the size of underlying grouped atoms.

Although the schemes based on density distribution functions retain the translational invariance and isotropicity, the computational cost is much higher than that of PM schemes. Normally a cell list<sup>83</sup> is required to accelerate simulations using schemes based on density distribution functions.

## 2.4 Simulation method

All mesoscopic systems in this thesis are simulated by using off-lattice Monte-Carlo (MC) simulation method<sup>137</sup>. MC simulations sample the space of microstates based on the use of random numbers. By averaging over the sampled microstates one can estimate the ensemble averages. A frequently used method to sample microstates is Metropolis method<sup>138</sup>. It tries to change the microstate by randomly moving one or a few beads, and then decides whether to accept or reject the new microstate according to certain acceptance criterion.

The changes in the microstate are attempted by MC "moves". The moves should be employed in such a way that the detailed balance and ergodicity are satisfied. Detailed balance<sup>83</sup> means in equilibrium the average probability of moving from microstate  $i$  to microstate  $j$ ,  $P(i \rightarrow j)$ , is equal to the probability of the reverse move  $P(j \rightarrow i)$ . The probability  $P(i \rightarrow j)$  is the product of the equilibrium probability of microstate  $i$   $P_{\text{eq}}(i)$  and the transition probability from  $i$  to  $j$ ,  $W(i \rightarrow j)$ .  $P(j \rightarrow i)$  is defined in the same way, i.e.,  $P(j \rightarrow i) = P_{\text{eq}}(j)W(j \rightarrow i)$ . Hence the detailed balance implies the following equation,

$$P_{\text{eq}}(i)W(i \rightarrow j) = P_{\text{eq}}(j)W(j \rightarrow i) \quad (2.30)$$

"Ergodicity"<sup>83</sup> means every microstate of the system can be generated by one or more moves.

In the following chapters, we employ two classic moves for polymeric systems, i.e., crankshaft<sup>139,140</sup> and reptation<sup>141</sup> moves. As shown in Fig. 2.3a, crankshaft move, which is also known as flip move, rotates a single bead around the axis defined by the two neighboring beads. The rotation angle is randomly chosen from the interval  $[0, 2\pi]$ . For chain ends, the rotation axis is defined by the next nearest bond (see Fig. 2.3b). The reptation move is illustrated in Fig. 2.3c. It removes one bead from one chain end and adds one bead to the other end. The reptation can be employed in a biased way, meaning the new bead is not randomly added to the chain end, but is added by taking into account certain distributions, e.g., distributions determined by bonded potential.

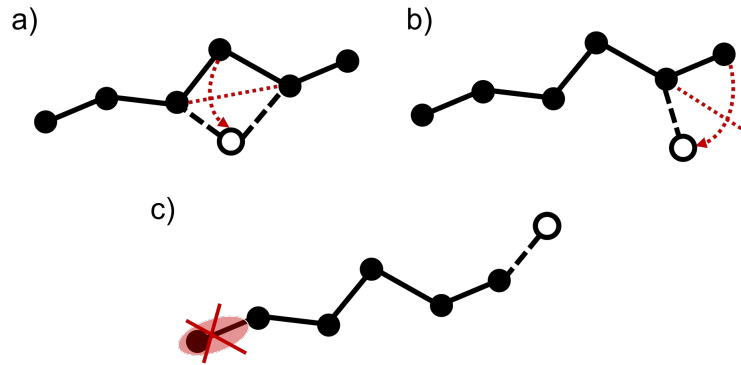


FIGURE 2.3: Illustration of Monte-Carlo moves: a) crankshaft move, b) crankshaft move at the chain end, c) reptation move.

After each move, one accepts or rejects the new microstate according to the acceptance criterion. The acceptance criterion is,

$$P_{\text{acc}} = \min(1, \exp(-\beta\Delta E)) \quad (2.31)$$

where  $\Delta E$  is the energy change caused by the proposed move. This acceptance criterion achieves a Boltzmann distribution of microstates. Then the procedures for implementing MC method based on the chosen moves and acceptance criterion are,

- a) randomly create an initial microstate,
- b) calculate the total energy of the initial microstate,

- c) propose a move based on a random number generator,
- d) calculate the energy change  $\Delta E$ ,
- e) if  $\Delta E < 0$ , then accept the new microstate. Otherwise, compare  $\exp(-\beta\Delta E)$  with a random number  $a \in [0, 1]$ . Accept the new microstate when  $\exp(-\beta\Delta E) > a$ , and retain the previous microstate otherwise.

The procedures from c) to e), so called one "MC step", are repeated to obtain enough number of microstates for the calculation of desired quantities. Because each step only moves one or a few beads, the successive microstates are highly correlated. In practice, it is more common to use "MC cycle" as a measure of the number of steps. Each MC cycle comprises a number of MC steps that equals the number of beads in the system. Namely, in average every bead is given the opportunity to move once within one MC cycle. The number of MC cycles needed for obtaining uncorrelated microstates is the "decorrelation time"  $\tau_{\text{rel}}$ <sup>142</sup>. In this study,  $\tau_{\text{rel}}$  is the number of MC cycles needed for the autocorrelation function of end-to-end vectors of polymer chains to decay to 0.01.  $\tau_{\text{rel}}$  is an important quantity for MC simulations, because the desired quantities should be calculated based on the microstates extending over several decorrelation times. Importantly, the initial microstate is frequently artificial and far from equilibrium. Hence the microstates within the first decorrelation time should not be used for the calculation of desired quantities.

## 2.5 Insights from self-consistent field theory and random phase approximation

The functional-based definition of non-bonded interactions in DFT-based models provides the opportunity to parameterize or improve these models before performing simulations. This can be done by using the mean-field (MF) theory, which is also known as self-consistent field theory<sup>96,143,144</sup>: one extracts thermodynamic properties of DFT-based models within MF theory, and parameterizes or improves CG models by comparing the MF estimates with known thermodynamic properties of target systems. Of course, MF theory fully neglects the effects of fluctuations. To take into account the effect

of small fluctuations, one can use an extension of MF theory, the so called random phase approximation (RPA)<sup>19,145–148</sup>.

In this section, we will first introduce how to derive thermodynamic properties of binary blends and di-BCPs within MF theory. Then we discuss the phase stability of these multi-component systems based on RPA. The main part of this discussion has been published and can be found in the Supplementary Information of ref. [149]. However, the discussion in this section is more detailed and we explain some steps that are omitted in our original publication.

Thermodynamic properties can be determined based on the Helmholtz free energy of systems. In MF theory, one introduces auxiliary fields<sup>145,150–152</sup> to simplify the derivation of Helmholtz free energy and thermodynamic properties. For each particle, its interaction with neighboring particles is replaced by an interaction with average fields, capturing the average behavior of neighboring particles. In this way, all the non-bonded particles are effectively non-interacting, decoupled particles. A system containing many chains is decoupled into single chains in “mean-field”, which to a great extent simplifies the description of polymeric systems.

The formal way of deriving the Helmholtz free energy within MF approximation is to express the partition function of a particle-based CG system in a field-theoretical form by invoking Hubbard-Stratonovich transformation<sup>153–156</sup> or other particle-to-field transformations<sup>7,157,158</sup>. Then the partition function is approximately rewritten using the saddle-point approximation.<sup>19,90,96,150,159</sup> The Helmholtz free energy is expressed in terms of the approximated partition function.

For systems described by DFT-based interactions in eq. 2.21, we derive the field-based Helmholtz free energy in an intuitive way, which clearly shows the underlying assumptions and physical meaning of the theoretical field-based expressions. We first identify the auxiliary fields simply by rewriting



the non-bonded interaction,

$$\begin{aligned}
 \beta H_{\text{nb}} &= \frac{\kappa}{2\rho_0} \int d\mathbf{r} [\hat{\rho}_A(\mathbf{r}) + \hat{\rho}_B(\mathbf{r})]^2 + \frac{\chi}{\rho_0} \int d\mathbf{r} \hat{\rho}_A(\mathbf{r}) \hat{\rho}_B(\mathbf{r}) \\
 &= \frac{1}{2} \left\{ \int \left[ \frac{\kappa}{\rho_0} \hat{\rho}_A(\mathbf{r}) + \frac{\kappa}{\rho_0} \hat{\rho}_B(\mathbf{r}) + \frac{\chi}{\rho_0} \hat{\rho}_B(\mathbf{r}) \right] \hat{\rho}_A(\mathbf{r}) d\mathbf{r} \right. \\
 &\quad \left. + \int \left[ \frac{\kappa}{\rho_0} \hat{\rho}_A(\mathbf{r}) + \frac{\kappa}{\rho_0} \hat{\rho}_B(\mathbf{r}) + \frac{\chi}{\rho_0} \hat{\rho}_A(\mathbf{r}) \right] \hat{\rho}_B(\mathbf{r}) d\mathbf{r} \right\} \\
 &= \frac{1}{2} \left[ \int \hat{W}_A(\mathbf{r}) \hat{\rho}_A(\mathbf{r}) d\mathbf{r} + \int \hat{W}_B(\mathbf{r}) \hat{\rho}_B(\mathbf{r}) d\mathbf{r} \right]
 \end{aligned} \tag{2.32}$$

where  $\hat{W}_A(\mathbf{r})$  and  $\hat{W}_B(\mathbf{r})$  are instantaneous auxiliary fields acting on particles of type A and B, respectively. We can understand the above transformed interaction based on auxiliary fields as follows: the local density field  $\hat{\rho}_\alpha(\mathbf{r})$  interacts with its conjugated auxiliary field  $\hat{W}_\alpha(\mathbf{r})$ . The product of the conjugated pair  $\hat{W}_\alpha(\mathbf{r}) \hat{\rho}_\alpha(\mathbf{r}) d\mathbf{r}$  gives us the local energy at position  $\mathbf{r}$  contributed by particles of type  $\alpha$ . The total energy is obtained from the integration of local energy over the whole space. In MF, one ignores the fluctuations and replaces the instantaneous fields by their average values at a stationary state, or equivalently a saddle point. We denote the average fields with  $\rho_A^*(\mathbf{r})$ ,  $\rho_B^*(\mathbf{r})$ ,  $W_A^*(\mathbf{r})$  and  $W_B^*(\mathbf{r})$ . Hence the average auxiliary fields in MF are defined as,

$$\begin{aligned}
 W_A^*(\mathbf{r}) &= \frac{\kappa}{\rho_0} \rho_A^*(\mathbf{r}) + \frac{\kappa}{\rho_0} \rho_B^*(\mathbf{r}) + \frac{\chi}{\rho_0} \rho_B^*(\mathbf{r}) \\
 W_B^*(\mathbf{r}) &= \frac{\kappa}{\rho_0} \rho_A^*(\mathbf{r}) + \frac{\kappa}{\rho_0} \rho_B^*(\mathbf{r}) + \frac{\chi}{\rho_0} \rho_A^*(\mathbf{r})
 \end{aligned} \tag{2.33}$$

In blends, the average density fields  $\rho_\alpha^*(\mathbf{r})$  are contributed by identical  $n_\alpha$  chains of type  $\alpha$ . In di-BCPs, there are  $n_{AB}$  identical chains comprising an A-block and a B-block which contribute to the average density fields. These identical chains are decoupled with the help of auxiliary fields  $W_\alpha^*(\mathbf{r})$ . Therefore, the average density fields can be expressed for blends as,

$$\rho_\alpha^*(\mathbf{r}) = n_\alpha \left\langle \sum_{s=1}^{N_\alpha} \delta[\mathbf{r} - \mathbf{r}_\alpha(s)] \right\rangle \tag{2.34}$$

For di-BCP, we have,

$$\rho_\alpha^*(\mathbf{r}) = n_{AB} \left\langle \sum_{s=1}^{N_\alpha} \delta[\mathbf{r} - \mathbf{r}_\alpha(s)] \right\rangle \tag{2.35}$$

where  $\delta$  is the Dirac delta function and  $\delta[\mathbf{r} - \mathbf{r}_\alpha(s)]$  represents a point particle at position  $\mathbf{r}_\alpha(s)$ . The angular bracket denotes the average over all the possible single-chain configurations at the saddle point. The average can be obtained by considering single chain partition functions. Hence we can write  $\rho_\alpha^*(\mathbf{r})$  for blends,

$$\rho_\alpha^*(\mathbf{r}) = \frac{n_\alpha}{Q_\alpha} \int \mathcal{D}\mathbf{r}_\alpha(\cdot) \left\{ \exp \left( -\beta H_{b,\alpha}^s[\mathbf{r}_\alpha(\cdot)] \right) \times \exp \left( - \int d\mathbf{r} \sum_{s=1}^{N_\alpha} \delta[\mathbf{r} - \mathbf{r}_\alpha(s)] W_\alpha^*(\mathbf{r}) \right) \sum_{t=1}^{N_\alpha} \delta[\mathbf{r} - \mathbf{r}_\alpha(t)] \right\} \quad (2.36)$$

and for di-BCPs,

$$\rho_\alpha^*(\mathbf{r}) = \frac{n_{AB}}{Q_{AB}} \times \int \mathcal{D}\mathbf{r}_{AB}(\cdot) \left\{ \exp \left( -\beta H_{b,A}^s[\mathbf{r}_A(\cdot)] - \beta H_{b,B}^s[\mathbf{r}_B(\cdot)] \right) \times \exp \left( - \int d\mathbf{r} \sum_{s=1}^{N_A} \delta[\mathbf{r} - \mathbf{r}_A(s)] W_A^*(\mathbf{r}) \right) \times \exp \left( - \int d\mathbf{r} \sum_{s=1}^{N_B} \delta[\mathbf{r} - \mathbf{r}_B(s)] W_B^*(\mathbf{r}) \right) \sum_{t=1}^{N_\alpha} \delta[\mathbf{r} - \mathbf{r}_\alpha(t)] \right\} \quad (2.37)$$

where  $\mathcal{D}\mathbf{r}_\alpha(\cdot)$  denotes functional integration over all possible conformations of a single homopolymer chain or a di-BCP chain.  $\beta H_{b,\alpha}^s[\mathbf{r}(\cdot)]$  stands for the bonded potential for the single chain or block comprising beads of type  $\alpha$ .  $Q_\alpha$  and  $Q_{AB}$  is single-chain partition functions for homopolymer chains in blends and chains in di-BCPs, respectively. They are defined as,

$$Q_\alpha = \int \mathcal{D}\mathbf{r}_\alpha(\cdot) \exp \left( -\beta H_{b,\alpha}^s[\mathbf{r}_\alpha(\cdot)] \right) \exp \left( - \int d\mathbf{r} \sum_{s=1}^{N_\alpha} \delta[\mathbf{r} - \mathbf{r}_\alpha(s)] W_\alpha^*(\mathbf{r}) \right) \quad (2.38)$$

$$Q_{AB} = \int \mathcal{D}\mathbf{r}_{AB}(\cdot) \exp \left( -\beta H_{b,A}^s[\mathbf{r}_A(\cdot)] - \beta H_{b,B}^s[\mathbf{r}_B(\cdot)] \right) \times \exp \left( - \int d\mathbf{r} \sum_{s=1}^{N_A} \delta[\mathbf{r} - \mathbf{r}_A(s)] W_A^*(\mathbf{r}) \right) \times \exp \left( - \int d\mathbf{r} \sum_{s=1}^{N_B} \delta[\mathbf{r} - \mathbf{r}_B(s)] W_B^*(\mathbf{r}) \right) \quad (2.39)$$

The system of equations defined in eqs. 2.33, 2.36 and 2.37 clearly shows the self-consistency between local density fields  $\rho_\alpha^*(\mathbf{r})$  and conjugated fields  $W_\alpha^*(\mathbf{r})$ . Namely, eq. 2.33 defines fields  $W_\alpha^*(\mathbf{r})$  in terms of  $\rho_\alpha^*(\mathbf{r})$ . Eqs. 2.36 and 2.37 demonstrate the resulting density fields based on given fields  $W_\alpha^*(\mathbf{r})$ .

The equation set derived through the simple, intuitive way is same as the equation set of saddle-point conditions one would obtain following formal frameworks, e.g., Hubbard-Stratonovich transformation.

Once we know the form of the Helmholtz free energy within MF approximation, we can further derive any desired thermodynamic properties. To determine the Helmholtz free energy, we use the standard definition,

$$F = U - TS \quad (2.40)$$

where  $F$  is Helmholtz free energy,  $U$  is average internal energy,  $T$  is absolute temperature and  $S$  is entropy. The average internal energy  $U$  of DFT-based models is determined by the predefined potentials. For blends,

$$\begin{aligned} \beta U = \beta H_b + \beta H_{nb} = \sum_{\alpha} n_{\alpha} \beta H_{b,\alpha}^s \\ + \frac{\kappa}{2\rho_0} \int d\mathbf{r} (\rho_A^*(\mathbf{r}) + \rho_B^*(\mathbf{r}))^2 + \frac{\chi}{\rho_0} \int d\mathbf{r} \rho_A^*(\mathbf{r}) \rho_B^*(\mathbf{r}) \end{aligned} \quad (2.41)$$

Similar expression holds for di-BCPs:

$$\begin{aligned} \beta U = \beta H_b + \beta H_{nb} = n_{AB} \left( \beta H_{b,A}^s + \beta H_{b,B}^s \right) \\ + \frac{\kappa}{2\rho_0} \int d\mathbf{r} (\rho_A^*(\mathbf{r}) + \rho_B^*(\mathbf{r}))^2 + \frac{\chi}{\rho_0} \int d\mathbf{r} \rho_A^*(\mathbf{r}) \rho_B^*(\mathbf{r}) \end{aligned} \quad (2.42)$$

where  $\beta H_{b,\alpha}^s = \langle H_{b,\alpha}^s[\mathbf{r}(\cdot)] \rangle$  denotes average bonded energy of a single chain (block) of type  $\alpha$  in the fields  $W_A^*(\mathbf{r})$  and  $W_B^*(\mathbf{r})$ .

For systems containing decoupled chains, the entropy  $S$  can be calculated based on statistical mechanics of non-interacting ideal chains. For blends,

$$\begin{aligned} \beta TS = \beta U_{id} - \beta F_{id} = \beta U_{id} + \ln Z_{id} \\ = \beta \sum_{\alpha=A,B} n_{\alpha} U_{0,\alpha} + \ln \frac{V^{n_A}}{n_A!} \left( \frac{Q_A[W_A^*(\mathbf{r})]}{V} \right)^{n_A} + \ln \frac{V^{n_B}}{n_B!} \left( \frac{Q_B[W_B^*(\mathbf{r})]}{V} \right)^{n_B} \\ = \sum_{\alpha=A,B} n_{\alpha} \beta H_{b,\alpha}^s + \sum_{\alpha=A,B} \int W_{\alpha}^*(\mathbf{r}) \rho_{\alpha}^*(\mathbf{r}) d\mathbf{r} \\ + \sum_{\alpha=A,B} n_{\alpha} \left[ 1 - \ln \left( \frac{n_{\alpha}}{V} \right) \right] + \sum_{\alpha=A,B} n_{\alpha} \ln \left( \frac{Q_{\alpha}[W_{\alpha}^*(\mathbf{r})]}{V} \right) \end{aligned} \quad (2.43)$$

For di-BCPs,

$$\begin{aligned}
\beta TS &= \beta U_{\text{id}} - \beta F_{\text{id}} = \beta U_{\text{id}} + \ln Z_{\text{id}} \\
&= \beta n_{\text{AB}} U_{0,\text{AB}} + \ln \frac{V^{n_{\text{AB}}}}{n_{\text{AB}}!} \left( \frac{Q_{\text{AB}}[W_{\text{A}}^*(\mathbf{r}), W_{\text{B}}^*(\mathbf{r})]}{V} \right)^{n_{\text{AB}}} \\
&= n_{\text{AB}} \left( \beta H_{\text{b,A}}^s + \beta H_{\text{b,B}}^s \right) + \sum_{\alpha=\text{A,B}} \int W_{\alpha}^*(\mathbf{r}) \rho_{\alpha}^*(\mathbf{r}) d\mathbf{r} \\
&\quad + n_{\text{AB}} \left[ 1 - \ln \left( \frac{n_{\text{AB}}}{V} \right) \right] + n_{\text{AB}} \ln \left( \frac{Q_{\text{AB}}[W_{\text{A}}^*(\mathbf{r}), W_{\text{B}}^*(\mathbf{r})]}{V} \right)
\end{aligned} \tag{2.44}$$

where  $U_{\text{id}}$ ,  $F_{\text{id}}$  and  $Z_{\text{id}}$  is average internal energy, free energy, and partition function, respectively, of the system containing non-interacting ideal chains. We insert volume  $V$  into the free energy term, i.e.,  $-\ln Z_{\text{id}}$ , to signify the extensive nature of free energy.  $U_{0,\alpha}$  and  $U_{0,\text{AB}}$  is average internal energy of a single homopolymer chain of type  $\alpha$  and a di-BCP chain, respectively. The Helmholtz free energy is obtained by substituting the entropy  $S$  defined in eq. 2.43 or 2.44 and the internal energy defined in eq. 2.41 or 2.42 into the standard definition of Helmholtz free energy in eq. 2.40. We separately write the expressions for blends and di-BCPs,

$$\begin{aligned}
\beta F_{\text{blend}} &= \sum_{\alpha=\text{A,B}} n_{\alpha} \left[ \ln \left( \frac{n_{\alpha}}{V} \right) - 1 \right] - \sum_{\alpha=\text{A,B}} n_{\alpha} \ln \left( \frac{Q_{\alpha}[W_{\alpha}^*(\mathbf{r})]}{V} \right) \\
&\quad - \sum_{\alpha=\text{A,B}} \int W_{\alpha}^*(\mathbf{r}) \rho_{\alpha}^*(\mathbf{r}) d\mathbf{r} + \frac{\kappa}{2\rho_0} \int (\rho_{\text{A}}^*(\mathbf{r}) + \rho_{\text{B}}^*(\mathbf{r}))^2 d\mathbf{r} + \frac{\chi}{\rho_0} \int \rho_{\text{A}}^*(\mathbf{r}) \rho_{\text{B}}^*(\mathbf{r}) d\mathbf{r}
\end{aligned} \tag{2.45}$$

and

$$\begin{aligned}
\beta F_{\text{BCP}} &= n_{\text{AB}} \left[ \ln \left( \frac{n_{\text{AB}}}{V} \right) - 1 \right] - n_{\text{AB}} \ln \left( \frac{Q_{\text{AB}}[W_{\text{A}}^*(\mathbf{r}), W_{\text{B}}^*(\mathbf{r})]}{V} \right) \\
&\quad - \sum_{\alpha=\text{A,B}} \int W_{\alpha}^*(\mathbf{r}) \rho_{\alpha}^*(\mathbf{r}) d\mathbf{r} + \frac{\kappa}{2\rho_0} \int (\rho_{\text{A}}^*(\mathbf{r}) + \rho_{\text{B}}^*(\mathbf{r}))^2 d\mathbf{r} + \frac{\chi}{\rho_0} \int \rho_{\text{A}}^*(\mathbf{r}) \rho_{\text{B}}^*(\mathbf{r}) d\mathbf{r}
\end{aligned} \tag{2.46}$$

In both formulas, the first term comes from the factorial in eqs. 2.43 and 2.44. The following two terms correspond to conformational entropy of chains, and the last two terms are the contributions from non-bonded interactions.

Having found the form of Helmholtz free energy, we need to insert solutions of density fields and conjugated fields at the saddle point to further derive thermodynamic properties. However, there are generally multiple saddle

points for one system. Each solution can be associated with a local minimum of free energy<sup>146</sup>, at which point the state can be stable or meta-stable.

In our work, the solutions which allow us analytically derive thermodynamic properties are preferred. One of such solutions corresponds to a fully homogeneous system<sup>146</sup>. Specifically, the system has homogeneous particle densities and homogeneous fields, which are defined as,

$$\bar{\rho}_0 = \bar{\rho}_A + \bar{\rho}_B = (n_A N_A + n_B N_B) / V \quad (2.47)$$

and

$$\bar{W}_A = \frac{\kappa}{\rho_0}(\bar{\rho}_A + \bar{\rho}_B), \quad \bar{W}_B = \frac{\kappa}{\rho_0}(\bar{\rho}_A + \bar{\rho}_B) \quad (2.48)$$

Here we consider the blends or di-BCPs with  $\chi = 0$  and the third term in eq. 2.33 is ignored. The corresponding Helmholtz free energy  $F$  is,

$$\beta F = \sum_{\alpha} n_{\alpha} \ln \left( \frac{n_{\alpha}}{V} \right) + \frac{\kappa V}{2\rho_0} (\bar{\rho}_A + \bar{\rho}_B)^2 \quad (2.49)$$

in which the contribution of conformational entropy of chains is neglected. Based on eq. 2.49, we can calculate the desired thermodynamic properties. For example, the isothermal compressibility  $\kappa_T$ <sup>160</sup> can be derived with the help of the equation of state  $P = -\partial F / \partial V$ ,

$$\frac{1}{k_B T \kappa_T} = -V \frac{\partial P}{\partial V} = V \frac{\partial^2 F}{\partial^2 V} \quad (2.50)$$

Then we can write:

$$\begin{aligned} \frac{1}{k_B T \kappa_T} &= V \frac{\partial^2 \left[ n_A \ln \frac{n_A}{V} + n_B \ln \frac{n_B}{V} + \frac{\kappa(n_A N_A + n_B N_B)}{2\rho_0 V} \right]}{\partial^2 V} \\ &= \frac{n_A + n_B}{V} + \frac{\kappa}{\rho_0} \bar{\rho}_0^2 \end{aligned} \quad (2.51)$$

which is the eq. 2.17 having discussed in section 2.2.

The assumption of MF theory on ignoring all fluctuations is usually poor for systems at atomistic scale. This is because the coordination number of atoms is small<sup>146</sup>,  $\sim 10$ . Hence the fluctuations of environment (fields) around atoms are non-neglectable. While from a mesoscopic perspective, one considers an effective coordination number of polymer chains, which is on the order of  $\sim \bar{\rho}_0 R_e^3$ . The effective coordination number can be very large in

dense melts of large molecules. Since the fluctuations diminish with the increasing of coordination numbers, the estimates of MF theory for dense melts of large molecules are accurate<sup>19</sup>.

Notwithstanding, it is possible to take into account small fluctuations by using RPA, so that we can study phase stability in multi-component systems. RPA assumes that fields can locally deviate from their average values in MF theory by a small amplitude  $\delta W_\alpha(\mathbf{r})$ , such that  $\int \delta W_\alpha(\mathbf{r}) d\mathbf{r} = 0$ . Notice that the accuracy of RPA predictions decreases rapidly when one approaches the phase transition point. This is because the magnitude of fluctuations at states closing to phase transition is comparable with the average values and one cannot assume the fluctuations are small.

When one considers a small perturbation of fields, the single-chain partition functions are defined as follow. For blends we have,

$$Q_\alpha = \int \mathcal{D}\mathbf{r}_\alpha(\cdot) \exp\left(-\beta H_{b,\alpha}^s[\mathbf{r}_\alpha(\cdot)]\right) \times \exp\left(-\int d\mathbf{r} \sum_{s=1}^{N_\alpha} \delta(\mathbf{r} - \mathbf{r}_\alpha(s))(\bar{W}_\alpha + \delta W_\alpha(\mathbf{r}))\right) \quad (2.52)$$

For di-BCPs we have:

$$Q_{AB} = \int \mathcal{D}_{AB}\mathbf{r}_\alpha(\cdot) \exp\left(-\beta H_{b,A}^s[\mathbf{r}_A(\cdot)] - \beta H_{b,B}^s[\mathbf{r}_B(\cdot)]\right) \times \exp\left(-\int d\mathbf{r} \sum_{s=1}^{N_A} \delta(\mathbf{r} - \mathbf{r}_A(s))(\bar{W}_A + \delta W_A(\mathbf{r}))\right) \times \exp\left(-\int d\mathbf{r} \sum_{s=1}^{N_B} \delta(\mathbf{r} - \mathbf{r}_B(s))(\bar{W}_B + \delta W_B(\mathbf{r}))\right) \quad (2.53)$$

We expand above single-chain partition functions to the second order in  $\delta W_\alpha(\mathbf{r})$  and conveniently express them in Fourier space,

$$Q_\alpha \simeq Q_{0,\alpha} \exp\left[\frac{N_\alpha}{2V^2} \sum_{\mathbf{q}} g_\alpha(\mathbf{q}) \delta W_\alpha(\mathbf{q}) \delta W_\alpha(-\mathbf{q})\right] \quad (2.54)$$

$$Q_{AB} \simeq Q_{0,AB} \times \exp \left[ \frac{N_{AB}}{2V^2} \sum_{\mathbf{q}} g_A(\mathbf{q}) \delta W_A(\mathbf{q}) \delta W_A(-\mathbf{q}) + g_B(\mathbf{q}) \delta W_B(\mathbf{q}) \delta W_B(-\mathbf{q}) + 2g_{AB}(\mathbf{q}) \delta W_A(\mathbf{q}) \delta W_B(-\mathbf{q}) \right] \quad (2.55)$$

where  $Q_{0,\alpha}$  are single chain partition functions in spatially homogeneous fields. The direct and inverse Fourier transforms are defined as,

$$f(\mathbf{q}) = \int d\mathbf{r} \exp[i \mathbf{q} \cdot \mathbf{r}] f(\mathbf{r}) \quad f(\mathbf{r}) = \frac{1}{V} \sum_{\mathbf{q}} \exp[-i \mathbf{q} \cdot \mathbf{r}] f(\mathbf{q}) \quad (2.56)$$

$g_\alpha(q)$  is single-chain structure factor of homopolymer chains of specie  $\alpha$ . The definition of  $g_\alpha(q)$  in blends is,

$$g_\alpha(\mathbf{q}) = \frac{\left\langle \sum_{\mathbf{i}}^{N_\alpha} \sum_{\mathbf{j}}^{N_\alpha} \exp [i \mathbf{q} \cdot (\mathbf{r}_i - \mathbf{r}_j)] \right\rangle}{N_\alpha} \quad (2.57)$$

For di-BCPs the corresponding (partial) single-chain structure factors in eq. 2.55 are defined as:

$$g_\alpha(\mathbf{q}) = \frac{\left\langle \sum_{\mathbf{i}}^{N_\alpha} \sum_{\mathbf{j}}^{N_\alpha} \exp [i \mathbf{q} \cdot (\mathbf{r}_i - \mathbf{r}_j)] \right\rangle}{N_{AB}} \quad (2.58)$$

$$g_{AB}(\mathbf{q}) = \frac{\left\langle \sum_{\mathbf{i}}^{N_A} \exp (i \mathbf{q} \cdot \mathbf{r}_i) \sum_{\mathbf{j}}^{N_B} \exp (-i \mathbf{q} \cdot \mathbf{r}_j) \right\rangle}{N_{AB}}$$

The angular brackets denote an average over all possible single-chain conformations and orientations of wavevectors, with given modulus  $q$ . It can be numerically calculated by sampling configurations obtained from simulations of ideal chains. For continuum Gaussian chains, one can directly adopt an analytical formula of single-chain structure factor, which is known as the Debye function<sup>113</sup>.

The approximated single-chain partition functions in eqs. 2.54 and 2.55 are substituted into  $\beta F_{\text{blend}}$  and  $\beta F_{\text{BCP}}$ . The saddle-point condition given by eq. 2.36 for blends and eq. 2.37 for di-BCP, is evaluated within the linear-response approximation. The linearized saddle-point equations are used to express the fields  $\delta W_\alpha(\mathbf{q})$  through linear functions of densities  $\rho_\alpha(\mathbf{q})$ . These linear expressions of  $\delta W_\alpha(\mathbf{q})$  through  $\rho_\alpha(\mathbf{q})$  are also substituted into  $\beta F_m$ .

Following a convenient matrix notation, the final result reads:

$$\beta F_m = \frac{1}{2\rho_0 V} \sum_{\mathbf{q}} \begin{bmatrix} \rho(\mathbf{q}) & \phi(\mathbf{q}) \end{bmatrix} \mathbf{D}_m \begin{bmatrix} \rho(-\mathbf{q}) \\ \phi(-\mathbf{q}) \end{bmatrix} \quad (2.59)$$

where  $\rho(\mathbf{q}) \equiv \rho_A(\mathbf{q}) + \rho_B(\mathbf{q})$  (Fourier transform of total local density) and  $\phi(\mathbf{q}) \equiv \rho_A(\mathbf{q}) - \rho_B(\mathbf{q})$  (Fourier transform of local composition). The matrices  $\mathbf{D}_m$  for blends and di-BCPs are:

$$\mathbf{D}_{\text{Blend}} = \begin{bmatrix} \kappa + \frac{\chi}{2} + \frac{1}{4\bar{\phi}_A g_A(\mathbf{q})} + \frac{1}{4\bar{\phi}_B g_B(\mathbf{q})} & \frac{1}{4\bar{\phi}_A g_A(\mathbf{q})} - \frac{1}{4\bar{\phi}_B g_B(\mathbf{q})} \\ \frac{1}{4\bar{\phi}_A g_A(\mathbf{q})} - \frac{1}{4\bar{\phi}_B g_B(\mathbf{q})} & -\frac{\chi}{2} + \frac{1}{4\bar{\phi}_A g_A(\mathbf{q})} + \frac{1}{4\bar{\phi}_B g_B(\mathbf{q})} \end{bmatrix} \quad (2.60)$$

$$\mathbf{D}_{\text{BCP}} = \begin{bmatrix} \kappa + \frac{\chi}{2} - \frac{g_A(\mathbf{q}) + g_B(\mathbf{q}) - 2g_{AB}(\mathbf{q})}{4(g_{AB}^2(\mathbf{q}) - g_A(\mathbf{q})g_B(\mathbf{q}))} & -\frac{g_B(\mathbf{q}) - g_A(\mathbf{q})}{4(g_{AB}^2(\mathbf{q}) - g_A(\mathbf{q})g_B(\mathbf{q}))} \\ -\frac{g_B(\mathbf{q}) - g_A(\mathbf{q})}{4(g_{AB}^2(\mathbf{q}) - g_A(\mathbf{q})g_B(\mathbf{q}))} & -\frac{\chi}{2} - \frac{g_A(\mathbf{q}) + g_B(\mathbf{q}) + 2g_{AB}(\mathbf{q})}{4(g_{AB}^2(\mathbf{q}) - g_A(\mathbf{q})g_B(\mathbf{q}))} \end{bmatrix} \quad (2.61)$$

$\bar{\phi}_\alpha$  denotes average volume fractions and are defined as  $\bar{\phi}_A = N_A n_A / \rho_0 V$  and  $\bar{\phi}_B = N_B n_B / \rho_0 V$ .

Inspecting the structure of  $\mathbf{D}_{\text{blend}}$  and  $\mathbf{D}_{\text{BCP}}$  we observe that for the special case of compositionally and conformationally symmetric blends and di-BCPs these matrices are diagonal. Therefore the fluctuations of  $\rho(\mathbf{q})$  and  $\phi(\mathbf{q})$  are decoupled. In this case, the structure factors of fluctuations of density,  $\langle \rho(\mathbf{q}) \rho(-\mathbf{q}) \rangle$ , and composition,  $\langle \phi(\mathbf{q}) \phi(-\mathbf{q}) \rangle$ , can be extracted from the diagonal elements of  $\mathbf{D}_{\text{blend}}$  and  $\mathbf{D}_{\text{BCP}}$ , directly invoking equipartition theorem.

However, in this thesis the asymmetric systems are considered. Then  $\mathbf{D}_m$  is non-diagonal, meaning the variables  $\rho(\mathbf{q})$  and  $\phi(\mathbf{q})$  are coupled. To calculate structure factors, the quadratic form of  $F$  must be first diagonalized to the



following form<sup>161</sup>:

$$\beta F_m = \frac{1}{2\rho_0 V} \sum_{\mathbf{q}} \begin{bmatrix} X(\mathbf{q}) & Y(\mathbf{q}) \end{bmatrix} \mathbf{A}_m \begin{bmatrix} X(-\mathbf{q}) \\ Y(-\mathbf{q}) \end{bmatrix} \quad (2.62)$$

with

$$\mathbf{A}_m = \mathbf{P}_m^T \mathbf{D}_m \mathbf{P}_m = \begin{bmatrix} \lambda_1 & 0 \\ 0 & \lambda_2 \end{bmatrix} \quad \text{and} \quad \begin{bmatrix} X(\mathbf{q}) \\ Y(\mathbf{q}) \end{bmatrix} = \mathbf{P}_m^T \begin{bmatrix} \rho(\mathbf{q}) \\ \phi(\mathbf{q}) \end{bmatrix} \quad (2.63)$$

Here  $\lambda_1$  and  $\lambda_2$  are eigenvalues of the symmetric matrix  $\mathbf{D}_m$ . The orthogonal matrix  $\mathbf{P}_m$  is defined through the components of two orthonormal eigenvectors  $\tilde{v}$  and  $\tilde{v}$  of the matrix  $\mathbf{D}_m$  as:

$$\mathbf{P}_m = \begin{bmatrix} \tilde{v}_1 & \tilde{v}_1 \\ \tilde{v}_2 & \tilde{v}_2 \end{bmatrix}_m \quad (2.64)$$

Accordingly, the local density and composition can be expressed through  $X(\mathbf{q})$  and  $Y(\mathbf{q})$ ,

$$\begin{bmatrix} \rho(\mathbf{q}) \\ \phi(\mathbf{q}) \end{bmatrix} = \mathbf{P}_m \begin{bmatrix} X(\mathbf{q}) \\ Y(\mathbf{q}) \end{bmatrix} \Rightarrow \begin{aligned} \rho(\mathbf{q}) &= \tilde{v}_1 X(\mathbf{q}) + \tilde{v}_1 Y(\mathbf{q}) \\ \phi(\mathbf{q}) &= \tilde{v}_2 X(\mathbf{q}) + \tilde{v}_2 Y(\mathbf{q}) \end{aligned} \quad (2.65)$$

Because the matrix  $\mathbf{A}_m$  is diagonal,  $X(\mathbf{q})$  and  $Y(\mathbf{q})$  are decoupled variables. Therefore  $\langle X(\mathbf{q})X(-\mathbf{q}) \rangle$  and  $\langle Y(\mathbf{q})Y(-\mathbf{q}) \rangle$  can be obtained from the diagonal elements of  $\mathbf{A}_m$ ,

$$\frac{\langle X(\mathbf{q})X(-\mathbf{q}) \rangle}{\rho_0 V} = \lambda_1^{-1}, \quad \frac{\langle Y(\mathbf{q})Y(-\mathbf{q}) \rangle}{\rho_0 V} = \lambda_2^{-1} \quad (2.66)$$

The structure factors of density and composition fluctuations are,

$$\boxed{\begin{aligned} \frac{\langle \rho(\mathbf{q})\rho(-\mathbf{q}) \rangle}{\rho_0 V} &= \tilde{v}_1^2 \lambda_1^{-1} + \tilde{v}_2^2 \lambda_2^{-1} \\ \frac{\langle \phi(\mathbf{q})\phi(-\mathbf{q}) \rangle}{\rho_0 V} &= \tilde{v}_2^2 \lambda_1^{-1} + \tilde{v}_1^2 \lambda_2^{-1} \end{aligned}} \quad (2.67)$$

Hence, the RPA structure factors of density and composition fluctuations in the most general case of asymmetric systems can be calculated via eq. 2.67 once we know the eigenvalues and the corresponding orthonormal eigenvectors of matrix  $\mathbf{D}_m$ . For the matrix  $\mathbf{D}_{\text{blend}}$  in eq. 2.60, the eigenvalues  $\lambda_1$ ,  $\lambda_2$ , and eigenvectors  $\boldsymbol{\nu}$ ,  $\boldsymbol{v}$  are listed below.

$$\lambda_1 = \frac{G_{\text{Blend},A}(\mathbf{q}) + G_{\text{Blend},B}(\mathbf{q}) + 2\kappa - \sqrt{(G_{\text{Blend},A}(\mathbf{q}) - G_{\text{Blend},B}(\mathbf{q}))^2 + 4(\chi + \kappa)^2}}{4} \quad (2.68)$$

$$\lambda_2 = \frac{G_{\text{Blend},A}(\mathbf{q}) + G_{\text{Blend},B}(\mathbf{q}) + 2\kappa + \sqrt{(G_{\text{Blend},A}(\mathbf{q}) - G_{\text{Blend},B}(\mathbf{q}))^2 + 4(\chi + \kappa)^2}}{4} \quad (2.69)$$

$$\boldsymbol{\nu} = \begin{bmatrix} \frac{2(\kappa + \chi) - \sqrt{4(\kappa + \chi)^2 + (G_{\text{Blend},A}(\mathbf{q}) - G_{\text{Blend},B}(\mathbf{q}))^2}}{G_{\text{Blend},A}(\mathbf{q}) - G_{\text{Blend},B}(\mathbf{q})} \\ 1 \end{bmatrix} = \begin{bmatrix} \nu_1 \\ \nu_2 \end{bmatrix} \quad (2.70)$$

$$\boldsymbol{v} = \begin{bmatrix} \frac{2(\kappa + \chi) + \sqrt{4(\kappa + \chi)^2 + (G_{\text{Blend},A}(\mathbf{q}) - G_{\text{Blend},B}(\mathbf{q}))^2}}{G_{\text{Blend},A}(\mathbf{q}) - G_{\text{Blend},B}(\mathbf{q})} \\ 1 \end{bmatrix} = \begin{bmatrix} v_1 \\ v_2 \end{bmatrix} \quad (2.71)$$

with

$$G_{\text{Blend},A}(\mathbf{q}) = \frac{1}{\bar{\phi}_A g_A(\mathbf{q})}, \quad G_{\text{Blend},B}(\mathbf{q}) = \frac{1}{\bar{\phi}_B g_B(\mathbf{q})} \quad (2.72)$$

For di-BCPs, the eigenvalues and eigenvectors are,

$$\lambda_1 = \frac{-G_{\text{BCP},A}(\mathbf{q}) - G_{\text{BCP},B}(\mathbf{q}) + 2\kappa}{4} - \frac{\sqrt{(G_{\text{BCP},A}(\mathbf{q}) - G_{\text{BCP},B}(\mathbf{q}))^2 + 4(G_{\text{BCP},AB}(\mathbf{q}) + \kappa + \chi)^2}}{4} \quad (2.73)$$

$$\lambda_2 = \frac{-G_{\text{BCP},A}(\mathbf{q}) - G_{\text{BCP},B}(\mathbf{q}) + 2\kappa}{4} + \frac{\sqrt{(G_{\text{BCP},A}(\mathbf{q}) - G_{\text{BCP},B}(\mathbf{q}))^2 + 4(G_{\text{BCP},AB}(\mathbf{q}) + \kappa + \chi)^2}}{4} \quad (2.74)$$

$$\boldsymbol{\nu} = \begin{bmatrix} \frac{2(\kappa+\chi)+2G_{\text{BCP},AB}(\mathbf{q})-\sqrt{4(G_{\text{BCP},AB}(\mathbf{q})+\kappa+\chi)^2+(G_{\text{BCP},A}(\mathbf{q})-G_{\text{BCP},B}(\mathbf{q}))^2}}{G_{\text{BCP},A}(\mathbf{q})-G_{\text{BCP},B}(\mathbf{q})} \\ 1 \end{bmatrix} = \begin{bmatrix} \nu_1 \\ \nu_2 \end{bmatrix} \quad (2.75)$$

$$\boldsymbol{\nu} = \begin{bmatrix} \frac{2(\kappa+\chi)+2G_{\text{BCP},AB}(\mathbf{q})+\sqrt{4(G_{\text{BCP},AB}(\mathbf{q})+\kappa+\chi)^2+(G_{\text{BCP},A}(\mathbf{q})-G_{\text{BCP},B}(\mathbf{q}))^2}}{G_{\text{BCP},A}(\mathbf{q})-G_{\text{BCP},B}(\mathbf{q})} \\ 1 \end{bmatrix} = \begin{bmatrix} \nu_1 \\ \nu_2 \end{bmatrix} \quad (2.76)$$

with

$$G_{\text{BCP},A}(\mathbf{q}) = \frac{g_A(\mathbf{q})}{g_{\text{AB}}^2(\mathbf{q}) - g_A(\mathbf{q})g_B(\mathbf{q})}, \quad G_{\text{BCP},B}(\mathbf{q}) = \frac{g_B(\mathbf{q})}{g_{\text{AB}}^2(\mathbf{q}) - g_A(\mathbf{q})g_B(\mathbf{q})}$$

$$G_{\text{BCP},AB}(\mathbf{q}) = \frac{g_{\text{AB}}(\mathbf{q})}{g_{\text{AB}}^2(\mathbf{q}) - g_A(\mathbf{q})g_B(\mathbf{q})} \quad (2.77)$$

The normalized eigenvectors are trivially obtained as  $\tilde{\boldsymbol{\nu}} = \boldsymbol{\nu} / \sqrt{\nu_1^2 + \nu_2^2}$  and  $\tilde{\boldsymbol{v}} = \boldsymbol{v} / \sqrt{v_1^2 + v_2^2}$ .



## Chapter 3

# Disorder morphology in blend-/BCP-based PLED

The study presented in this chapter has been published in the ref. [149]. In order to integrate the published contents into this thesis, we include only the sections of the paper which are compatible with the scope of this chapter, and modify small parts of the original text at various places. Specifically, Sections 3.1 and 3.2 are written based on sections 1 and 2 of ref. [149] and its Supplementary Information. For these sections, parts of the contents in the published paper are omitted for a better integration with the thesis, and a few discussions are rewritten. Sections 3.3, 3.5, 3.6 and 3.7 are almost identical to the corresponding parts of the published paper. The section 3.4 is taken from the Supplementary Information of the published paper.

### 3.1 Introduction

In this chapter, we use the mesoscopic model to simulate the morphologies within active layers of polymeric light-emitting diodes (PLED)<sup>162</sup>. As shown in Fig. 3.1, PLED consists of a thin active layer with typical thickness on the order of 100 nm. The active layer contains luminescent semiconducting polymers<sup>163</sup>, within which the electrons and holes injected from cathode and anode can form excitons. Then the light is generated through radiative decay of excitons. One needs at least one transparent electrode, so that light can pass through. Fig. 3.1 shows one of the possible structures, i.e., top-emitting PLED.

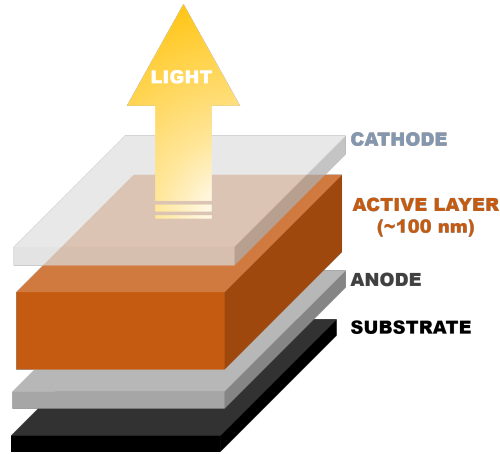


FIGURE 3.1: The basic structure of a top-emitting PLED.

Having high luminous efficiency within PLED relies on the balanced transport of holes and electrons. Though in commonly used polymeric semiconductors, electron transport – unlike hole transport – is limited by trap states, likely caused by chemical impurities<sup>164</sup>. The disbalance in transport of electrons and holes<sup>163</sup> caused by the trap sites reduces luminous efficiency. Recent studies have shown that the negative impact of trap sites on luminous efficiency can be alleviated by using blend-based active layers, which are formed by blends of semiconducting and insulating polymers<sup>165</sup>. This approach is motivated by the theoretical prediction of Mark and Helfrich (MH)<sup>166</sup> that the trap-limited current density  $J$  scales as  $J \sim N/N_t^r$ , where  $N$  and  $N_t$  are the densities of transport and trapping sites. The exponent  $r$  is a measure of the width of the energetic distribution of the trap states. For disordered visible light-emitting semiconductors<sup>165,167</sup>,  $r \geq 4$  typically. To first approximation, blending with an insulator reduces both  $N$  and  $N_t$  by the average volume fraction of the semiconducting polymer  $\bar{\phi}_A$  ( $0 < \bar{\phi}_A < 1$ ). Hence, the electron current density increases to  $J_{\text{blend}} \approx \bar{\phi}_A^{(1-r)} J$ . It has been shown that diluting the semiconductor with 90% of an insulator doubles the luminous efficiency of the PLED<sup>165,167</sup>.

The concept of alleviating negative impact of trap sites by blending requires intimate mixing between the semiconducting and insulating polymers<sup>167</sup>, i.e., disordered phase is preferred. However, polymer blends are prone to macroscopic phase separation: the strength of immiscibility is proportional to chain length, so that even weak incompatibilities between monomers are amplified in the blends containing large molecules. According to an earlier study of active layers containing blends formed by poly[2-methoxy-5-(2-ethylhexyloxy)-1,4-phenylenevinylene] (MEH-PPV) and

polystyrene<sup>167</sup>, one encounters phase segregation when working with molecular weights commonly used in experiments, e.g., MEH-PPV with  $\sim 300$  kg/mol and polystyrene with  $\sim 10$  kg/mol.

One possibility to increase stability of disordered phases is to link semiconducting and insulating polymers into an “equivalent” diblock-copolymer (di-BCP), i.e., using BCP-based active layers. The rationale is simple: covalently linked blocks of dissimilar polymers cannot segregate into macroscopic phases (as homopolymers do) though microphase separate into regular domain patterns<sup>147,168,169</sup>. Because of entropy losses caused<sup>169,170</sup> by stretching of blocks inside domains and localization of block junctions at domain interfaces, microphase separation in BCPs requires stronger immiscibility (which for mixtures with UCST behavior is equivalent to lower temperatures) than phase separation in the equivalent blend. For example, consider compositionally and conformationally symmetric blends of homopolymers comprised of  $N$  monomers each. Monomer/monomer incompatibility is quantified by the Flory-Huggins (FH) parameter, which in the simplest case has only an enthalpic contribution:  $\chi = B/T$  ( $B$  is a constant and  $T$  is the temperature). For a symmetric blend, the phase transition from disordered to the macroscopically separated phase occurs<sup>113</sup> within MF at  $\chi N = 2$ . In contrast, for an equivalent BCP comprising  $2N$  monomers, the phase transition from disordered state to an ordered microdomain structure, i.e. order-disorder transition (ODT), happens<sup>147</sup> within MF at  $2\chi N \simeq 10.49$ . Hence, in this example, substituting a blend by a BCP reduces the threshold temperature, below which the disordered phase is unfavorable thermodynamically, by 2.5 times.

Though the ideal of using BCP-based active layers is attractive, it requires detailed investigation because disordered blends and BCPs are structurally not equivalent. The phase transitions in blends and BCPs belong to different universality classes: 3D Ising<sup>171–175</sup> and Brazovskii<sup>176,177</sup>, respectively. Depending on  $\bar{\phi}_A$ , the phase transition in blends is first order (off-critical  $\bar{\phi}_A$ ) or second order (critical  $\bar{\phi}_A$ ). For critical  $\bar{\phi}_A$  the correlation length and magnitude of composition fluctuations diverge at the phase transition, following 3D Ising critical exponents<sup>171–175</sup>. In BCPs the Brazovskii mechanism always leads<sup>177</sup> to a first order ODT, for which reason such divergences do not occur. This mechanism also modifies<sup>177–179</sup> in BCP the “topology” of the phase diagram near ODT (comparing to MF predictions). Moreover, in disordered blends mesoscopic heterogeneities are characterized by a single

length scale, corresponding to the correlation length of composition fluctuations. In contrast, in a disordered BCP there is<sup>180</sup> an additional length scale on the order of the average chain extension, related to the wavelength of the emerging microphase-separated structure. This feature of BCPs is signified by a Lorentzian-like shaped structure factor of composition fluctuations<sup>147</sup>. Interestingly,<sup>181,182</sup> near the ODT disordered phases of lamellar- and cylinder-forming BCPs with short chains contain bicontinuous random networks. Each network is enriched in one of the blocks. Fluctuations of the network topology provide additional entropy, stabilizing the disordered phase<sup>182</sup>. It is unknown whether the properties related to charge transport differ in disordered blends and BCPs and, if so, which system is more suitable for PLED.

Motivated by the above question, we simulate the disordered morphologies of blends and BCPs containing typical semiconducting polymer poly(p-phenylene vinylene) (PPV) and insulating polymer polyacrylate. Based on the morphologies, we use a phenomenological percolation model to explore the influence of global polymer arrangement on macroscopic electrical conductance. The obtained results of blends and BCPs are compared to understand the differences between disorder phase of blends and BCPs. Additionally, it is useful for further experimental studies to know the effects of compositions and processing conditions on the electrical conductance. Therefore we also investigate their effects in both blends and BCPs by considering different compositions and processing conditions.

## 3.2 Model description

### 3.2.1 Mapping strategy

Our mesoscopic model represents an atomistic system containing  $n_A$  PPV and  $n_B$  polyacrylate homopolymers or blocks in a volume  $V$ . For both polymers, the general chemical structure of a monomer is shown in Fig. 3.2a. For brevity, we indicate the chemical identity of a homopolymer (or BCP block) with subscripts  $\alpha = A$  for PPV and  $\alpha = B$  for polyacrylate. Each homopolymer (block) is made of  $m_\alpha$  atomistic monomers; the molecular weight



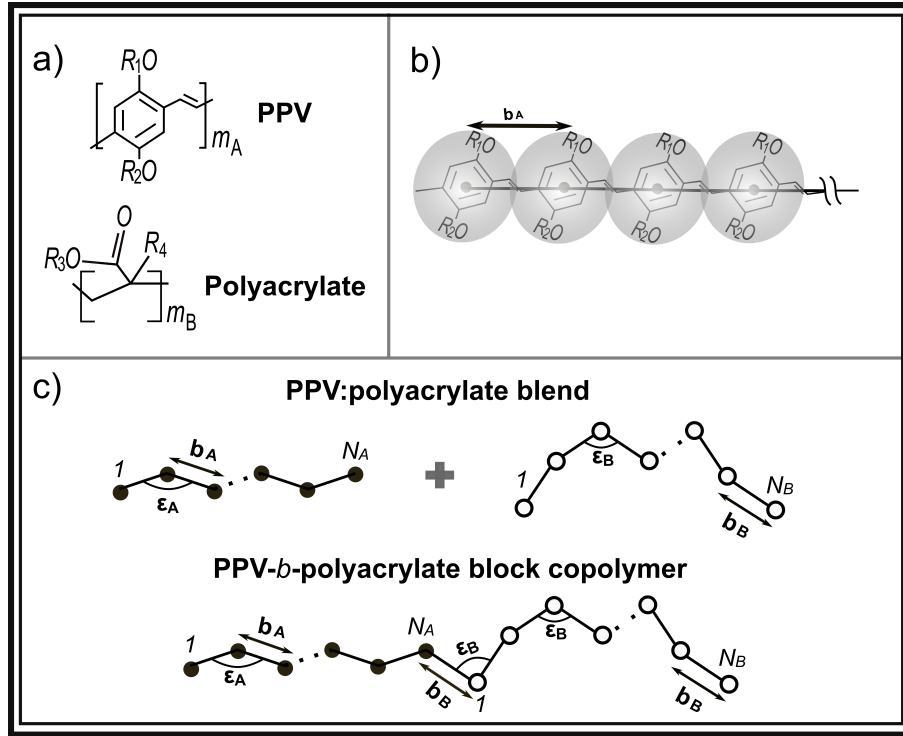


FIGURE 3.2: a) Chemical structure of PPV (top) and polyacrylate (bottom) monomers. For PPV  $R_1$  and  $R_2$  stand for alkyl substituents. For polyacrylates  $R_3$  is a small non-polar moiety while  $R_4$  denotes a  $-\text{H}$  or  $-\text{CH}_3$  group. b) Scheme used to map PPV (shown in an all trans configuration) on the discrete WLC model. Each atomistic monomer (gray sphere) is mapped on one interaction center (solid circle) placed at a junction or end-point of the WLC. c) Top: Sketch showing the representation of PPV and polyacrylate homopolymers in blends by WLC with  $N_A$  (solid circles) and  $N_B$  (open circles) beads, respectively. Angles between WLC bonds are controlled by stiffness parameters  $\epsilon_\alpha$ , while bond lengths are fixed to  $b_\alpha$ . Bottom: coarse-grained representation of PPV-*b*-polyacrylate BCPs obtained by covalently linking the WLC of PPV and polyacrylate homopolymers.

(MW) of each monomer is  $M_\alpha$ . The mass densities of pure PPV and polyacrylate phases are given by  $\tilde{\rho}_\alpha = m_\alpha n_\alpha M_\alpha / \mathcal{N}_A V_\alpha$ , where  $V_\alpha$  are the volumes that would be occupied by atomistic PPV and polyacrylate homopolymers (blocks) in their pure phase.  $\mathcal{N}_A$  is the Avogadro number.

Our coarse-graining procedure conserves the number of chains  $n_\alpha$  and the volume of each component  $V_\alpha$ . Each CG chain (block) is defined to reproduce key mesoscopic features of the molecular architecture of the atomistic chain (block). Considering that we can estimate the contour length  $L_\alpha$  and persistence length  $l_{p,\alpha}$  of the atomistic chains (blocks) from experimental studies,

we aim to conserve these two quantities. The target  $L_\alpha$  and  $l_{p,\alpha}$  are quantitatively reproduced by using the discrete WLC model. Each WLC is discretized by  $N_\alpha$  interaction centers, beads, connected by bonds with fixed length  $b_\alpha$ . The detailed description of WLC model has been already presented in section 2.2 and the bonded potential is given by the eq. 2.10.

To determine the  $N_\alpha$ ,  $b_\alpha$  and the bonded parameter  $\epsilon_\alpha$ , one needs three constraints on these three unknown parameters. The invariant quantities  $L_\alpha$  and  $l_{p,\alpha}$  provide two constraints, i.e.,  $L_\alpha = f(N_\alpha, b_\alpha)$  in eq. 2.15 and  $l_{p,\alpha} = g(b_\alpha, \epsilon_\alpha)$  in eq. 2.12. We introduce an additional constraint on  $N_\alpha$  based on the following considerations. First, to facilitate qualitative studies of charge transport, it is reasonable to use for the WLC, describing the electrically active component, a level of discretization which is comparable to the actual polymer. In spirit of earlier studies,<sup>183,184</sup> we assign physical meaning to A-type beads, assuming that  $N_A$  is equal to the number of atomistic PPV monomers (see Fig. 3.2b). This choice of  $N_A$  facilitates qualitative studies of charge transport within the electrically active component. The  $N_B$  are chosen in a way that the pure phase of coarse-grained polyacrylates has the same average number density of beads as the pure phase of the coarse-grained PPV, i.e. we impose the constraint  $n_A N_A / V_A = n_B N_B / V_B \equiv \rho_0$ . This specific choice of  $N_B$  simplifies the definition of non-bonded interactions (see eqs. 2.21 and 2.23). The additional constraint on the  $N_\alpha$  leads to the relationships:

$$N_A = m_A, \quad N_B = \frac{\tilde{\rho}_A}{\tilde{\rho}_B} \frac{m_B M_B}{M_A} \quad (3.1)$$

Provided that  $L_\alpha$ ,  $l_{p,\alpha}$ ,  $m_\alpha$ ,  $\tilde{\rho}_\alpha$  and  $M_\alpha$  of actual polymers are known experimental quantities,  $L_\alpha = f(N_\alpha, b_\alpha)$ ,  $l_{p,\alpha} = g(b_\alpha, \epsilon_\alpha)$ , and eq. 3.1 fully define the WLCs in our mesoscopic model, i.e., define the  $N_\alpha$ ,  $b_\alpha$  and  $\epsilon_\alpha$ .

### 3.2.2 Material-specific parameters and systems studied

To specify the input quantities for modeling, i.e.,  $l_{p,\alpha}$ ,  $L_\alpha$ ,  $m_\alpha$ ,  $\tilde{\rho}_\alpha$  and  $M_\alpha$ , we choose the PPV derivative poly[2-methoxy-5-(3',7'-dimethyloctyloxy)-1,4-phenylenevinylene] (MDMO-PPV) and poly(methylmethacrylate) (PMMA) as model systems. We emphasize that the conjugated polyaromatic backbone, as well as the alkyl substitution pattern of MDMO-PPV are representative for a broad range of non-polar polymeric (luminescent)

semiconductors commonly applied in optoelectronics. Similarly, PMMA represents a class of synthetically well-accessible insulating polymers, of which the polarity (and hence solubility with PPV) can be easily tuned by varying the alkoxy groups of the ester moieties. Hence, the parameterization established on the basis of MDMO-PPV and PMMA can be considered, at least, as qualitatively representative of a broad range of non-polar polymeric semiconductor:insulator mixtures.

We focus on the special case of blends with  $n_A = n_B$ , i.e. equimolar mixtures. We make this choice to facilitate direct comparison with their equivalent BCPs, where  $n_A = n_B$  by default. The atomistic PPV homopolymers (blocks) underlying the WLC model have  $m_A = 24$  monomers. The MW of an MDMO-PPV monomer is  $M_A \simeq 288$  g/mol, and we use for the mass density<sup>185</sup>  $\tilde{\rho}_A = 0.91$  g/cm<sup>3</sup>. We stress that considering such rather short PPV polymers is relevant from an experimental point of view. Typically, PPV derivatives exhibit poor solubility and processability if the MW is high.<sup>186</sup> For this reason synthetic strategies have focused on suppressing chain length and coupling defects,<sup>187</sup> in order to arrive at well-processable materials while exhibiting a high charge carrier mobility.

Different levels of dilution are realized by parameterizing the WLC model such that it describes long atomistic polyacrylate chains with  $m_B = 70, 138$ , and 300. The MW of each atomistic PMMA monomer is  $M_B \simeq 100$  g/mol and we set the mass density to  $\tilde{\rho}_B = 1.09$  g/cm<sup>3</sup>, which is a representative value for the polyacrylate family<sup>188</sup>. Blending PPV with these three polyacrylates induces dilutions that approximately correspond to mass ratios of 1:1, 1:2, and 1:4. In the following, we index all modeled blends and BCPs by these three mass ratios.

Having specified  $m_A$ ,  $M_A$ , and  $\tilde{\rho}_A$ , it is straightforward to calculate the average number density of CG beads  $\rho_0 = 1.9$  nm<sup>-3</sup>. The amounts of homopolymers (blocks) comprising a sample with volume  $V$  are:

$$n_A = n_B = \frac{\tilde{\rho}_A \tilde{\rho}_B V \mathcal{N}_A}{m_A M_A \tilde{\rho}_B + m_B M_B \tilde{\rho}_A} \quad (3.2)$$

The last set of material-specific parameters are contour lengths and persistence lengths, required as input for the LHS of  $L_\alpha = f(N_\alpha, b_\alpha)$  and  $l_{p,\alpha} = g(b_\alpha, \epsilon_\alpha)$ . Experimental data on the persistence length of MDMO-PPV are

TABLE 3.1: Parameters characterizing the discrete WLCs used in this study.

Dilutions	$b_A(\text{nm})$	$b_B(\text{nm})$	$N_A$	$N_B$	$\epsilon_A$	$\epsilon_B$
1:1		0.937		20		0.99
1:2	0.657	0.923	24	40	9.6	1.01
1:4		0.923		87		1.01

not available, so we set  $l_{p,A} = 6$  nm. This choice is motivated by data<sup>189</sup> on the persistence length of MEH-PPV, which has the same conjugated backbone and similar substitution pattern as MDMO-PPV. For PMMA we choose an experimentally known<sup>190</sup> value of persistence length  $l_{p,B} = 0.8$  nm. The provided persistence lengths illustrate that PPV derivatives are significantly less flexible than polyacrylates. Finally, contour lengths are obtained from  $L_\alpha = m_\alpha l_\alpha$ , where  $l_\alpha$  stands for the end-to-end distance of either atomistic monomer when the polymer is in the all-trans conformation. We estimate  $l_A = 0.657$  nm and  $l_B = 0.268$  nm based on the chemical structures of the PPV and polyacrylate backbone (see Fig. 3.2a), as well as geometric parameters such as bond lengths and angles. The latter are available from atomistic force-fields.<sup>191,192</sup> Table 3.1 summarizes the parameters of the WLC models for all homopolymers and BCPs considered in this study.

The approach just described fully define both chains and blocks in the blends or BCPs. For the covalent bond in BCPs, we set length of the covalent bond to be  $b_B$ , and the stiffness parameter controlling the angles formed by this covalent bond with its two neighboring bonds to be  $\epsilon_B$  (Fig. 3.2c). This choice is somewhat arbitrary, though we expect that penalizing the angle between the last PPV and the linking bond by  $\epsilon_A$ , instead of  $\epsilon_B$ , will not substantially affect our results. The reasons are two: our flexible polyacrylate blocks are long and we focus on disordered phases.

To support this statement, we performed MC simulations of BCPs in the ideal chain limit, i.e. where only bonded interactions  $\beta H_b$  are present, adopting the two different scenarios for the stiffness. Fig. 3.3a compares the orientational correlations of polyacrylate bonds with respect to the last PPV bond, for the two scenarios, in a BCP 1:1. Fig. 3.3b shows a similar plot for the BCP 1:4. We observe that the orientational correlations, for both scenarios, decay to zero along the contour of the polyacrylate WLC after a comparable number of bonds. Fig. 3.4a compares the distributions of the end-to-end distance,  $\rho(R_e)$ , in the BCP 1:1 for the two scenarios. Fig. 3.4b presents a similar plot

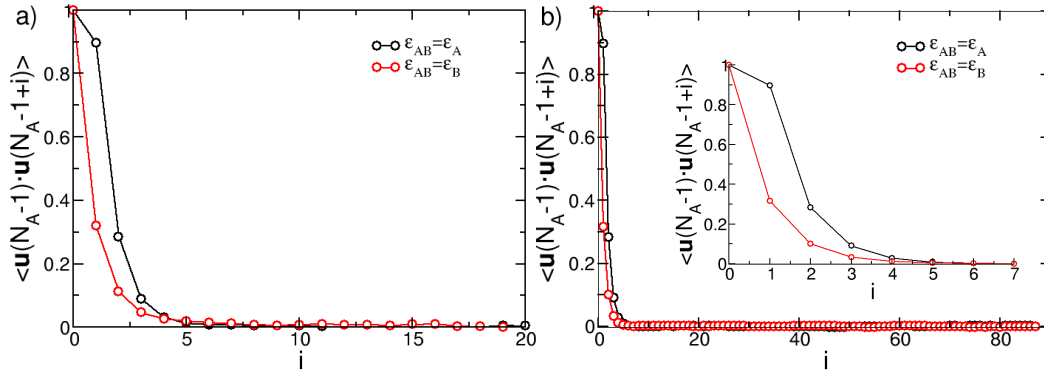


FIGURE 3.3: Average orientational correlations  $\langle \mathbf{u}(N_A - 1) \cdot \mathbf{u}(N_A - 1 + i) \rangle$  between the last PPV bond and the  $i$ -th polyacrylate bond (counting from the junction) in BCP 1:1 (left) and BCP 1:4 (right). The black and red curves correspond to different choice of the coefficient  $\epsilon_{AB}$  in the angular potential at the linkage between two blocks,  $\epsilon_{AB} = \epsilon_A$  and  $\epsilon_{AB} = \epsilon_B$ , respectively. The inset of panel b) is an enlarged view of the decay of correlations at small  $i$ .

for the BCP 1:4. The distributions  $\rho(R_e)$  for the two scenarios are indeed close to each other. Of course, modeling shorter BCPs might require more specific choices for the mesoscopic description of the linkage. Especially in a microphase separated state, the architecture of the linkage might influence the orientation of the blocks with respect to the interface.

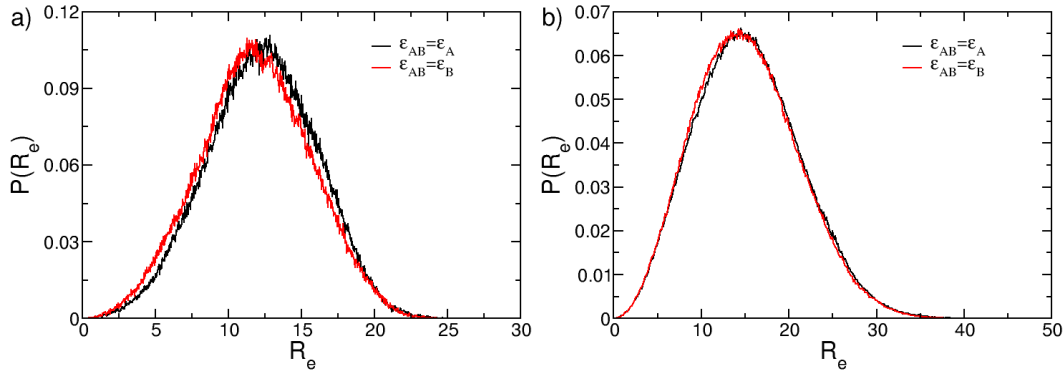


FIGURE 3.4: Distribution of end-to-end distance of block copolymers in BCP 1:1 (left) and BCP 1:4 (right) with different coefficient  $\epsilon_{AB}$  in the angular potential at the linkage between the two blocks.

### 3.2.3 Non-bonded interactions

The non-bonded interactions of multi-component systems, i.e., blends and BCPs, should account for limited compressibility of the polymer liquid and

incompatibility between unlike beads. We use the DFT-based interaction introduced in the section 2.2 to describe these non-bonded interactions. The PM scheme with zeroth-order assignment function described in the section 2.3 is employed to perform particle-based simulations on experimental scales. Therefore, the non-bonded potential  $H_{\text{nb}}$  is given by the eq. 2.23.

We need to specify the parameters within the  $H_{\text{nb}}$ , i.e., lattice spacing  $\Delta L$ , parameters  $\kappa$  and  $\chi$ . As discussed in the section 2.2, the  $\Delta L$  of the cubic lattice should not be significantly larger than the length-scales relevant to the studied problem. In this study, it is important to reproduce the molecular architectures of both stiff PPV part and flexible polyacrylate part. The relevant length-scale is the length of Kuhn segment  $l_{\text{k},\alpha}$  describing the chain stiffness, i.e. the length scale below which the chains can be considered (approximately) as stiff. Therefore, the lattice spacing  $\Delta L$  in this study should be not larger than the smallest Kuhn segments, i.e., the Kuhn segment of the polyacrylate chains ( $\sim 2l_{\text{p,B}} = 1.6$  nm). We define the lattice space  $\Delta L$  as 1.8 nm, which results in an average number of interacting particles  $\eta \approx 10$ . Relatively large  $\eta$  allows us to perform MF estimations for the CG systems. The parameter  $\kappa$  is chosen as 10. This choice of  $\kappa$  allows for high MC acceptance rates and reasonable relaxation times, while maintaining sufficiently low isothermal compressibility  $\kappa_{\text{T}}$  for the coarse-grained polymers. The  $\kappa_{\text{T}}$  is estimated according to eq. 2.17. For simplicity, we omit<sup>183,193,194</sup> the small contribution from chain translational entropy within the eq. 2.17, and assume that the average density  $\bar{\rho}_0$  is equal to the reference density  $\rho_0$ . The simplified expression of  $\kappa_{\text{T}}$  is  $\kappa_{\text{T}} = 1/k_{\text{B}}T\kappa\rho_0$ . For the representative temperature  $T = 423$  K we obtain  $\kappa_{\text{T}} \simeq 9 \times 10^{-9} \text{ Pa}^{-1}$ . This value is only marginally larger than the compressibility of actual polymeric liquids ( $10^{-9}$ – $10^{-10} \text{ Pa}^{-1}$ ). Different  $\chi$  parameters are employed to realize different strength of incompatibility. More details about the choice of parameter  $\chi$  will be given in the next section.

### 3.2.4 Simulation protocol

We perform MC simulations in the canonical ensemble. Our simulation protocol is inspired by a processing procedure, which is employed during laboratory scale experiments where PLED active layers are manufactured by spin-coating. To reduce non-equilibrium morphological features, caused by

fast drying, spin-coated layers are annealed at elevated temperatures (after the solvent has evaporated). After annealing, the structure of morphologies is solidified by a rapid quench. Multicomponent polymer systems are characterized by slow kinetics, originating from the combination<sup>195</sup> of thermodynamic barriers to mixing of different species, chain entanglements, and segmental friction (which depends on local environment). Therefore, non-equilibrium states may even survive long annealing times. For our materials, we assume that it is possible to qualitatively mimic the effects of thermodynamic barriers on morphology formation using only crankshaft move which reproduces Rouse-like pseudo-dynamics.

Assuming that the spin-coated structure used as a starting point for annealing experiments is disordered, we initiate our pseudo-dynamic MC simulations from configurations of disordered melts. Each MC run imitates an annealing process performed at a specific temperature. To mimic the implementation of different annealing temperatures in experiments, we simply employ different  $\chi$  parameters. As discussed in the section 2.2, parameter  $\chi$  is correlated with temperature and their relationship is described by a state-dependence function  $\chi(T)$ . For our model with complex molecules and drastic coarse-graining, nontrivial state-dependence function is expected. However, to mimic annealing at different temperatures it is sufficient to vary  $\chi$  considering it as a free input parameter, without specifying  $\chi(T)$ . We only assume that the dependence  $\chi(T)$  is identical for blends and BCP made of the same material. Of course, specifying  $\chi(T)$  becomes necessary for rephrasing observations made for different  $\chi$  in terms of actual temperature variations. We scan the region  $0 \leq \chi \leq \chi_{\max}$  with step  $\Delta\chi = 0.029$  and identify the  $\chi$ -values for which each blend or BCP remains disordered (details follow in Sec. 3.3.1 and Sec. 3.3.2).

Orthogonal to the electrodes, PLED active layers are finite systems with typical thickness of  $\sim 100$  nm. Therefore, we perform the simulations in cubic samples with edge lengths  $L \sim 100$  nm, and employ periodic boundary conditions (PBC) in all Cartesian directions. Technically, including free polymer surfaces and polymer/solid interfaces into our model to simulate the thin film condition is straightforward<sup>126,194,196</sup>. This extension would allow for a more realistic mesoscopic description of PLED layers at comparable costs of computation. However, explicit considerations of film geometry would



significantly expand the parameter space. Interfacial phenomena, e.g. surface segregation and conformational changes, are driven by a complex balance<sup>197</sup> between various entropic and enthalpic factors, which change across different systems. Therefore, the choice of the relevant parameters of the model, e.g. the strength of effective interactions with film boundaries, becomes much more materials specific. Hence just confining our blends and BCPs in  $z$ -direction without tuning the effective interactions at the interfaces guided by material-specific information, might not add realism. For the first study reported in this work, we investigate only the structural differences between blends and BCPs in the interior of PLED layers and it is sufficient to use the simple PBC for all dimensions.

In the following, we report results obtained for samples with  $L = 6 R_e$ , with  $R_e$  the root mean-square end-to-end distance of a BCP. In actual units, this choice is equivalent to  $L \simeq 74$  nm (1:1 dilution) and  $L \simeq 101$  nm (1:4 dilution). To provide a better feeling for the sizes of the modeled systems, we mention that the samples at 1:1 and 1:4 dilutions contain about  $7.8 \times 10^5$  and  $1.9 \times 10^6$  monomers, respectively. To estimate the influence of finite size effects when the system size is varied around  $\sim 100$  nm, we also consider samples with  $L = 5 R_e$  and  $7 R_e$  (for each dilution). For each  $\chi$ , the starting configuration is obtained from samples equilibrated at  $\chi = 0$ . During the simulations, the average acceptance rate of flip moves is about 50%. The annealing runs are long: the number of MC cycles is equivalent (at least) to ten decorrelation times for BCPs, i.e.,  $10 \tau_{\text{rel}}$ , and  $25 \tau_{\text{rel}}$  for blends. The decorrelation time  $\tau_{\text{rel}}$  is estimated when  $\chi = 0$ . For example, in 1:4 blends and BCPs  $\tau_{\text{rel}}$  approximately corresponds to  $5 \times 10^4$  and  $2 \times 10^5$  MC cycles, respectively.

### 3.3 Location of disordered phase

#### 3.3.1 RPA spinodals

Accurately locating the phase transition for each blend and BCP is outside the scope of our work. Such calculations would require advanced sampling techniques beyond the simple MC pseudo-dynamics realized in this study, as well as sophisticated finite-size scaling methods specific to first-order phase



transitions.<sup>198–200</sup> However, we need to estimate a region of  $\chi$ -values where we can assume that the disordered phase is stable in our simulations.

We approximate the boundary of the region of bare  $\chi$ -values where the disordered phase can be considered as stable in our simulations by the value of the bare  $\chi$  at the MF spinodal,  $\chi_s$ . To determine  $\chi_s$  we calculate within RPA the structure factor of composition fluctuations. The procedures of RPA calculation based on the potentials used in this study has been discussed in detail in section 2.5. The final expression of structure factor of composition fluctuations is given by the second formula of eq. 2.67. The involved quantities in eq. 2.67, i.e., eigenvalues  $\lambda_1, \lambda_2$  and components of orthogonal eigenvectors  $\tilde{v}, \tilde{v}$ , can be calculated through equations from 2.68 to 2.77. The only unknown quantities in these equations is the structure factor of composition fluctuations  $g_\alpha(q)$ . In this study, we numerically obtain the single-chain structure factors from a large ensemble of single chain conformations (see section 2.5). This ensemble is generated for WLC of PPV homopolymers, polyacrylate homopolymers, and BCPs, by adjusting our MC algorithm to sample conformations of ideal chains. Specifically, for this MC sampling we retain the bonded potential  $\beta H_{b,\alpha}$  and deactivate the non-bonded interactions  $\beta H_{nb}$ .

As discussed in section 2.5, RPA invokes several approximations<sup>120,201–203</sup>. Part of these simplifications occurs on small scales, where RPA neglects local correlations, e.g. monomer packing, and local fluctuations, present in the statistical mechanics of the CG model. To correct<sup>120,201–204</sup> for these local approximations the bare parameters  $\kappa$  and  $\chi$  entering  $S_{\text{RPA}}$  must be “renormalized”. Namely, the scattering in MC simulations should be approximated by  $S_{\text{RPA}}(q, \kappa_e, \chi_e)$  where the effective parameters are defined through functions  $\kappa_e = \kappa_e(\kappa, \chi)$  and  $\chi_e = \chi_e(\kappa, \chi)$ . The renormalized  $\kappa_e$  and  $\chi_e$  encapsulate contributions from local correlations and fluctuations. Even with renormalized parameters  $\kappa_e$  and  $\chi_e$ , the RPA accuracy is still limited<sup>120,201,203</sup> for finite chain lengths by approximations made on larger scales, such as assuming ideal chain statistics at  $\chi = 0$ , and neglecting long wavelength fluctuations (essentially the MF nature of the theory). With the chosen value of bare  $\kappa$ , the compressibility in our simulations is already small. Therefore, we assume that  $\kappa_e \simeq \kappa$  and consider only  $\chi_e \neq \chi$ . Provided that the function  $\chi_e(\chi)$  is known,  $\chi_s$  is extracted from the divergence of the scattering, i.e. from the condition  $1/S_{\text{RPA}}(q^*, \kappa, \chi_e(\chi_s)) = 0$ , where  $q^*$  is the modulus of the wavevector at which the structure factor has a maximum.

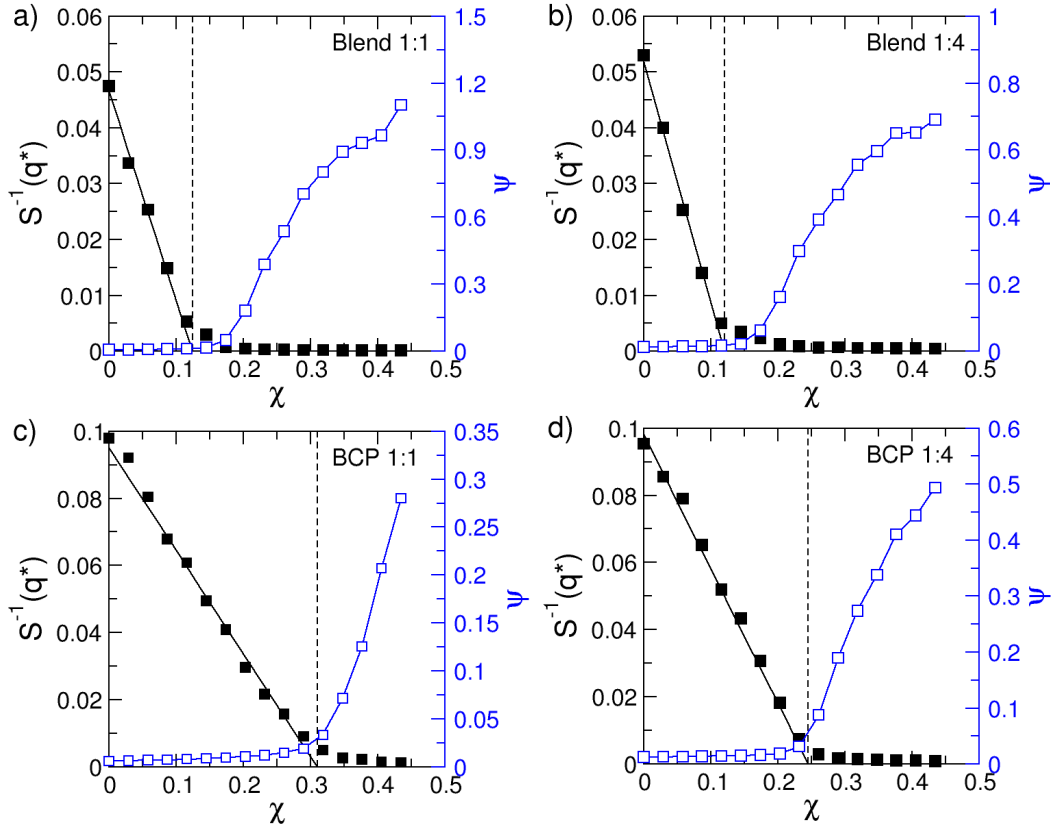


FIGURE 3.5: Structure factors (black squares) and order parameters (blue open squares) calculated from MC simulations for blends and BCPs at different dilutions indicated in each panel. Black solid lines show the RPA prediction:  $1/S_{\text{RPA}}(q^*, \lambda\chi_s)$ , where  $\lambda$  is a renormalization coefficient (see main text and Fig. 3.6). Black dashed lines indicate the location of RPA spinodals  $\chi_s$ . In blend 1:1, blend 1:4, BCP 1:1, and BCP 1:4,  $\chi_s = 0.1182, 0.1205, 0.3169$ , and  $0.2406$ , respectively.

To estimate  $\chi_e(\chi)$  we calculate, in our simulations, the structure factor:

$$S(q, \chi) = \frac{1}{N_{\text{(tot)}}} \left\langle \left| \sum_{i=1}^{N_{\text{A(tot)}}} \exp(-i\mathbf{q} \cdot \mathbf{r}_i) - \sum_{j=1}^{N_{\text{B(tot)}}} \exp(-i\mathbf{q} \cdot \mathbf{r}_j) \right|^2 \right\rangle \quad (3.3)$$

In eq. 3.3 the Cartesian components of the scattering vectors  $\mathbf{q}$  comply with PBC, i.e.  $\mathbf{q}_\gamma = 2\pi k_\gamma / L_{\text{box}}$ , where  $k_\gamma$  are integers. Angular brackets denote an average over system configurations and orientations of vector  $\mathbf{q}$ , at given  $\chi$ ; accordingly  $q = |\mathbf{q}|$ . For each  $\chi$ , we average over ten configurations taken from ten independent annealing runs, after the number of MC cycles becomes larger than  $25 \tau_{\text{rel}}$  (blends) and  $10 \tau_{\text{rel}}$  (BCP). Fig. 3.5 presents  $1/S(\tilde{q}^*, \chi)$  (open squares) extracted for blends and BCP, for two compositions: 1:1 (top panels) and 1:4 (bottom panels). For the blends  $\tilde{q}^* = 0$  whereas

for the BCPs  $\tilde{q}^*$  is finite. The “tilde” in the notation  $\tilde{q}^*$  indicates that, in general, the location of the scattering peak in simulations and RPA is different.

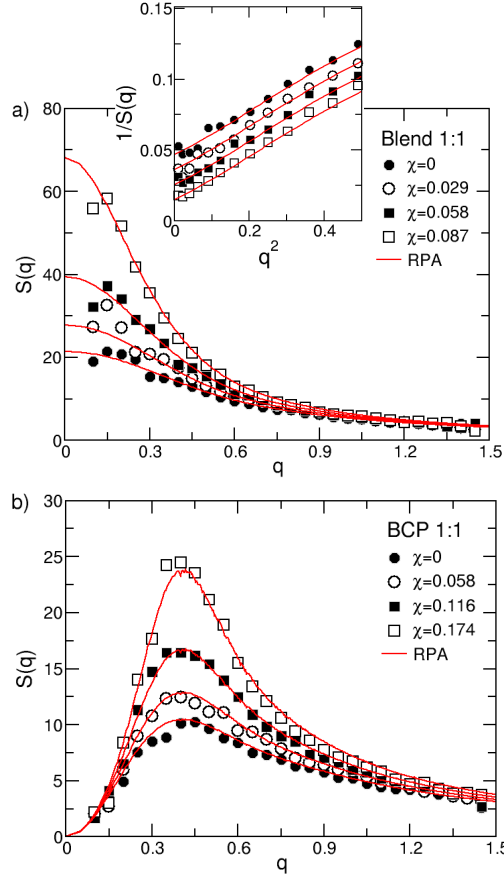


FIGURE 3.6: Examples of structure factors calculated from simulations (symbols) at  $\chi$ -values indicated by the legends, compared with RPA predictions (red solid lines). The latter are plotted based on an effective parameter  $\chi_e = \lambda\chi$ . For each mixture, the renormalization coefficient  $\lambda$  is a single fit parameter extracted by simultaneously fitting the RPA result to the set of structure factors available at the different  $\chi$ -values (see main text). Panel a: Structure factors for blends 1:1, where RPA predictions are obtained with  $\lambda = 0.734$ . The inset illustrates the linear relationship between  $1/S(q)$  and  $q^2$  in the regime of small  $q$ . Panel b: Structure factors for BCP 1:1. The RPA predictions are obtained with  $\lambda = 0.615$ .

For each system we assume that  $\chi_e$  is proportional to the bare parameter  $\chi$ , that is  $\chi_e = \lambda\chi$ . This simple renormalization can be understood as follows.<sup>202,203,205</sup> Within RPA the average energy (per monomer) penalizing mixing of unlike monomers is reduced to a MF term of random mixing  $E_{AB} = \chi\bar{\phi}_A\bar{\phi}_B$ , with  $\bar{\phi}_\alpha$  being the average volume fractions (see section 2.5).

This MF term does not account for basic correlations that are present in the MC simulations. Importantly, random mixing neglects that chain connectivity in weakly compressible polymer melts expels intermolecular monomers from the neighborhood of a test monomer and, consequently, reduces  $AB$  contacts. The prefactor  $\lambda$  corrects for the reduced effective coordination number of monomers. This linear renormalization of bare  $\chi$  is expected to be valid<sup>203–205</sup> for small  $\chi$ . We do not consider more sophisticated non-linear<sup>203,204,206,207</sup> renormalization which might be necessary for larger  $\chi$ .

The renormalization coefficient  $\lambda$  is extracted separately for each blend and BCP, by simultaneously fitting  $S_{\text{RPA}}(q, \lambda\chi)$  to a set of structure factors calculated from simulations conducted at several small  $\chi$ . We start with  $\chi = 0$  and choose empirically the largest  $\chi$  in the set. The choice is based on exploratory fits, taking into account that the quality of RPA deteriorates when immiscibility increases. Our fit minimizes the mean-squared error:  $\delta S^2 = \sum_{\{\chi\}} \sum_{\{q\}} [S_{\text{RPA}}(q, \lambda\chi) - S(q, \chi)]^2 / N_\chi N_q$ . The first summation is performed over the set of small  $\chi$ ;  $N_\chi$  is the total number of  $\chi$ -values in this set. The second summation is performed over  $N_q$  moduli of wave vectors for which the  $S(q, \chi)$  is available from simulations (for given  $\chi$ ). The good quality of the fits is illustrated in Fig. 3.6a and b, considering as examples 1:1 blends and 1:1 BCP, respectively. The two panels present the original structure factors calculated from simulations (symbols) for several  $\chi$  (indicated in the legends) and the fitted RPA prediction (red lines).

In structurally symmetric systems with flexible chains local correlations are affected by the polymerization degree  $N$ , e.g. the intermolecular correlation hole becomes more shallow as  $N$  increases, so that  $\lambda$  is also an  $N$ -dependent quantity. For these systems the  $N$ -dependence of  $\lambda$  is known.<sup>202,203</sup> It can be used to determine the effective FH parameter in the limit of infinitely long chains  $\chi_e = \lambda_\infty \chi$ , by extrapolating a sequence of  $\lambda$  extracted for different  $N$  to  $N \rightarrow \infty$ . For blends and BCPs as those considered in our study, such extrapolation procedures are currently not available. The  $\chi_e$  extracted from the procedure outlined in the previous paragraph, implicitly encapsulates local effects from system-specific features such as composition, asymmetry in molecular structure, and chain length.

In all panels of Fig. 3.5, we present the functions  $1/S_{\text{RPA}}(q^*, \lambda\chi)$  (solid black line) calculated from RPA after substituting the fitted  $\lambda$ . Interestingly, in BCP

the RPA provides a reasonable approximation for the peak of  $S_{\text{RPA}}(q^*)$  for immiscibilities well beyond the range of  $\chi$  used to fit of the entire structure factor (see Fig. 3.6). The required MF spinodal  $\chi_s$  is found at  $1/S_{\text{RPA}}(q^*, \lambda\chi_s) = 0$  and is indicated in the panels of Fig. 3.5 by a vertical dashed line.

### 3.3.2 Order parameters

How reliable is our approach to assume that the disordered phase is stable in our simulations for  $\chi < \chi_s$ ? The answer would have been simple for symmetric systems. There, within MF, the phase transition occurs at the critical point where the MF binodal and MF spinodal touch. Because fluctuations stabilize the disordered phase, the  $\chi$  at which the phase transition actually happens is larger than the MF  $\chi_s$ . Hence, for  $\chi \leq \chi_s$  the disordered phase is stable. The case of first-order transitions in our asymmetric systems is less straightforward. Thermal fluctuations still shift the actual binodal to higher  $\chi$ , comparing to the MF binodal. However, because the MF binodal and MF spinodal are now separated by the metastability region, the  $\chi$  where the phase transition actually happens may still be smaller than  $\chi_s$ . Such cases have been observed experimentally.<sup>208</sup> Therefore, the condition  $\chi < \chi_s$  does not guarantee the thermodynamic stability of the disordered phase, which motivates us to quantify the degree of order in our morphologies as a function of  $\chi$ .

We consider the MC trajectories accumulated at every  $\chi$  and calculate the order parameter:<sup>209</sup>

$$\psi = \frac{\Delta L^6}{V^2} \sum_{m=1}^{N_{\text{cell}}} \sum_{l=1}^{N_{\text{cell}}} [\langle \sigma_m \sigma_l \rangle - \langle \sigma_m \rangle \langle \sigma_l \rangle]^2$$

$$\text{where } \sigma_m = \frac{\hat{\rho}_A(\mathbf{c}_m) - \hat{\rho}_B(\mathbf{c}_m)}{\hat{\rho}_A(\mathbf{c}_m) + \hat{\rho}_B(\mathbf{c}_m)} \quad (3.4)$$

Here angular brackets denote an average over the same configurations that were used to calculate  $S(q, \chi)$ . The advantage of using the order parameter  $\psi$  is its sensitivity to order:<sup>209</sup> in a disordered phase (where correlations are short-ranged)  $\psi \sim V^{-1}$ , whereas in an ordered phase  $\psi \sim V^0$ .

Figs. 3.5a and b present (open blue squares)  $\psi$  as a function of  $\chi$  in the 1:1 and 1:4 blends. Figs. 3.5c and d provide similar plots for the 1:1 and 1:4 BCPs. We

do not display results for the 1:2 systems since they are qualitatively similar to the 1:4 case (see Appendix). In all plots,  $\psi$  increases substantially only when  $\chi \geq \chi_s$ , demonstrating that we can indeed consider morphologies with  $\chi < \chi_s$  as disordered. Actually, we expect that in our simulations some of the disordered morphologies near  $\chi_s$  are only metastable; long-lived metastability is facilitated by the slow Rouse-like pseudo-dynamics.

As expected (see section 3.1), Fig. 3.5 demonstrates that blends become ordered at lower values of  $\chi$  than their equivalent BCPs; in terms of actual experiments this behavior is equivalent to PPV:polyacrylate blends becoming ordered at higher temperatures (than the BCPs). Therefore, to compare these different materials on a common basis, it is meaningful to refer the strength of segregation not to  $\chi = 0$  but to their respective MF spinodals. In the following, all results will be reported in terms of the normalized  $\tilde{\chi} = \chi/\chi_s$ .

### 3.4 Sub-lattice polymer packing

As discussed in the section 2.3, PM schemes can lead<sup>21</sup> to artificial packing of material below the smallest physical scale of the model  $\Delta L$ , manifested by density variations within individual grid cells.

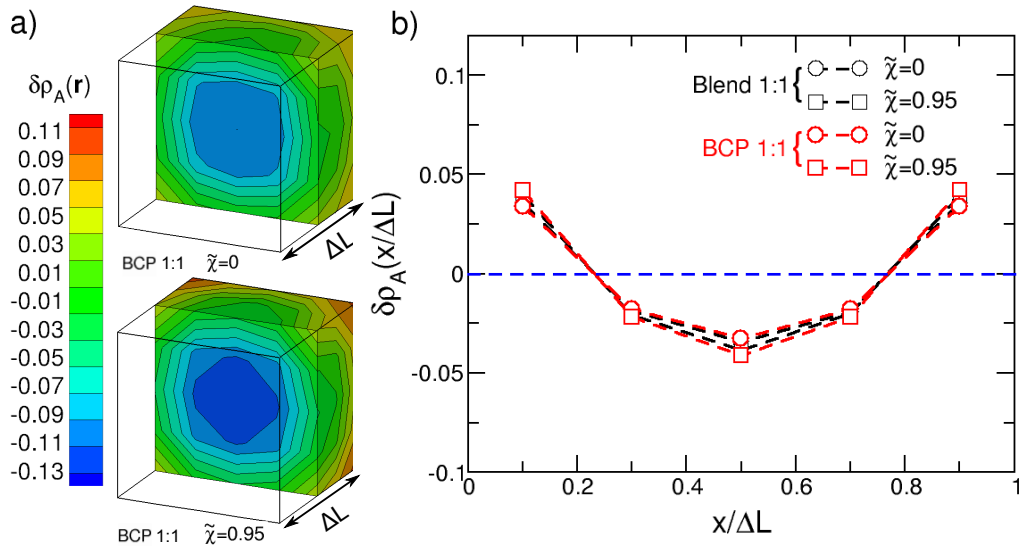


FIGURE 3.7: Panels a and b shows the three- and one- dimensional plots, respectively, quantifying the normalized density variation of PPV monomers within one lattice cell (see main text for details).

We explore the sub-lattice packing by quantifying the polymer distribution within a lattice cell for all disordered blends and BCPs. As an illustration, Fig. 3.7a presents 3D contour plots of normalized variation of local number density of PPV monomers,  $\delta\rho_A(\mathbf{r}) = \langle (\rho_A(\mathbf{r}) - \bar{\rho}_A) / \bar{\rho}_A \rangle$ , calculated for a 1:1 BCP. Here  $\mathbf{r}$  is a vector of coordinates inside a lattice cell and  $\bar{\rho}_A$  is the number density of PPV monomers averaged over this lattice cell. Angular brackets denote an average taken over all lattice cells in a large sample of morphologies (in this example, of 1:1 BCP). The plot in the upper panel of Fig. 3.7a considers the case  $\tilde{\chi} = 0$  demonstrating that PPV density inside a cell varies within 10–14 %. The bottom panel considers the case of strong segregation  $\tilde{\chi} = 0.95$  and we observe that the amplitude of sub-lattice density variations stays on the same order. Fig. 3.7b serves as an additional quantifier of sub-lattice structuring, presenting cross-sectional profiles of the PPV density variation in a cell. These profiles have been obtained for the 1:1 blend and BCP for  $\tilde{\chi} = 0$  and 0.95, by calculating the 1D analog of  $\delta\rho_A(\mathbf{r})$ . The amplitude of the 1D density variation of  $\sim 0.04$  % is about an order of magnitude larger than in previous studies<sup>21</sup> based on a discrete Gaussian model. Presumably, the stronger sub-lattice packing in our case is promoted by the WLC architecture and the somewhat smaller  $\bar{N}$ . Importantly, Fig. 3.7b demonstrates that the sub-lattice packing responds only weakly to increasing  $\tilde{\chi}$  and is very similar in blends and BCP having the same dilution.

In Sec 3.6 we will demonstrate that the PM-related artefacts in microscopic materials structure, quantified in Fig. 3.7, have no qualitative effects on our analysis of percolation properties.

### 3.5 Local composition in blends and BCP

We identify qualitative differences in the structure of disordered morphologies of our blends and BCPs by analyzing the local environment of PPV and acrylate monomers. Inspired by earlier studies<sup>210,211</sup> of symmetric blends and BCPs, we calculate the volume fraction  $\phi_A$ , of PPV monomers in the surroundings of each PPV and acrylate monomer. This volume fraction equals a number fraction calculated as:<sup>210,211</sup>  $\phi_A = \Sigma_A / (\Sigma_A + \Sigma_B)$ . Here  $\Sigma_A$  and  $\Sigma_B$  are, respectively, the number of intermolecular PPV and acrylate neighbors of a test (PPV or acrylate) monomer. Considering intermolecular neighbors



only, filters out<sup>211</sup> effects from trivial contributions to monomer concentration in the local environment caused by chain connectivity.

We calculate  $\Sigma_A$  and  $\Sigma_B$  by summing particles that are found in a spherical control volume centered at the test particle, i.e. we sum particles that are closer than a cutoff radius,  $r_c$ . To obtain physically meaningful information on the local environment, unbiased by sub-lattice structure (see discussion in section 3.4) we choose  $r_c = 2\Delta L$ , which is larger than the lattice spacing.

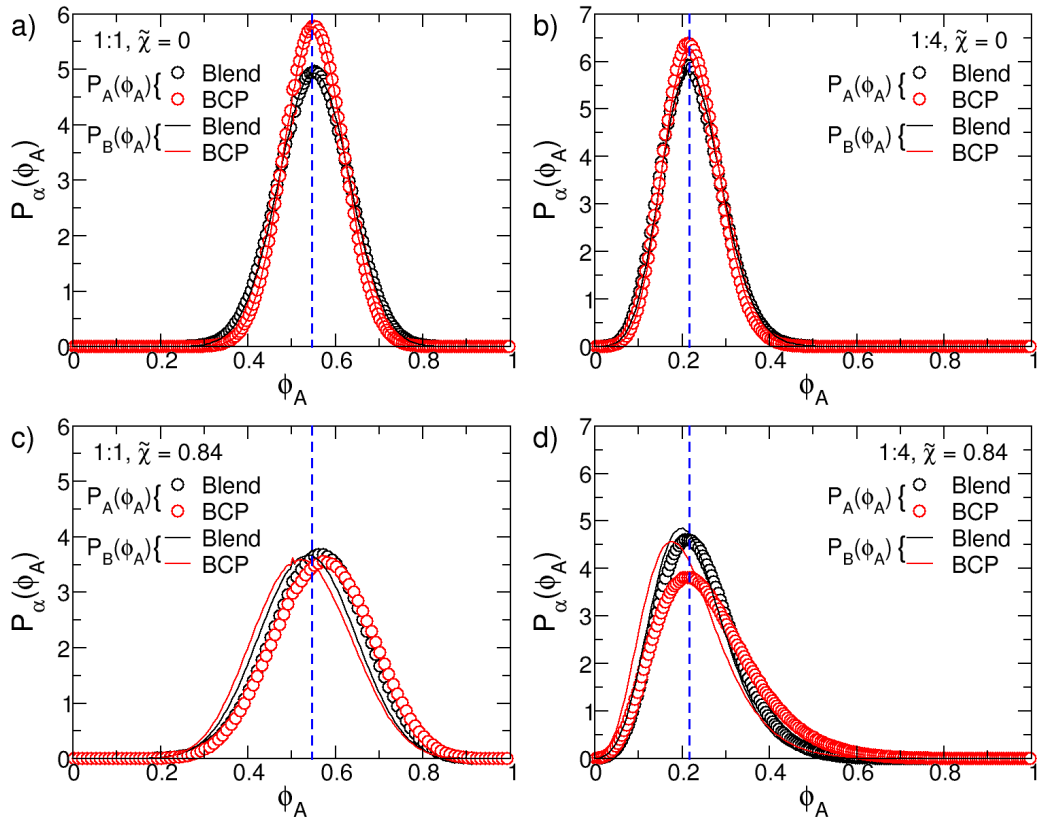


FIGURE 3.8: Probability distributions  $P_\alpha(\phi_A)$  for the volume fraction of PPV monomers in a spherical volume surrounding a test PPV ( $\alpha = A$ , circles) or polyacrylate ( $\alpha = B$ , lines) monomer. Each of the four panels compares the distributions  $P_\alpha(\phi_A)$  for blends and BCPs at the same composition and normalized  $\tilde{\chi}$  value, indicated in the panel. Vertical dashed lines correspond to the average volume fraction of PPV monomers in a completely homogeneous mixture.

Fig. 3.8 presents the probability distribution  $P_\alpha(\phi_A)$  quantified around PPV ( $\alpha = A$ , circles) and acrylate ( $\alpha = B$ , lines) monomers. We report results for the 1:1 and 1:4 dilution (left and right panels, respectively). For each dilution, two representative segregations are considered: far ( $\tilde{\chi} = 0$ ) and near the MF spinodal ( $\tilde{\chi} = 0.84$ ). For  $\tilde{\chi} = 0$  (see Figs. 3.8a,b) the distributions  $P_A(\phi_A)$  are



indistinguishable from  $P_B(\phi_A)$  in both blends and BCPs. The slight difference in the width of the distributions calculated in blends and BCPs suggests that local composition fluctuations in the former are somewhat stronger than in the latter. For  $\tilde{\chi} = 0$  the maximum of all distributions is found at the average number fraction of PPV monomers in the system (indicated by the vertical dashed line). In Figs. 3.8c,d the distributions  $P_A(\phi_A)$  and  $P_B(\phi_A)$  become distinguishable, demonstrating that the local segregation in the disordered phase increases as  $\chi$  becomes larger. This trend is consistent with previous studies.<sup>210,211</sup> For the more asymmetric 1:4 systems the difference in local segregation between blends and BCPs becomes evident even from simple visual inspection of their morphologies. As an illustration, the left column of Fig. 3.9 shows instantaneous configurations of the 1:4 blend and the 1:4 BCP, that have been considered in Fig. 3.8d. In the BCP morphology PPV blocks (yellow color) show a stronger tendency for clumping together, comparing to the blend. To demonstrate more clearly the segregation in these configurations, we divide the simulation box into cubic cells with length  $2\Delta L$ , calculate the number density of PPV monomers in each cell, and extract the instantaneous density distribution. The right column of Fig. 3.9 shows a random slice of the 3D density distribution for the blend and the BCP. We observe that the density distribution in the BCP is more heterogeneous than in the blend.

For a more quantitative comparison of local environments in blends and BCPs it is useful to consider the quantity:

$$\Delta I(\phi_A) = \int_{\phi_A}^1 \left[ P_{A, \text{BCP}}(\phi'_A) - P_{A, \text{blend}}(\phi'_A) \right] d\phi'_A \quad (3.5)$$

Here we introduce an additional index to indicate the type of the material (blend or BCP) where  $P_A(\phi_A)$  was calculated. The meaning of  $\Delta I(\phi_A)$  is transparent: it quantifies the difference between BCPs and blends in probability to observe a local volume fraction larger than  $\phi_A$ .

Figs. 3.10a and b show plots of  $\Delta I(\phi_A)$  at several representative values for  $\tilde{\chi}$ , for dilutions 1:1 and 1:4, respectively. The plots demonstrate that for segregations  $\tilde{\chi} > 0.5$  the probability to observe large values of  $\phi_A$  is higher in BCPs than in blends, for the same distance from the MF spinodal. In other words, the local segregation in the disordered morphologies of BCPs is stronger. This trend is more pronounced in the more asymmetric 1:4 mixtures.

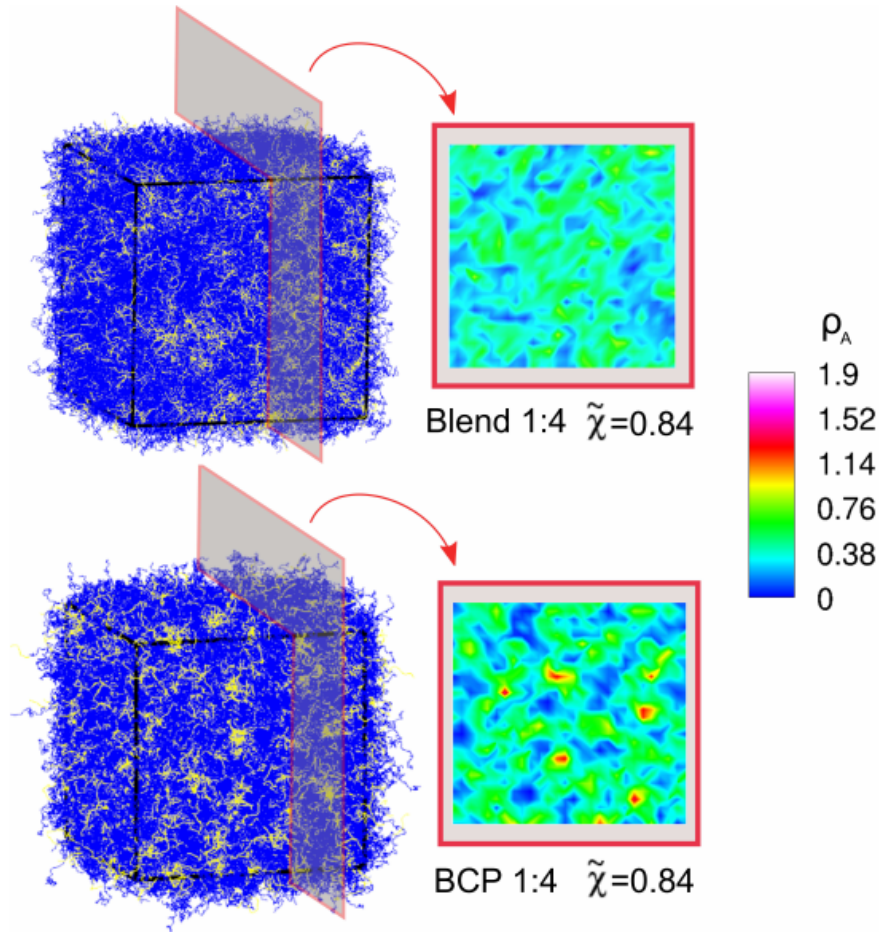


FIGURE 3.9: Left column: representative configurations of a 1:4 blend (top) and a 1:4 BCP (bottom) obtained from our hybrid simulations at  $\tilde{\chi} = 0.84$ . PPV and polyacrylate chains (blocks) are colored with yellow and blue, respectively. Right column: two slices of the instantaneous 3D contour plot of the local number density of PPV monomers calculated for the configuration of the blend (top) and BCP (bottom).

Finding stronger local segregation in disordered BCPs than in blends (at the same  $\tilde{\chi}$  and dilution) suggests that in the latter the effect of electron trap alleviation by blending may be more pronounced than in the former. However, we emphasize that the MH relation for the trap-limited current density<sup>166</sup> (see section 3.1) is not sufficient for verifying this hypothesis. Although the MH model has served to explain in what way a trap-limited current in an organic semiconductor is enhanced by spatially separating transport and trap sites,<sup>165,167</sup> it remains a macroscopic theory. By construction, it considers only the global average of the semiconductor concentration and overlooks any effects related to local inhomogeneities in composition.

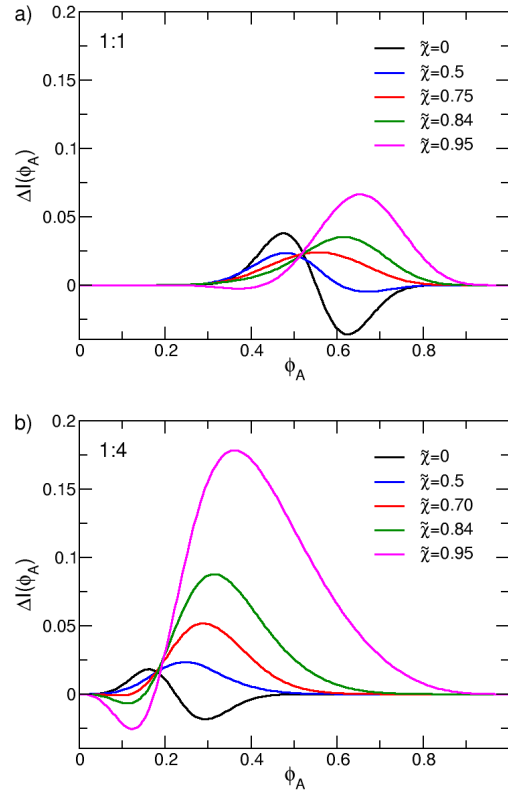


FIGURE 3.10: Difference between BCPs and blends in probability to observe, in the surroundings of a test PPV monomer, a volume fraction of PPV monomers larger than  $\phi_A$ , see eq. 3.5. In both panels, the probability difference is denoted by  $\Delta I(\phi_A)$  and is plotted as a function of the threshold value  $\phi_A$ . Panel a shows  $\Delta I(\phi_A)$  calculated for BCPs and blends with dilution 1:1 found at the same normalized  $\tilde{\chi}$ , indicated by the legends. Panel b is similar to panel a but refers to BCPs and blends with dilution 1:4.

### 3.6 Percolation analysis

In this section, we identify structural differences between disordered blends and BCPs concerning the spatial distribution of the charge conducting PPV component over large scales. Our approach attempts to establish a qualitative link to electric conductivity. The analysis assumes that we are dealing with solid-state structures corresponding to vitrified instantaneous configurations of an annealed morphology. Whenever we refer to  $\chi$ , we implicitly mean the value of  $\chi$  (equivalently the temperature) at which annealing was performed. Because we are interested in disordered morphologies, we focus on the range  $0 \leq \tilde{\chi} \leq 1$ .

We identify conducting clusters of PPV monomers through a percolation analysis in spirit of qualitative charge transport models<sup>212–214</sup>. First, we take into account that our PPV homopolymers (blocks) are semiflexible, since they are only slightly longer than a single PPV Kuhn segment. Considering the restricted conformational freedom, we make the approximation that there are no conjugation breaks along the entire PPV backbone of the homopolymers or blocks. Therefore each PPV homopolymer (block) is a single charge-carrier transport site. Within this picture, electric conductivity is limited only by factors disrupting interchain charge transfer. To group transport sites into conductive clusters we postulate that charges can hop between two PPV homopolymers (blocks) only if the minimum distance between these homopolymers (blocks) is smaller than a hopping threshold  $d$ . With this criterion in hand, it is straightforward to identify the conductive clusters using an “ants-in-labyrinth” algorithm<sup>215</sup> with PBC. We determine the minimum distance of two PPV homopolymer (blocks) by comparing the distances within all possible intermolecular pairs formed by their monomers.

From the perspective of the Miller-Abrahams model<sup>41,216–219</sup> it is tempting to interpret  $d$  as a characteristic cutoff distance at which the charge tunneling probability between two conjugated segments has exponentially decayed to an extent that they can be considered as electrically decoupled.<sup>220</sup> Yet, the nanoscale structure of morphologies in our model and real materials differs significantly because of drastic coarse graining, soft potentials, and grid-based calculation of interactions. Therefore, it is not meaningful to quantitatively compare the  $d$  at which percolation occurs in our samples with length scales typical to charge transport in real systems, such as the localization length<sup>221</sup>.  $d$  should rather be seen as a phenomenological parameter. Still, we can quantify similarities or differences across morphologies, for example, by systematically comparing the properties of conducting clusters identified at a value of  $d$  which is fixed across different systems.

We focus on the spanning probability,  $P_s$ , and percolation probability,  $P_c$ . A cluster is classified as spanning when it connects two opposite sides of the sample, at least, along one of the three Cartesian directions. The spanning probability is calculated as the frequency of observing a spanning cluster in a set of independent morphologies obtained for a fixed set of system parameters, i.e. class of material (blend or BCP), degree of dilution, and  $\chi$ . Specifically,  $P_s = n_s/n_o$  where  $n_s$  is the number of spanning clusters observed in  $n_o$  independent simulations. The error in estimating  $P_s$  is given

by<sup>222</sup>  $\delta P_s = \sqrt{P_s(1 - P_s)/n_0}$ .

Percolation transitions are subjected to finite system size effects.<sup>199</sup> In an infinite system,  $P_s$  is a step function of the geometrical parameter controlling percolation, i.e.  $P_s$  is zero or unity, whereas in finite systems it grows and saturates smoothly around the percolation threshold. In this work we are explicitly interested in a percolation analysis that includes effects of a finite system size, because (as has been elaborated previously) PLED layers themselves have finite dimensions, especially in the vertical coordinate.

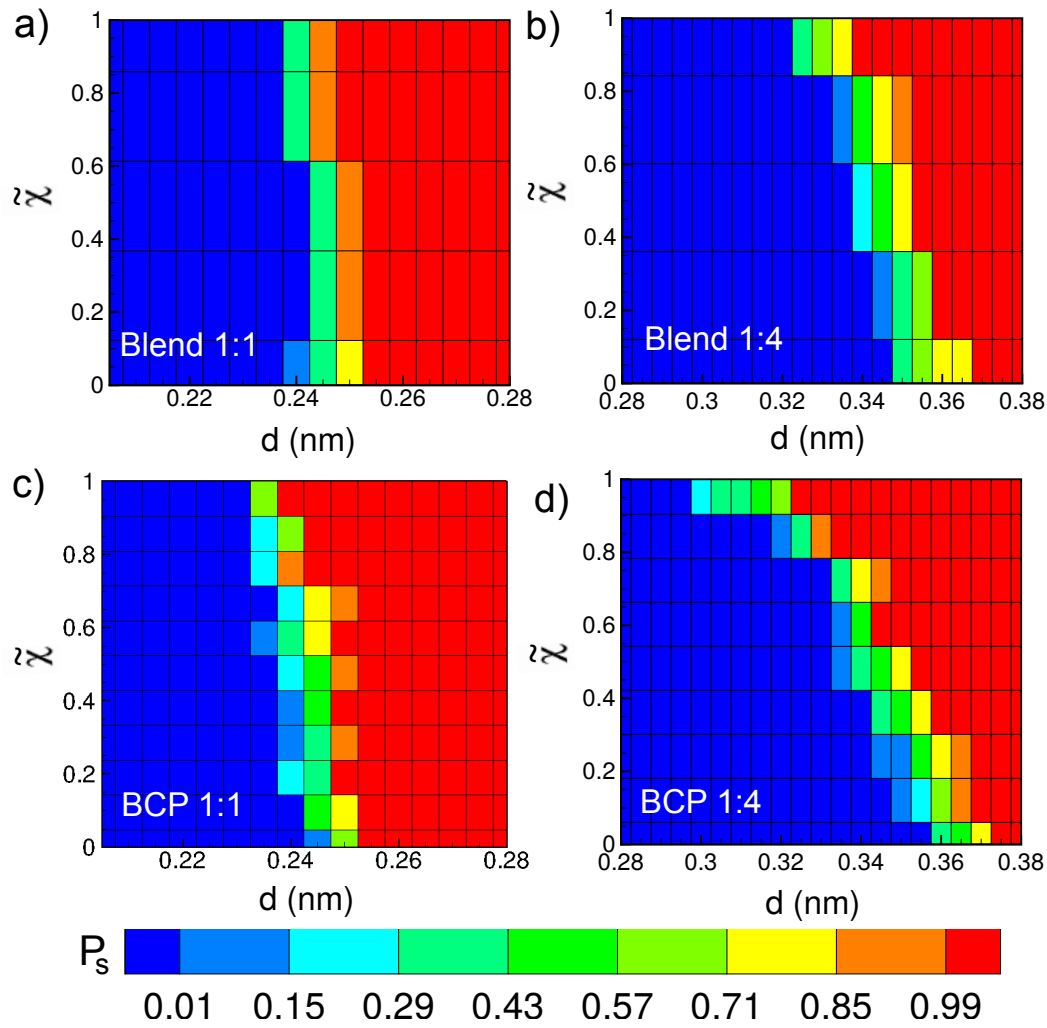


FIGURE 3.11: Contour plots quantifying the probability,  $P_s$ , to observe a spanning PPV cluster in disordered blends and BCPs as a function of normalized  $\chi$  and hopping threshold  $d$ . Blue and red colors correspond to low and high probabilities, respectively. The type of the mixture is indicated at each panel.

Figs. 3.11a–d present contour plots quantifying  $P_s$  as a function of  $d$  and  $\chi$  for blends and BCPs. Mixtures with weight fraction 1:1 are presented in

Figs. 3.11a, c while the 1:4 case is addressed in Figs. 3.11b, d. For each  $(d, \tilde{\chi})$  pair, the  $P_s$  has been extracted from 10 independent morphologies. The resolution of the color map is consistent with the error estimate  $\delta P_s$ . For each fixed  $\tilde{\chi}$ ,  $P_s$  varies with  $d$  as expected. Small  $d$  lead to  $P_s = 0$ , i.e. the systems are always non-conducting, whereas a large  $d$  results in  $P_s = 1$ , i.e. the systems are always conducting. Between the two extremities, there is a rather narrow region of  $d$ -values where  $0 < P_s < 1$ . In our contour plots, this region is indicated by the multicolored band and stems from finite system size effects.

For  $\tilde{\chi} = 0$  the percolation transition in our blends and BCPs occurs at about the same value for  $d$ , provided that the degree of dilution is the same. This trend is consistent with the local environment analysis for  $\tilde{\chi} = 0$  (see Figs. 3.8a, b) where the distribution  $P_A(\phi_A)$  in blends was found to be only marginally broader than in their corresponding BCPs. However,  $P_s$  behaves qualitatively different for blends and BCPs when  $\tilde{\chi} > 0$ . In blends, we observe that the position of the  $d$ -boundary, separating non-conducting and conducting regimes, changes with  $\tilde{\chi}$  only weakly. In contrast, for the BCPs the boundary shifts substantially towards smaller  $d$ , as  $\tilde{\chi}$  increases to reach  $\tilde{\chi} = 1$ . This effect is particularly evident for more diluted 1:4 BCP, where the boundary shifts between  $\tilde{\chi} = 0$  and  $\tilde{\chi} = 1$  by about 15 %. The results obtained for the 1:2 dilution are consistent with this statement and can be found in Appendix. These qualitative differences in the behavior of  $P_s$  in blends and BCPs are consistent with our conclusions from Figs. 3.8 and Figs. 3.10 that disordered blends are locally less segregated than BCPs (as  $\tilde{\chi}$  increases towards  $\tilde{\chi} = 1$ ). The observation that increasing  $\tilde{\chi}$  strongly promotes the formation of a percolating PPV phase in BCPs, is consistent with the build-up of a disordered fluctuating network-like morphology.<sup>181,182</sup>

It should be emphasized that the above percolation analysis is insensitive to the choice of chain discretization. The obtained results are qualitatively same with a moderate, at least, modification of bond length  $b_{\text{PPV}}$ . To prove this, we perform the same percolation analysis based on systems with different discretization of PPV chains (blocks). Performing the entire set of simulations using a model with different chain discretization would require substantial computational time. Therefore, we obtain simple insights from an alternative approach. The PPV chains (blocks) in the configurations of blends and BCPs that have been already equilibrated with the old WLC model are

coarse-grained into chains (blocks) with segmental length of  $2b$ . The substituting monomer is placed at the center of mass of the coarser bond. An example of original and "decimated" WLC is shown in Fig. 3.12. The results of percolation analysis based on the decimated WLCs in blends 1:4 and BCPs 1:4 are shown in Fig. 3.13. Compared with the original percolation behavior (Fig. 3.11 c and d), the new results deliver, qualitatively, the same trends. The only difference is that for the coarser description, the values of the phenomenological parameter  $d$  that are relevant for percolation become larger. This shift is caused by the convention we use to define the minimum distance of two PPV chains (blocks) during percolation analysis. As has been already mentioned, we find this distance by looping over all pairs of monomers of the two blocks. Obviously, the fewer monomers of decimated chains are more sparsely distributed in space than in the case of the original WLC.

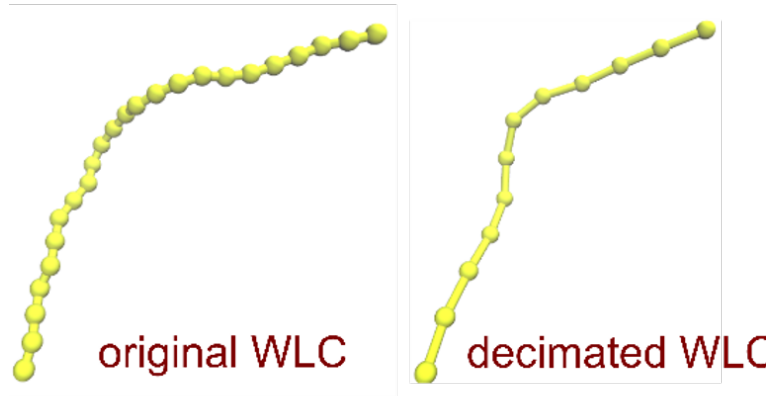


FIGURE 3.12: An illustration of the original (left) and "decimated" (right) WLC describing PPV.

We observe that all changes in percolation occur for  $d \ll \Delta L$ . Therefore we also need to verify that the observed trends do not originate from the model-specific sub-lattice polymer packing quantified in Sec. 3.4 but stem from generic physical mechanisms. We perform this test through an alternative, more coarse-grained, percolation analysis<sup>223</sup> which involves length scales larger than  $\Delta L$  and excludes, therefore, artefacts from sub-lattice polymer packing. Specifically, we discretize the volume of each morphology (see section 3.5 and Fig. 3.9) by a cubic mesh with spacing  $2\Delta L$ , i.e. twice as large as that of the original lattice in the MC simulations used to prepare these



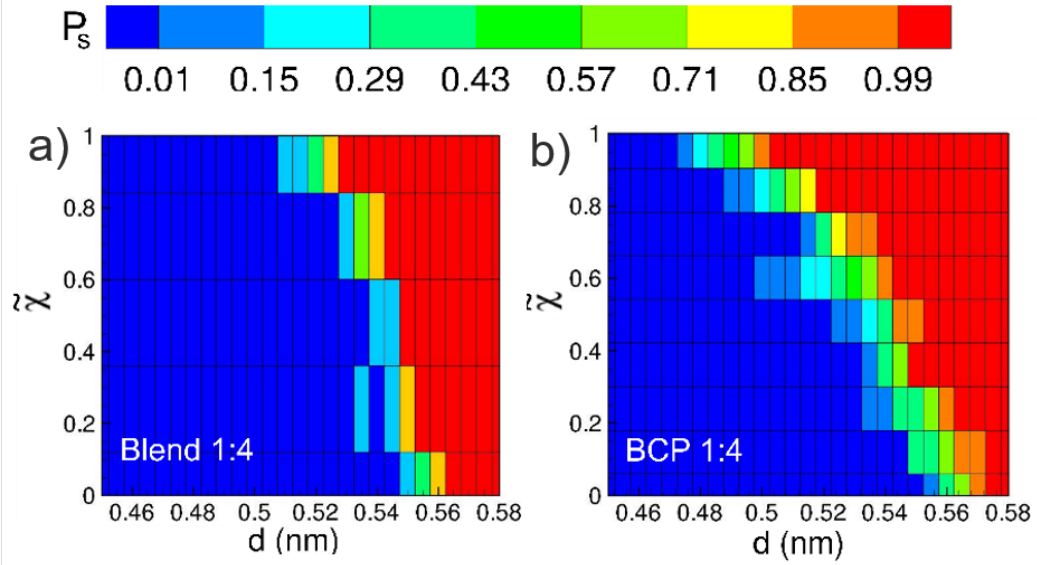


FIGURE 3.13: Probability  $P_s$  for observing a spanning cluster in disordered blend 1:4 and BCP 1:4. The results are calculated based on decimated configurations. Blue and red colors correspond to low and high probabilities, respectively. In each panel,  $P_s$  is calculated as a function of normalized  $\chi$  and hopping threshold  $d$ .

morphologies. The cells of this superlattice are colored black or white depending on whether or not the number density of PPV monomers in a supercell is larger or smaller than a threshold density  $\rho_{th}$ . The 3D lattice-based graphs are screened for percolation using the “ants-in-labyrinth” algorithm with the criterion that two neighboring lattice cells are connected if they have the same color. The criterion considers cells that are nearest neighbors only and accounts for PBC.

Figs. 3.14a–d report the  $P_s$  from the lattice-based analysis. To present the results in the same format as Figs. 3.11a–d we do not report  $\rho_{th}$  on the abscissas, but seek a derived variable which has the same physical meaning as  $d$ . We consider that<sup>224</sup> in a large volume, containing randomly oriented slender rods with density  $\rho_r$  and length  $\lambda_o$ , the average minimum distance between rods is  $d_{min} \simeq 2/\pi\rho_r\lambda_o^2$ . Let  $g$  be the average number of monomers that a single PPV block has in a lattice cell. To first approximation  $g$  is a constant, determined by geometrical parameters:  $L_A$  and  $\Delta L$ . Substituting  $\rho_r = \rho_{th}/g$  and  $\lambda_o = gb_A$  transforms  $\rho_{th}$  into an equivalent minimum threshold distance  $d_{min} \simeq 2/\pi\rho_{th}gb_A^2$ . Therefore, we display on the abscissa axes in Fig. 3.11 the variable  $1/b_A^2\rho_{th}$ . We neglect all prefactors because the estimate is qualitative, e.g. we use the approximation of slender rods and apply the original



expression for  $d_{\min}$  to the rather small volumes of individual lattice cells.

The coarser lattice-based analysis confirms the trends obtained from the continuum-space analysis – Figs. 3.11e–h are qualitatively similar to the patterns reported in Figs. 3.11a–d. Of course, the continuum-space analysis is a more general method and allows for various extensions. For example, intramolecular breaks in conjugation can be included, because individual molecules are explicitly considered (and not just densities).

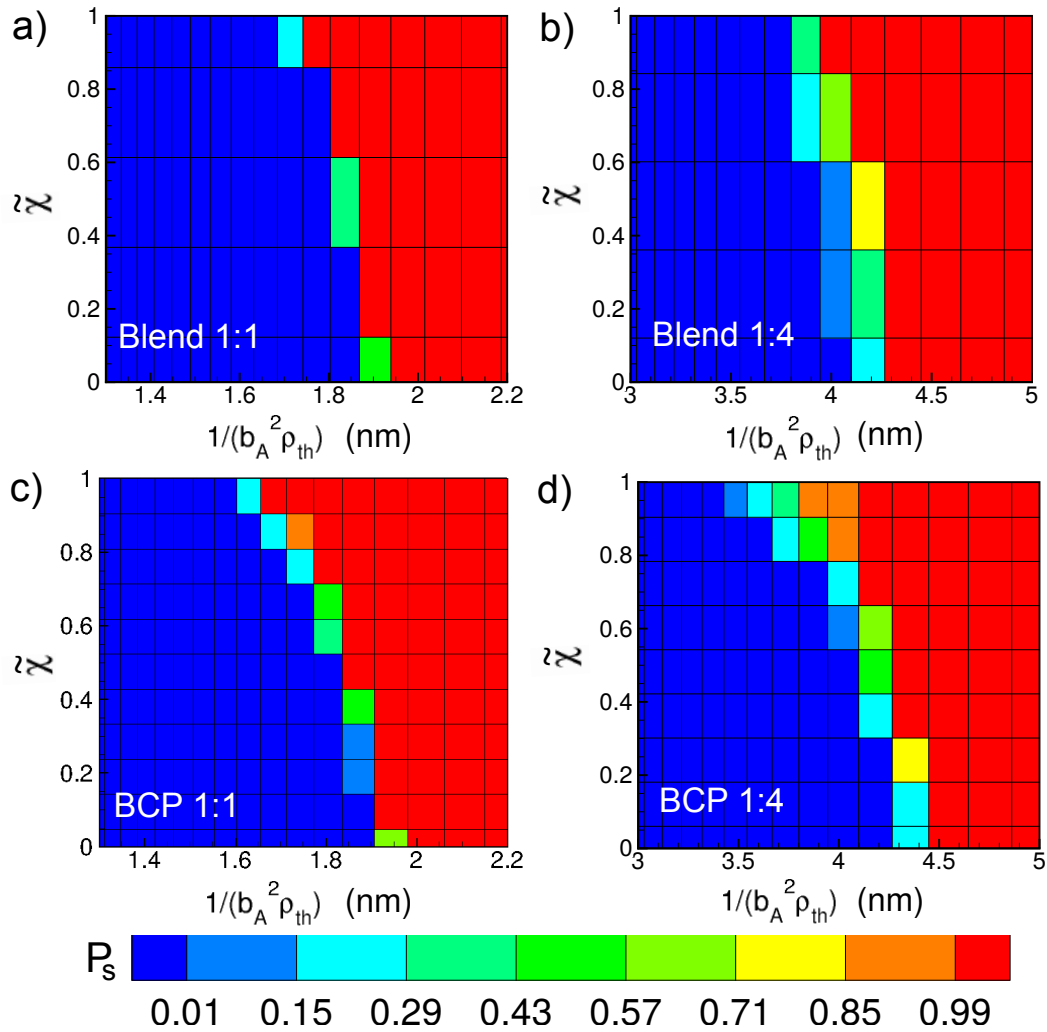


FIGURE 3.14: Contour plots quantifying the probability,  $P_s$ , to observe a spanning PPV cluster in disordered blends and BCPs as a function of normalized  $\chi$  and density threshold  $\rho_{th}$ . Blue and red colors correspond to low and high probabilities, respectively. The type of the mixture is indicated at each panel.

Although  $d$  acts in Figs. 3.11a–d as an adjustable phenomenological parameter, we can make qualitative estimates concerning effects of annealing temperature on the conductance of disordered PLED layers, prepared in experiments. Namely, the weak dependence of percolation threshold on  $\tilde{\chi}$  in blends suggests the following hypothesis. Suppose that the concentration of insulating polymer is such that there is no flow of current through active layers prepared by annealing the blend at a given temperature. Then it is unlikely that macroscopic conductance will be recovered by preparing the layers at lower annealing temperatures (but still above the phase transition). The situation in BCPs is radically different. Because increasing  $\tilde{\chi}$  substantially reduces the maximum hopping length required for percolation, annealing these materials at lower temperatures may recover conductance. The practical consequence of the finite system size effects on the percolation transition in both blends and BCPs (multicolored bands in Fig. 3.11) can be understood as follows: if, because of materials parameters or processing conditions, PLED layers are found near a percolation transition, their electronic properties may not be reproducible: conducting and non-conducting samples will be randomly mixed within a single batch.

We remind that in our simulations blends and BCPs, at the same dilution, have the same physical size and number of particles. Therefore, they are compared in Figs. 3.11 on equal basis, as far as finite system size effects are concerned. We performed the same analysis for systems with box sizes  $L = 5 R_e$  and  $7 R_e$ . As expected, increasing  $L$  makes the percolation transitions sharper; the multicolored bands in Fig. 3.11 become narrower. At the same time, the overall shape of the boundary between blue (non-percolating) and red (percolating) areas is conserved. In other words, increasing the system size does not change our conclusions, provided that  $L$  stays on the scale of  $\sim 100$  nm.

### 3.7 Summary and outlook

We performed mesoscopic computer simulations of *disordered* morphologies of blends of semiconducting and insulating homopolymers and their equivalent BCP melts. Polymers were coarse-grained into discrete worm-like chains and non-bonded interactions were introduced through a quadratic, generic, functional of instantaneous local densities of monomers of different chemical

species. The functional accounts for limited compressibility and repulsion between unlike monomers. The strength of the repulsion is controlled by a bare<sup>120</sup> Flory-Huggins-like parameter,  $\chi$ . We transformed the functional-based definition of interactions into particle-based potentials via a simple PM scheme<sup>126,194,225,226</sup> and sampled the configurational space with local MC moves, that realize Rouse-like pseudo-dynamics. The model was parameterized to mimic characteristic conformational and volumetric properties of PPV and polyacrylates – two typical families of semiconducting and insulating polymers relevant to PLED applications.

The hybrid approach enabled the simulation of samples with dimensions on the order of 100 nm, which is the typical thickness of active layers in an actual PLED, for a broad range of  $\chi$ -values. We found that for the Rouse-like pseudo-dynamics used in our simulations, the disordered phase is stable or metastable for  $0 \leq \chi < \chi_s$ . The upper boundary  $\chi_s$  is the MF spinodal obtained from standard RPA theory, which we adapted to the specific features of our model: worm-like chain architecture and compressibility (see section 2.2). We analyzed the structure of the disordered morphologies on local and more global scales, focusing on the spatial distribution of the electrically active PPV component.

Structural analysis demonstrated the local heterogeneity of disordered morphologies due to thermal fluctuations in composition, as well as segregation of PPV and polyacrylate monomers. We found that the local segregation near the MF spinodal is stronger in BCPs than in the equivalent blends. This qualitative difference between blends and BCP is stronger for higher compositional asymmetries, i.e. higher fractions of insulating homopolymers or blocks in the mixture. Our BCP did not show a clear tendency to form spherical domains at high  $\chi$  because the surplus of acrylate was not sufficiently high. Therefore, we cannot conclude whether the observed difference between BCP and blends persists for very asymmetric compositions. In this case, BCPs can micellize in the disordered phase.<sup>168,181,227,228</sup>

Our observations on the heterogeneity of disordered morphologies highlight the phenomenological character of effective medium charge-transport models<sup>165</sup> based on the MH formalism.<sup>166</sup> These models only yield effective transport and trap site densities when fitted against experimental current-voltage data. However, global averaging of composition in combination with a one-dimensional drift-diffusion model is insufficient to explain how

a reduction in trapping depends on local morphological details of the active layer of the PLED. The present mesoscopic description of morphologies could be combined with an advanced model for charge-carrier dynamics<sup>219,229–231</sup> to provide for a more appropriate description of the effect of composition heterogeneity on trap elimination. Such a model is necessary because a non-homogeneous composition automatically leads to spatial inhomogeneities in charge distribution, local electric field, and hence carrier mobility.

Instead of employing sophisticated models of charge-transport, we used a simplified percolation analysis to qualitatively link the global distribution of the PPV component with macroscopic electric conductance. Strikingly, we found that the  $\chi$  – equivalently the temperature – at which the disordered morphology is annealed prior to solidification, has a stronger influence on electrical percolation in BCPs than in their equivalent blends. Specifically, if there is no flow of current through a disordered BCP morphology prepared by annealing at low  $\chi$  (high temperatures) it might be still possible to recover conductivity by preparing the morphology at higher  $\chi$  (lower temperatures) which are near (but do not cross) the ODT. For an equivalent blend, it is less likely that one can switch between conducting and nonconducting morphologies simply by changing the  $\chi$  (temperature) of annealing. Similar to local segregation, the differences between blends and BCPs with respect to their electrical percolation increase as the compositional asymmetry of the mixture becomes larger. The percolation analysis also suggests an unexpected consequence of finite size effects related to the limited thickness of active layers. Because finite size effects smoothen the percolation transition, the macroscopic current conductance of layers annealed under conditions, e.g. temperatures, close to this transition may be erratic.

Here we considered isotropic systems and neglected the confined film geometry of actual PLED layers. Even in disordered polymer blends and BCPs confinement profoundly affects microstructure: the boundaries of the film modify polymer conformations and are usually enriched in one component. Of course, conjecturing local environment and percolation properties in these anisotropic regions from “bulk-like” systems is not valid. However, we believe that our analysis can provide useful insights into structural differences between blends and BCPs in the interior of PLED layers, i.e. their bulk-like

part. The part of the layer that can be considered as bulk is largely determined by the decay of compositional perturbations into the film, characterized<sup>232–234</sup> by a correlation length  $\zeta$ . The quantity  $\zeta$  relates directly<sup>232–234</sup> to the correlation length of bulk composition fluctuations and is, therefore, proportional to the size of the chains quantified, e.g. by the average end-to-end distance,  $R_e$ . The prefactor in this proportionality depends on the incompatibility of unlike monomers – for symmetric systems, within MF<sup>232,235</sup>,  $\zeta$  diverges as one approaches<sup>232,233,235</sup> the phase transition. For strongly asymmetric systems (the focus of our work) simulations<sup>233</sup> suggest that the changes of  $\zeta$  as a function of incompatibility are less pronounced. For conjugated polymers similar to those considered in our study, the typical thickness of PLED layers is equivalent to several  $R_e$ . Therefore, for thermodynamic conditions away from the phase transition we expect these layers to have an extended bulk-like region. At higher  $\chi$  the isotropic approximation for the interior of the layers deteriorates for symmetric systems (because of the significant increase of  $\zeta$ ) but might be still reasonably accurate for the application-relevant case of asymmetric blends and BCPs.

The model described in this study can be extended<sup>126,194,196</sup> to include free polymer surfaces and polymer/solid interfaces. This extension will allow for a more realistic mesoscopic description of PLED layers at comparable costs of computation. However, we emphasize that explicit considerations of film geometry will significantly expand the parameter space. Indeed interfacial phenomena, e.g. surface segregation and conformational changes, are driven by a complex balance<sup>197</sup> between various entropic and enthalpic factors, which change across different systems. Therefore, the choice of the relevant parameters of the model, e.g. the strength of effective interactions with film boundaries, becomes much more materials specific. Inevitably, the scenarios that can be considered at each simulation study are rather limited.

Our modeling results suggest that, from a fundamental point of view, it is of interest to study the electronic behavior of blend- or BCP-based devices of which the active layer has been processed in the disordered phase near the phase transition. To our knowledge such studies are currently lacking. Structure-conductivity relationships on both sides of the phase transition have been explored experimentally for other polymer-based systems, such as ion-conducting mixtures.<sup>236</sup>

In relation to our current findings, we note that the non-trivial structure of

disordered BCP morphologies, especially close to ODT, makes them potentially interesting for other devices. For instance, the motivation of using donor(D)-acceptor(A) BCPs,<sup>237,238</sup> or BCP compatibilizers<sup>239</sup> in OPV has focused on ordered phases, following the philosophy of obtaining thermodynamically relaxed microstructures that provide for stable domains with dimensions commensurate with the exciton diffusion length.<sup>237,238</sup> However, despite exhibiting enhanced thermal stability compared to classical blends, such BCP-based OPV cells have never outperformed blend-based devices. With this respect, so far, possible advantages of stabilized *disordered* D-A BCP morphologies near the ODT have not been explored.

## Chapter 4

# When can soft models describe polymer knots?

We are currently preparing a publication<sup>240</sup> on the basis of this chapter. The main figures in the publication will be same as the figures shown in this chapter. Parts of the text in the publication is going to be similar to the corresponding content in this chapter.

### 4.1 Introduction

The soft potentials of mesoscopic models usually lead to simplified local liquid structure. This approximation does not affect the mesoscopic description of those properties that show scale separation. Such properties are governed on large scales by universal laws<sup>19</sup>, encapsulating effects of microscopic details – including local liquid packing – into numerical prefactors of generic expressions. However, for many properties the concept of scale separation does not apply. Our work in this chapter is concerned with one of such cases: the behavior of polymer self-entanglements or “knots”.

Already for single (isolated) chains, simulations have shown that microscopic features largely affect knotting behavior<sup>241,242</sup>. While short flexible ideal chains tend to form numerous<sup>243</sup> highly localized knots, adding excluded volume interactions between monomers can significantly increase the chain lengths at which knots are frequently formed<sup>244</sup>. These knots are still (weakly) localized, but considerably larger than in the ideal case. Globular polymers and confined polymers, in contrast, are heavily knotted, but their

knots tend to be loose and delocalized<sup>244</sup>, and thus become a global property of the chain.

For many chain systems, modeling studies of knotting behavior are sparse. For the special case of polymer melts one can naively try to apply basic polymer physics. According to the Flory hypothesis<sup>48,245</sup>, the effects from excluded volume interactions in melts are screened on scales exceeding the microscopic Edwards correlation length. Therefore, the conformations of polymers follow the statistics of ideal chains that have the same contour length and mean-squared end-to-end distance as the chains in the melt. Recent studies<sup>246,247</sup> have demonstrated that the Flory hypothesis is an approximation, which, nevertheless, becomes highly accurate for long chains. Therefore, one might expect that the properties of knots in melts of long chains and their equivalent ideal chains are similar.

Intriguingly, recent modeling studies<sup>47</sup> have demonstrated that this assumption is too simplistic. In polymer melts, knots appear significantly less frequently and are more loose, comparing to their equivalent isolated ideal chains. Apparently, even local excluded volume effects, or, more generally, microscopic liquid structure can significantly influence the behavior of polymer knots. These observations lead to a basic question: Can mesoscopic models describe knots in polymer melts, given the absence of hard excluded volume and simplified local liquid structure?

Here, we address this fundamental question using a model that is typical for mesoscopic simulations of polymeric materials. The molecular architecture of long polymers is described through the WLC model (see section 2.2). The DFT-based potential (see section 2.2) is employed to describe the non-bonded interactions between CG monomers. By using a PM scheme (see section 2.3) to perform particle-based simulations, we deliberately want to obtain polymer liquids with very crude local liquid structure. The mesoscopic model is parameterized to accurately reproduce mesoscopic structure and conformations of microscopic polymer melts that have been equilibrated in a previous study<sup>47</sup> using a bead-spring model. We directly compare the knotting properties in mesoscopic melts with their counterparts in the equivalent microscopically-resolved samples.

We find that the ability of mesoscopic models to accurately describe knotting properties is crucially affected by the relationship between two length



scales: the size of the excluded volume and the length scale characterizing the stiffness of polymer chains. We qualitatively explain the trends of knotting behavior in mesoscopic and microscopic simulations benefiting from a free-energy model of simple knots available in the literature.<sup>241,248</sup>

## 4.2 Qualitative insights from a free energy model

To qualitatively understand the effect of local liquid structure on knots, we focus on knots with the simplest possible topology: the trefoil knots (see Fig. 4.1). According to the Grosberg-Rabin theory for ideal chains<sup>248</sup>, the free energy cost – with respect to the unknotted state – to form a trefoil knot includes two contributions, the bending energy and the loss of entropy due to confinement. Dai et al.<sup>241</sup> adapted the above theory to chains with finite thickness  $w$  and derived the free energy cost for forming a trefoil knot with contour length  $N_{\text{knot}}$ . The thickness of chains is determined by the size of excluded volume and sets the characteristic length-scale of local liquid structure.

We rewrite the expression derived by Dai et al. in terms of the normalized contour length of knots  $\tilde{N}_{\text{knot}}$  and thickness  $\tilde{w}$  as follows,

$$\beta F_{\text{knot}} = \frac{k_1}{2} \frac{1}{\tilde{N}_{\text{knot}}} + k_2 \sqrt[3]{2} \frac{\tilde{N}_{\text{knot}}^{1/3}}{\left(1 - \frac{p\tilde{w}}{\tilde{N}_{\text{knot}}}\right)^{2/3}} \quad (4.1)$$

The first term and second term in eq. 4.1 corresponds to the bending energy and the loss of entropy due to confinement, respectively.  $k_1, k_2$  are positive coefficients. The normalized contour length of knot and chain thickness are defined as  $\tilde{N}_{\text{knot}} = N_{\text{knot}}/l_k$  and  $\tilde{w} = w/l_k$ , where  $l_k$  is the length of the Kuhn segment of chains. The prefactors  $1/2$  and  $\sqrt[3]{2}$  make eq. 4.1 equivalent to the original expression<sup>241</sup>, casted in terms of  $N_{\text{knot}}/l_p$ . Here  $l_p$  is the persistence length and we assume  $l_k \simeq 2l_p$ .  $p$ <sup>248</sup> is related to the topology of knots and is defined as the ratio between the contour length of the knot  $N_{\text{knot}}$  and the diameter  $D$  of a maximally inflated virtual tube confining the knots (see Fig. 4.1). For trefoil knots,  $p$  is approximately equal to 12<sup>249</sup>.

From the definition of  $p$  we know that the minimum knot that a chain can form has the contour length  $p\tilde{w}$ . Therefore, the term  $\left(1 - \frac{p\tilde{w}}{\tilde{N}_{\text{knot}}}\right) \geq 0$  and

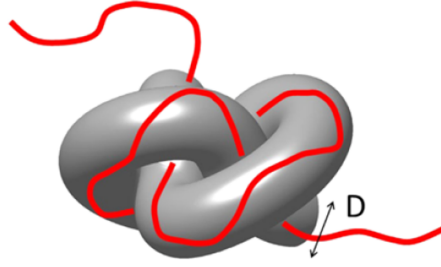


FIGURE 4.1: Illustration of a trefoil knot formed in an open chain (red). The knot is confined in a virtual tube (gray) with diameter  $D$ . The figure is taken from ref. [241].

the loss of entropy due to confinement is always positive. It should be emphasized that the entropy loss can be expressed by the second term in eq. 4.1 only if the trefoil knots are tight enough so that we can consider the knots are strongly confined in virtual tubes<sup>249</sup>.

The free energy cost  $\beta F_{\text{knot}}$  returns to the simple expression within Grosberg-Rabin theory when  $\tilde{w} = 0$ , i.e.,

$$\beta F_{\text{knot,id}} = \frac{k_1}{2} \frac{1}{\tilde{N}_{\text{knot}}} + k_2 \sqrt[3]{2} \tilde{N}_{\text{knot}}^{1/3} \quad (4.2)$$

It can be easily seen from eq. 4.2 that the bending energy and the loss of entropy due to confinement monotonically decreases and increases, respectively, with the increasing of  $\tilde{N}_{\text{knot}}$ . Therefore, the bending energy and the loss of entropy tends to swell and shrink, respectively, the knot sizes. However, the loss of entropy for real chains with non-zero  $\tilde{w}$ , which is defined by the second term in eq. 4.1, does not monotonically increase with  $\tilde{N}_{\text{knot}}$ , but has a minimum at  $\tilde{N}_{\text{knot}} = 3p\tilde{w}$ . Therefore it tends to swell very small knots with size smaller than  $3p\tilde{w}$ , but shrink knots with size larger than  $3p\tilde{w}$ . For both ideal and real chains, the competition between the bending energy and the loss of entropy due to confinement leads to a local minimum of  $F_{\text{knot,id}}$  or  $F_{\text{knot}}$ , corresponding to a metastable and most probable trefoil knot with size  $\tilde{N}_{\text{knot}}^*$ .

By comparing eqs. 4.1 and 4.2, we observe that the free energy cost of real chains  $\beta F_{\text{knot}}$  can be approximated by  $\beta F_{\text{knot,id}}$  when chains are sufficiently stiff making  $\tilde{w} = w/l_k \approx 0$ . This indicates that the behavior of trefoil knots formed in melts containing stiff chains approaches the universal limit of ideal chains and the impact of  $\tilde{w}$  can be ignored. To be more general, this means

that local liquid structure of polymer melts does not have significant influence on the behavior of trefoil knots when the chains are stiff enough. The same tendency can be expected for more complex knot types. Accordingly, we can predict from the simple free-energy model that, mesoscopic models can describe relatively small knots in polymer melts quite well when chains are sufficiently stiff.

If the chain thickness  $\tilde{w}$  cannot be ignored, the free energy cost  $\beta F_{\text{knot}}$  for forming a trefoil knot with contour length  $\tilde{N}_{\text{knot}}$  in a real chain with stiffness  $l_k$  increases with the increasing of  $\tilde{w}$ . This is because the loss of entropy due to confinement always increases as  $\tilde{w}$  becomes larger, and the bending energy is not affected by  $\tilde{w}$ . Assuming that the monotonic increase of  $\beta F_{\text{knot}}$  with respect to  $\tilde{w}$  also holds for more complex knots, the simple free-energy model suggests that the probability of a randomly picked chain being in knotted state decreases as  $\tilde{w}$  increases.

Moreover, larger  $\tilde{w}$  increases the size of the most probable trefoil knot  $\tilde{N}_{\text{knot}}^*$ . This can be seen by analyzing the derivative of  $\beta F_{\text{knot}}$  with respect to  $\tilde{N}_{\text{knot}}$ .  $\tilde{N}_{\text{knot}}^*$  corresponds to the value of  $\tilde{N}_{\text{knot}}$  at the local minimum of  $\beta F_{\text{knot}}$ . Then one can write,

$$\beta F'_{\text{knot}}|_{\tilde{N}_{\text{knot}}^*} = 0 \quad (4.3)$$

where

$$\begin{aligned} \beta F'_{\text{knot}} &= -\frac{k_1}{2\tilde{N}_{\text{knot}}^2} + \frac{\sqrt[3]{2}k_2}{3(\tilde{N}_{\text{knot}} - p\tilde{w})^{2/3}} - \frac{2\sqrt[3]{2}k_2p\tilde{w}}{3(\tilde{N}_{\text{knot}} - p\tilde{w})^{5/3}} \\ &= -\frac{k_1}{2\tilde{N}_{\text{knot}}^2} + \frac{\sqrt[3]{2}k_2}{3\tilde{N}_{\text{knot}}^{2/3}} \cdot \underbrace{\left( \frac{1}{\left(1 - \frac{p\tilde{w}}{\tilde{N}_{\text{knot}}}\right)^{2/3}} - \frac{2p\tilde{w}}{\tilde{N}_{\text{knot}}\left(1 - \frac{p\tilde{w}}{\tilde{N}_{\text{knot}}}\right)^{5/3}} \right)}_{K(\tilde{w}, \tilde{N}_{\text{knot}})} \end{aligned} \quad (4.4)$$

We define the part of second term within the bracket in eq. 4.4 as a function  $K(\tilde{w}, \tilde{N}_{\text{knot}})$ . Before we discuss how chain thickness  $\tilde{w}$  influences the local minimum of eq. 4.4, it is important to know several properties of  $K(\tilde{w}, \tilde{N}_{\text{knot}})$ . First,  $K(0, \tilde{N}_{\text{knot}}) = 1$ , making eq. 4.4 correspond to the derivative of  $\beta F_{\text{knot}, \text{id}}$ ,

$$\beta F'_{\text{knot}, \text{id}} = -\frac{k_1}{2\tilde{N}_{\text{knot}}^2} + \frac{\sqrt[3]{2}k_2}{3\tilde{N}_{\text{knot}}^{2/3}} \quad (4.5)$$

Second,  $\partial K(\tilde{w}, \tilde{N}_{\text{knot}})/\partial \tilde{N}_{\text{knot}} > 0$  when  $\tilde{w} > 0$ . This means  $K(\tilde{w}, \tilde{N}_{\text{knot}})$  and

also the entire derivative  $\beta F'_{\text{knot}}$  monotonically increase with the increasing of  $\tilde{N}_{\text{knot}}$ . Considering  $K(\tilde{w}, \tilde{N}_{\text{knot}}) \rightarrow 1$  as  $\tilde{N}_{\text{knot}} \rightarrow \infty$ , we can conclude that the relationship  $K(\tilde{w}, \tilde{N}_{\text{knot}}) < 1$  always holds.

Then we can demonstrate that larger  $\tilde{w}$  shift the local minimum of eq. 4.4 to larger values, by comparing the  $\tilde{N}_{\text{knot}}^*$  of an extreme case, ideal chains with  $\tilde{w} = 0$ , with that of real polymer chains. Suppose the size of the most probable trefoil knot formed in ideal chains with stiffness  $l_k$  is  $\tilde{N}_{\text{knot,id}}^*$ . According to eq. 4.5 we can write,

$$\frac{\sqrt[3]{2}k_2}{3\tilde{N}_{\text{knot,id}}^{*2/3}} = \frac{k_1}{2\tilde{N}_{\text{knot,id}}^{*2}} \quad (4.6)$$

For real chains with the same stiffness, we assume the coefficients  $k_1, k_2$  are same as that of ideal chains. Note that this assumption is a simplification serving for qualitatively predicting the influence of  $\tilde{w}$  on  $\tilde{N}_{\text{knot}}^*$ . In reality,  $k_1, k_2$  can vary between different models. Then the derivative of free energy cost of real chains  $\beta F'_{\text{knot}}$  at the size  $\tilde{N}_{\text{knot,id}}^*$  is,

$$\beta F'_{\text{knot}}|_{\tilde{N}_{\text{knot,id}}^*} = -\frac{k_1}{2\tilde{N}_{\text{knot,id}}^{*2}} + \frac{\sqrt[3]{2}k_2}{3\tilde{N}_{\text{knot,id}}^{*2/3}}K(\tilde{w}, \tilde{N}_{\text{knot,id}}^*) \quad (4.7)$$

By substituting eq. 4.6 into  $\beta F'_{\text{knot}}|_{\tilde{N}_{\text{knot,id}}^*}$ , we obtain,

$$\beta F'_{\text{knot}}|_{\tilde{N}_{\text{knot,id}}^*} = \frac{k_1}{2\tilde{N}_{\text{knot,id}}^{*2}} [K(\tilde{w}, \tilde{N}_{\text{knot,id}}^*) - 1] < 0 \quad (4.8)$$

Taking into account that the derivative  $\beta F'_{\text{knot}}$  exhibits monotonic increase with  $\tilde{N}_{\text{knot}}$ , the size of the most probable knot of real chains corresponding to  $\beta F'_{\text{knot}} = 0$  should be larger than that of ideal chains  $\tilde{N}_{\text{knot,id}}^*$ . Therefore, for chains having larger  $\tilde{w}$ , the most probable trefoil knots formed in these chains have larger sizes.

It should be noted that all the predictions obtained from free-energy model work only for (trefoil) knots with relatively small sizes. For larger (trefoil) knots, the free-energy model becomes invalid<sup>241,248</sup>. In the following sections, a detailed simulation study quantifying the effects of local liquid structure on behavior of both small and large knots formed in melts will be discussed. The qualitative predictions obtained from the simple free-energy model will be verified based on the simulation results of small knots.

## 4.3 Model description

### 4.3.1 The reference bead-spring model

The reference data of microscopic polymer melts are taken from ref [47]. Meyer, Horwath, and Virnau generated microscopic melts based on a bead-spring model by using standard molecular dynamics simulations. In the following paragraphs, we summarize the main elements of the bead-spring model, which are of importance for the following discussions. The detailed description can be found in the ref. [47].

The microscopic melts contain  $n_{\text{mic}}$  identical chains in the volume  $V_{\text{mic}}$ . Each chain is formed by  $N_{\text{mic}}$  hard beads with excluded volume. The repulsion between these hard beads is described by the classic Lennard-Jones (LJ) potential,

$$V_{\text{LJ}}(r) = 4\tilde{\epsilon} \left[ (\sigma/r)^{12} - (\sigma/r)^6 \right] \quad (4.9)$$

where  $\sigma = 1$  and  $\tilde{\epsilon} = 1$ . The LJ potential is shifted at the cutoff distance  $r_c = \sqrt[6]{2}\sigma$ . The bonds between beads are described by harmonic springs, and the bonded potential is defined as:

$$V_{\text{b}}(r_{i,i+1}) = k(r_{i,i+1} - b_0)^2 \quad (4.10)$$

where  $k = 400$  and  $b_0 = 0.967\sigma$ .  $r_{i,i+1}$  is the distance between two bonded beads with indices  $i$  and  $i + 1$ . The parameters in the bonded potential in practice lead to rigid bonds with lengths fixed to  $b_0$ . In addition to eq. 4.10, an angular potential is added to control the stiffness of chains,

$$V_{\text{a}}(\theta) = B(1 - \cos \theta) \quad (4.11)$$

here  $\theta$  is the angle between two connected bonds. Setting  $B = 0$  results in fully flexible chains, whereas larger  $B$  lead to stiffer chains.

As listed in the table 4.1, different microscopic melts containing chains with different stiffness parameters  $B$  are simulated based on this model, i.e.,  $B = 0, 2, 4$ . For each  $B$ , several chain lengths are considered:  $N_{\text{mic}} = 128, 256, 512$  and 1024. The average bead densities of these systems are same and set to be

TABLE 4.1: The contour length  $L$ , mean-squared end-to-end distance  $\langle R_e^2 \rangle$  and invariant degree of polymerization  $\sqrt{\bar{N}}$  of the reference microscopic melts with different  $B$  parameters and  $N_{\text{mic}}$ . The units of  $L$  and  $\langle R_e^2 \rangle$  are  $\sigma$  and  $\sigma^2$ , respectively.

Systems	$B$	$N_{\text{mic}}$	$L$	$\langle R_e^2 \rangle$	$\sqrt{\bar{N}}$
B0a	0	128	122.8	249.4	20.9
B0b		256	246.6	500.7	29.8
B0c		512	494.1	1003.4	42.2
B0d		1024	989.2	2008.9	59.8
B2a	2	128	122.8	427.5	47.0
B2b		256	246.6	858.4	66.8
B2c		512	494.1	1720.2	94.8
B2d		1024	989.2	3443.7	134.2
B4a	4	128	122.8	831.3	127.3
B4b		256	246.6	1669.1	181.1
B4c		512	494.1	3344.8	256.9
B4d		1024	989.2	6696.2	363.9

$\rho_{\text{mic}} = 0.68 \sigma^{-3}$ . In table 4.1, we also summarize the properties of these microscopic melts, including contour length  $L$ , mean-squared end-to-end distance  $\langle R_e^2 \rangle$  and invariant degree of polymerization  $\sqrt{\bar{N}}$ . All lengths are expressed in units of  $\sigma$ .  $\sqrt{\bar{N}}$  is an important property of polymer melts and will be discussed in detail in the next section. All the microscopic melts are labeled with short names, listed in the first column of table 4.1.

### 4.3.2 Mesoscopic model

#### Mapping strategy

The microscopic melts are mapped onto equivalent mesoscopic melts, which contain  $n_{\text{cg}}$  identical chains in volume  $V_{\text{cg}}$  and each chain is formed by  $N_{\text{cg}}$  soft beads. The mapping procedure conserves the chain density and key conformational properties. The same chain density implies the relationship,

$$\frac{n_{\text{mic}}}{V_{\text{mic}}} = \frac{n_{\text{cg}}}{V_{\text{cg}}} \quad (4.12)$$

To reproduce the key conformational properties, we recall that within the Flory hypothesis<sup>48,245</sup> the average behavior of long flexible chains in polymer melts can be described by equivalent Kuhn chains. Each Kuhn chain comprises freely-jointed  $N_k$  Kuhn segments, with length  $l_k$  each. The Kuhn segments are the smallest units along polymer chains that can be considered as uncorrelated. Therefore,  $l_k$  is a measure of chain stiffness and sets the scale at which the formation of knots becomes unlikely. Accordingly, one of the requirements for mesoscopically- and microscopically-resolved melts to have the same knotting properties is that mapping them on the same Kuhn chains, i.e. they have the same  $l_k$  and  $N_k$ . We emphasize that this requirement is only a necessary but not sufficient<sup>47</sup> condition. Clarifying additional conditions for having the same behaviour of knots is among the objectives of our study.

The parameters of a Kuhn chain,  $l_k$  and  $N_k$ , are expressed<sup>113</sup> through the contour length  $L$  and mean-squared end-to-end distance  $\langle R_e^2 \rangle$ , i.e.,

$$l_k = \langle R_e^2 \rangle / L \quad (4.13)$$

$$N_k = L / l_k = L^2 / \langle R_e^2 \rangle \quad (4.14)$$

$L$  and  $\langle R_e^2 \rangle$  are properties that can be easily sampled from simulations and their values of microscopic chains are given in the table 4.1. In our mesoscopic simulations, the same  $l_k$  and  $N_k$  are achieved by conserving the  $L$  and  $\langle R_e^2 \rangle$  of microscopic melts as invariant quantities.

We employ WLC model to quantitatively reproduce  $L$  and  $\langle R_e^2 \rangle$ . To fully define the three parameters of WLCs, i.e.,  $N_{cg}$ ,  $b_{cg}$  and  $\epsilon$ , three constraint functions are needed. The invariant quantities  $L$  and  $\langle R_e^2 \rangle$  already provide two constraints:  $L = f(N_{cg}, b_{cg})$  (see eq. 2.15) and  $\langle R_e^2 \rangle = h(N_{cg}, b_{cg}, \epsilon)$  (see eq. 2.14). Apart from that, it is necessary to consider several restrictions on  $N_{cg}$ . First of all, the discretization of WLCs should be finer than or at least comparable to the Kuhn chain, meaning  $N_{cg} \geq N_k$ . Though finer discretizations lead to larger CG systems and longer relaxation times. As a compromise, we set the third constraint on  $N_{cg}$  as  $N_{cg} = 2N_k$ . Then we can find the  $b_{cg}$  and  $\epsilon$  from the relationship  $L = f(N_{cg}, b_{cg})$  and  $\langle R_e^2 \rangle = h(N_{cg}, b_{cg}, \epsilon)$ , respectively. It is worth recalling that in a melt of interacting WLCs, the predicted  $\epsilon$  should be further tuned to quantitatively reproduce the  $\langle R_e^2 \rangle$ .

Our mapping strategy also conserves another important property of homopolymer melts, the invariant degree of polymerization  $\bar{N}$ . The invariant degree of polymerization  $\bar{N}$  for coil-like chains is defined<sup>21</sup> as,

$$\sqrt{\bar{N}} = \bar{\rho}_c R_e^3 \quad (4.15)$$

where  $\bar{\rho}_c$  is the average number density of chains in the homopolymer melts.  $R_e^3$  is proportional to the average volume of coil chains. Physically,  $\sqrt{\bar{N}}$  quantifies the number of chains interdigitating with a given chain. Therefore, it plays a central role for determining the deviation of chain conformations from the ideal random walk statistics. The chain conformations in polymer melts can be described by the simple ideal random walks when  $\sqrt{\bar{N}} \rightarrow \infty$  (Flory hypothesis<sup>48,245</sup>). The deviation increases as  $\sqrt{\bar{N}}$  becomes smaller<sup>250,251</sup>. Moreover, many mesoscale conformational and structural properties of polymeric systems are universal functions of  $\bar{N}$ <sup>250,252,253</sup>. For example, the depth of the correlation hole for entire chains in polymer melts scales as  $\sim \sqrt{\bar{N}}$ . Hence it is essential to preserve  $\bar{N}$  as an invariant quantity when one maps the homopolymer melts. Our mapping strategy assumes the same chain density and mean-squared end-to-end distance between mesoscopic and microscopic melts, thus we naturally conserve the  $\bar{N}$ .

### Non-bonded potential

The most simple DFT-based potential considering only mutual repulsion between CG beads is employed to describe non-bonded interactions in mesoscopic melts. The volume taken by the melts is discretized through a cubic lattice. Then we perform particle-based simulations based on the PM scheme with zeroth-order assignment function. The DFT-based potential  $H_{nb}$  has been introduced in eq. 2.23. Because only a single component is involved in homopolymer melts, the incompatibility parameter  $\chi$  is set to be zero, and we omit the subscript  $\alpha$  indicating components in eq. 2.23. For a better understanding of the following discussion, we recapitulate the simple form of



$H_{\text{nb}}$  for homopolymers,

$$\beta H_{\text{nb}} = \frac{1}{2} \frac{\kappa}{\rho_0 \Delta L^3} \sum_{i=1}^{n_{\text{cg}}} \sum_{s=1}^{N_{\text{cg}}} \sum_{j=1}^{n_{\text{cg}}} \sum_{t=1}^{N_{\text{cg}}} U(\mathbf{r}_i(s), \mathbf{r}_j(t))$$

(4.16)

with

$$U(\mathbf{r}_i(s), \mathbf{r}_j(t)) = \sum_{m=1}^{N_{\text{cell}}} \Pi[\mathbf{r}_i(s), \mathbf{c}_m] \Pi[\mathbf{r}_j(t), \mathbf{c}_m]$$

The parameters  $\Delta L$  and  $\kappa$  are chosen based on the objectives of this study. We know that  $\Delta L$  relates to the average number of overlapping particles  $\eta$  (see section 2.3). To understand correlations between knotting properties and local liquid structure in mesoscopic models, we must be able to model melts with  $\eta$  corresponding to the regime of weak ( $\eta < 1$ ) and strong ( $\eta > 1$ ) overlapping. Therefore  $\Delta L$  is an adjustable parameter in our model. Obviously,  $\Delta L$  can only be varied within the range  $(0, l_k)$ . This constraint ensures that  $\Delta L$  is not significantly larger than the smallest length-scales that characterize the physical phenomena, which is the  $l_k$  in this study. The parameter  $\kappa$  is varied to realize different repulsion strength  $\nu_k = \kappa / \rho_0 \Delta L^3$  (see section 2.3), which also determines the softness of potential. The ratio  $\nu_k$  varies from a fraction of  $k_B T$  to a few tens of  $k_B T$ .

### Simulation details

We perform simulations in the canonical ensemble. The melts are placed in cubic simulation boxes and PBC is applied to all dimensions. The lengths of boxes are set to be  $\sim 2\sqrt{\langle R_e^2 \rangle}$ . This choice is widely accepted as the minimum requirement for avoiding finite-system size effects in the disordered melts<sup>95</sup>. Both crankshaft and reptation moves are employed to accelerate the relaxation of dense melts.

## 4.4 Knot detection

The analysis of knotting properties is carried out in collaboration with Dr. Peter Virnau and a program developed by Dr. Peter Virnau is employed for

knot detection. In this section, we will provide basic knowledge on the detection method used in this study, a variant of Alexander polynomial. Essentially, our presentation recapitulates the presentation of the method provided in several topical reviews and books<sup>254–256</sup>. A complete discussion on the definition of Alexander polynomial can be found in the relevant books<sup>255,257</sup>.

Normally knots are only well-defined in closed loops. Different knot types are distinguished according to the minimum number of crossings (crossing number) in a projection of the chain onto a plane. Several basic knot types are shown in Fig. 4.2, including unknot (0), trefoil knot ( $3_1$ ), and figure-eight knot ( $4_1$ ), which has 0, 3, or 4 crossings, respectively. The subscripts distinguish different knot types with the same number of crossings. Note that the number of knot types increases considerably with the number of crossings. For example, the number of knot types having 15 crossings is on the order of  $10^5$ <sup>258</sup>.

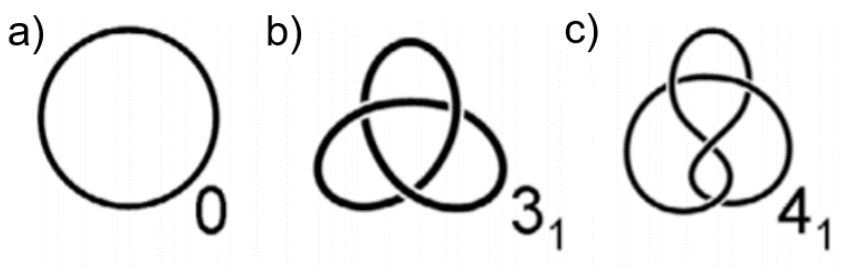


FIGURE 4.2: The structures of the most basic knot. a) unknotted loop (0), b) trefoil knot ( $3_1$ ), c) four-eight knot ( $4_1$ ). The figure is replotted from ref. [256].

In order to distinguish between different knots, one can define a knot invariant assigning a unique value to every knot type. However, considering the huge number of involved knot types when crossing number is large, up to now, no algorithm can distinguish between all the knot types<sup>47</sup>. Alexander polynomial  $\Delta$  is a popular invariant that distinguishes between simple knots and assigns a polynomial to each knot type. For the basic knots shown in Fig. 4.2, each of them has a unique polynomial among the knots having up to 10 crossings.

However, Alexander polynomial is only defined for closed loops. For linear open chains concerned in this study, one must first carefully connect the two ends. For both microscopic and mesoscopic chains involved in our study, a

closure that has been successfully used for macromolecules is chosen<sup>47,259</sup>. As shown in Fig. 4.3, one first determines the center of mass (COM) of the analyzed chain, and then obtains two lines defined by the COM and the two ends of the chain. These two lines are extended to the outside of the chain. By connecting two points along the line (one point each line), which are far from the chain, the open chain is closed.

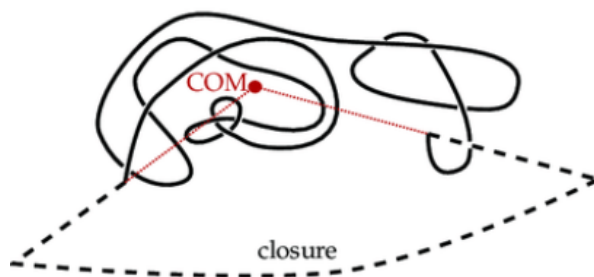


FIGURE 4.3: The mechanism of defining the closure for an open chain. Two lines are determined based on the center of mass (COM) and two ends of the chain. The open chain is closed by connecting two points which are far away from the chain. The figure is taken from ref. [259].

Then the closed chain is simplified into a chain containing fewer beads. In this way, the computational cost of the calculation of Alexander polynomials is significantly reduced. The bead reduction is performed<sup>47</sup> by grouping every three successive beads along the chain and considering the triangles formed by them. If the chain itself does not cross the triangle, the middle bead is deleted. Otherwise, all three beads remain. The above procedures are repeated for several times to ensure the simplest chain is obtained.

The Alexander polynomial  $\Delta$ <sup>260</sup> of a simplified closed polymer chain is determined based on the crossing number along the chain and the handedness of crossings<sup>47</sup>. The crossing number is counted according to a projection of the polymer chain, e.g., projection on the x-y plane. By choosing an arbitrary starting point and direction for walking along the chain projection, we can determine the handedness of each crossing. As shown in Fig. 4.4, there are three crossings in the projection (①, ②, ③). According to the chosen starting point (●) and direction (arrow)<sup>47</sup>, the crossings are numbered as 1, 2, and 3. From the starting point, we first underpass a later section of the projection at crossing 1, then overpass at crossing 2 and again underpass at crossing 3. Then we can divide the projection into several arcs (I, II, III), which are defined from underpass to underpass. Depending on the direction of two arcs

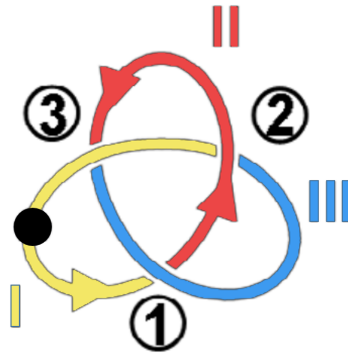


FIGURE 4.4: The numbering of crossing (1, 2, 3) and arcs (I, II, III) according to a chosen starting point (●) and direction (indicated by arrows). The figure is taken from ref. [47]

forming the crossing, the crossing is either right-handed or left-handed (as shown in Fig. 4.5). Specifically, we assume that the projection is on x-y plane, and if the cross product of the vectors defined by two arcs forming the crossing is positive, the crossing is right-handed. The crossing is left-handed if the cross product is negative. Accordingly, we can find that all the crossings in Fig. 4.4 are right-handed. The detailed rules for defining  $\Delta$  based on crossing numbers and handedness are too technical and beyond the scope of this thesis. Hence we do not elaborate upon this point and refer the interested reader to the reviews and books that have been mentioned earlier.

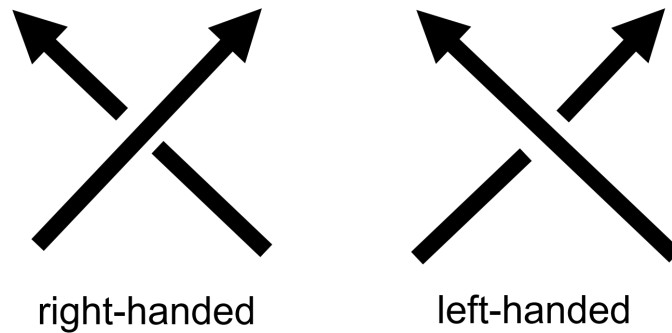


FIGURE 4.5: Definition of handedness of a crossing. The figure is replotted from ref. [256].

Based on the presented detection method, we quantify the knotting behavior of microscopic or mesoscopic melts through knotting probability  $P_k$  and sizes of trefoil knots. Specifically, we generate sufficient number of melt configurations which are decorrelated. Suppose the total number of chains within

these configurations is  $n$ . We identify the chains in knotted state and count the number of knotted chains  $n_{\text{knot}}$ . The knotting probability  $P_k$  is defined as  $P_k = n_{\text{knot}}/n$ . For every chain forming a trefoil knot, the size of trefoil knot is determined by successively deleting beads from one side, then from the other side until the Alexander polynomial changes<sup>47</sup>.

## 4.5 Structural and conformational properties

Before we compare the knotting properties of mesoscopic and microscopic melts, we first characterize the basic structural and conformational properties of the melts generated through our mesoscopic model. First of all, the results of structural and conformational properties are required for quantifying the accuracy with which our model reproduces the mesoscopic features of the microscopic melts. Secondly, these results are important for interpreting the behavior of knots. Considering that knots involve multiple scales, we study in this section structural and conformational properties on both local and mesoscopic scales.

We first investigate the ability of mesoscopic model to describe structural and conformational properties of microscopic melts by focusing on the mesoscopic melts mapped from B2c microscopic melt. Different mesoscopic melts equivalent to B2c melt are generated by using different repulsion strength  $\nu_k$  and average number of overlapping particles  $\eta$  (see table 4.2).  $\nu_k$  is varied by tuning the non-bonded parameter  $\kappa$  at constant  $\bar{\rho}_0$  and  $\Delta L$ , and  $\eta$  is adjusted by changing the lattice size  $\Delta L$  at constant  $\bar{\rho}_0$ . According to the data provided in table 4.1, B2c microscopic melt has chain density  $\bar{\rho}_c = \bar{\rho}_0/N_{\text{mic}} = 0.0013 \sigma^{-3}$  and  $N_k = L^2/\langle R_e^2 \rangle = 142$  Kuhn segments per chain. Based on our mapping strategy, the mesoscopic melts have the same chain density  $\bar{\rho}_c = 0.0013 \sigma^{-3}$ . The bonded parameters  $N_{\text{cg}}$ ,  $b_{\text{cg}}$  and  $\epsilon$  of melts with different  $\nu_k$  and  $\eta$  are listed in table 4.2. In particular,  $N_{\text{cg}} = 2N_k = 284$  and  $b_{\text{cg}}$  is accordingly determined as  $1.75 \sigma$ .  $\epsilon$  is tuned to quantitatively match the  $\langle R_e^2 \rangle$  of the B2c melt (see section 2.2).

The local liquid structure of mesoscopic melts can be described by monomer-monomer radial distribution function  $g(r)$ . It measures the probability of

TABLE 4.2: The parameters of mesoscopic melts mapped from the B2c microsocopic melt.

$\nu_k$	$\eta$	$\bar{\rho}_0 (\sigma^{-3})$	$\kappa$	$\Delta L (\sigma)$	$N_{cg}$	$b_{cg} (\sigma)$	$\epsilon$
3	0.1	0.37	0.3	0.64	284	1.74	1.0
	0.2		0.6	0.82			0.99
	0.5		1.5	1.1			0.94
	1		3	1.37			0.94
	15		45	3.46			0.97
0.2	1	0.37	0.2	1.37	284	1.74	0.97
0.8			0.8				0.97
10			10				0.94
15			15				0.94
20			20				0.94

finding a bead at distance  $r$  away from a reference bead, and is defined as,

$$g(r) = \frac{1}{A} \left\langle \sum_i^{N_{tot}} \sum_{j \neq i}^{N_{tot}} \delta(r_{ij} - r) \right\rangle \quad (4.17)$$

where  $A = 4\pi r^2 \bar{\rho}_0 N_{tot}$  is a normalization constant.  $N_{tot}$  is the total number of beads in the system, and  $r_{ij}$  denotes the distance between beads  $i$  and  $j$ .

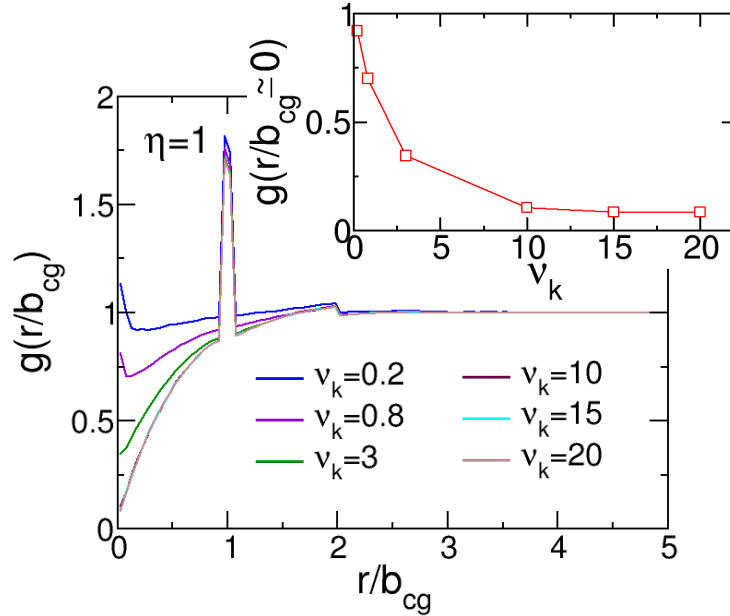


FIGURE 4.6: The radial distribution functions obtained from mesoscopic models mapped from B2c. The mesoscopic models have the same average number of overlapping particles  $\eta = 1$  and different repulsion strengths (see legends).

The  $g(r)$  of melts with different repulsion strengths  $\nu_k$  are shown in Fig. 4.6. In this figure, the distance  $r$  is scaled by the bond length of WLC  $b_{cg}$ , so that the main peak of  $g(r)$  originating from chain connectivity is always at  $r/b_{cg} = 1$ . We observe from Fig. 4.6 that,  $\nu_k$  mainly influences the structure on length scales smaller than 2 bonds, i.e.,  $r/b_{cg} < 2$ . In addition, the value of  $g(r)$  at  $r \approx 0$ , the so called depth of monomer-monomer correlation hole, decreases with the increasing of repulsion strength  $\nu_k$ , or equivalently decreasing of softness. This tendency indicates that stronger repulsion leads to fewer overlaps between beads. However,  $g(r \approx 0)$  saturates to  $\sim 0.08$  with respect to  $\nu_k$  and cannot reach zero as in microscopic melts with hard excluded volume. This means that we cannot completely eliminate overlaps between beads by increasing the repulsion strength.

The peculiar dependence of  $g(r \approx 0)$  on the repulsion strength  $\nu_k$  stems from the zeroth-order assignment function used in the PM scheme. According to the definition of zeroth-order assignment function (see section 2.3), beads do not interact with each other when they belong to different cells. Therefore, two beads in different but neighboring cells can be arbitrarily close to each other without any energy penalty. As shown in Fig. 4.7, when two beads are at the two sides of the common surface, edge or corner of neighboring cells, the distance between them can be arbitrary small. Strong repulsion cannot separate these closed packed non-interacting beads.

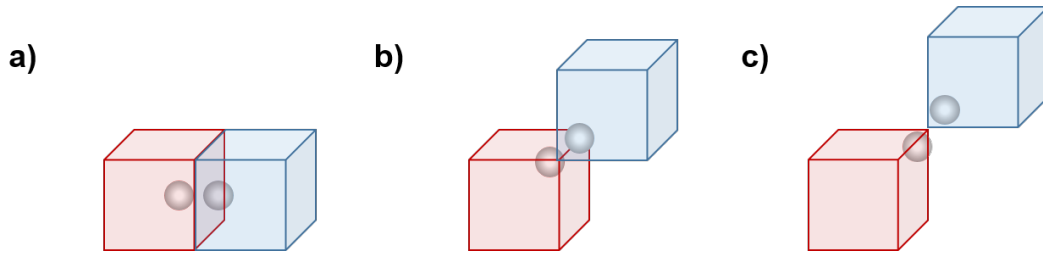


FIGURE 4.7: Illustration of close-packed pair of beads in two neighboring cells. Depending on the relative position of neighboring cells, they can share a common a) surface, b) edge or c) corner.

The above discussion about the saturation of  $g(r \approx 0)$  can be conveniently illustrated by decomposing  $g(r)$  into two types of contributions. We consider the contributions from pairs of beads in the same cell  $g_{sc}(r)$  and in different

cells  $g_{dc}(r)$ , which are defined as,

$$g_{sc}(r) = \frac{1}{A} \left\langle \sum_i^{N_{tot}} \sum_{j \neq i}^{N_{tot}} \delta(r_{ij} - r) \omega(\mathbf{r}_i, \mathbf{r}_j) \right\rangle \quad (4.18)$$

and:

$$g_{dc}(r) = \frac{1}{A} \left\langle \sum_i^{N_{tot}} \sum_{j \neq i}^{N_{tot}} \delta(r_{ij} - r) (1 - \omega(\mathbf{r}_i, \mathbf{r}_j)) \right\rangle \quad (4.19)$$

with

$$\omega(\mathbf{r}_i, \mathbf{r}_j) = \sum_{m=1}^{N_{cell}} \Pi[\mathbf{r}_i, \mathbf{c}_m] \Pi[\mathbf{r}_j, \mathbf{c}_m] \quad (4.20)$$

where  $\mathbf{r}_i, \mathbf{r}_j$  are the coordinates of beads  $i$  and  $j$ , respectively. Function  $\omega(\mathbf{r}_i, \mathbf{r}_j)$  identifies whether particles  $i$  and  $j$  are in the same cell.  $\omega(\mathbf{r}_i, \mathbf{r}_j) = 1$  if particles  $i$  and  $j$  belong to the same cell, and  $\omega(\mathbf{r}_i, \mathbf{r}_j) = 0$  otherwise.

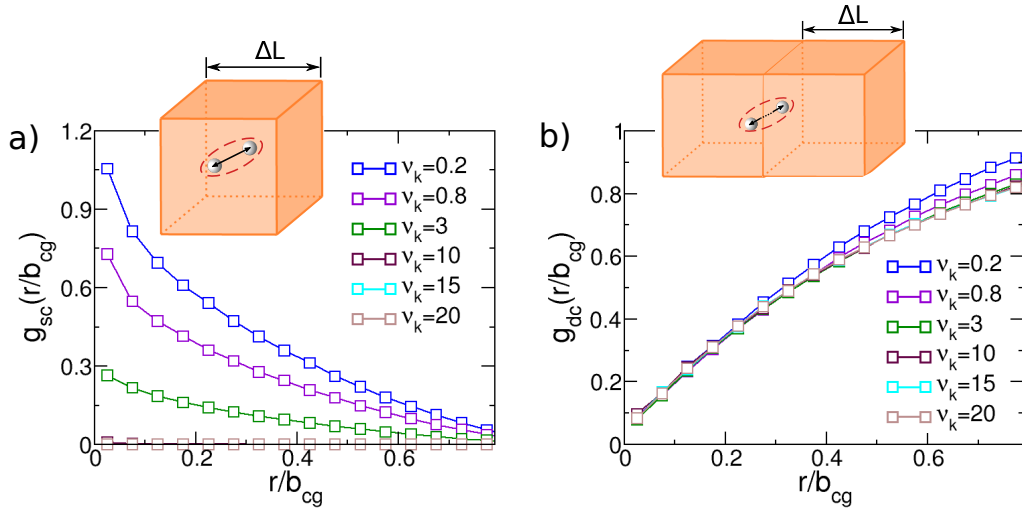


FIGURE 4.8: The decomposed radial distribution functions obtained from mesoscopic models mapped from B2c. The mesoscopic models have the same average number of overlapping particles  $\eta = 1$  and different repulsion strength  $v_k$  (see legends). Panel a shows the radial distribution function  $g_{sc}(r)$  between pairs within the same cell. Panel b shows the radial distribution function  $g_{dc}(r)$  between pairs involving two different neighboring cells. The values of  $r/b_{cg}$  range here from 0 to the cell size, i.e.  $\Delta L/b_{cg} = 0.79$  for all the models.

Since the closed-packed pairs only exist in the same or neighboring cells, we decompose the part of  $g(r)$  when  $r \leq \Delta L$ . For the melts involved in Fig. 4.6, they have the same lattice size  $\Delta L/b_{cg} = 0.79$ . The corresponding results are presented in Fig. 4.8a and b, respectively. From  $g_{sc}(r)$  we conclude that there are less and less pairs of beads found in the same cell as  $v_k$  increases.



When  $\nu_k \geq 10$ ,  $g_{sc}(r) \approx 0$ , and all non-zero data points are less than  $10^{-4}$ . In contrast, the saturation of  $g_{dc}(r)$  demonstrates that the contribution from beads in neighboring cells becomes constant at large  $\nu_k$ . This result verifies our hypothesis, stating that beads in two neighboring cells can be arbitrary close and cannot be separated by increasing  $\nu_k$ .

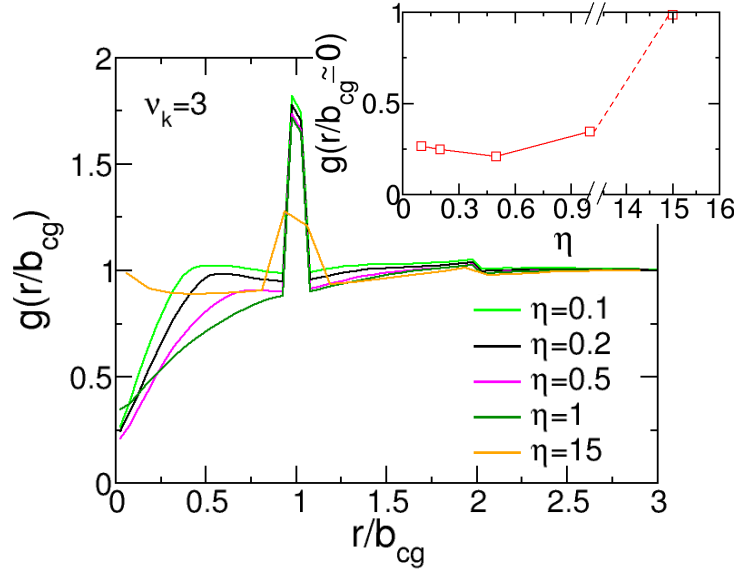


FIGURE 4.9: The radial distribution functions obtained from mesoscopic models mapped from B2c. The mesoscopic models have the same repulsion strength  $\nu_k = 3$  and different average number of overlapping particles  $\eta$  (see legends).

The  $g(r)$  of melts with different  $\eta$  are compared in Fig. 4.9. Because of the softness of our potential, it is possible to employ a high value of  $\eta$ . For  $\eta = 15$ ,  $g(r \approx 0) \sim 1$ , indicating that the beads are locally highly overlapped. One can reduce the overlapping by using a smaller  $\eta$ , because it is energetically favorable to have beads in different cells at low  $\eta$ . For  $\eta \leq 1$ , we observe that the width of correlation hole decreases as  $\eta$  becomes smaller. This is because  $\eta$  is reduced by reducing the range of interactions  $\Delta L$ . However, the depth of correlation hole shows a more complex behavior. The inset of Fig. 4.9 shows the variation of  $g(r \approx 0)$  with respect to  $\eta$ . It can be seen that,  $g(r \approx 0)$  decreases from  $\sim 1$  to  $\sim 0.2$  when  $\eta$  is reduced from 15 to 0.5. However, if we further reduce  $\eta$ , the depth of  $g(r)$  becomes more shallow. The non-monotonous change of  $g(r \approx 0)$  as a function of  $\eta$  has the same origin as the non-trivial effects of  $\nu_k$  on  $g(r \approx 0)$ . By decomposing the  $g(r)$  from Fig. 4.9 into  $g_{sc}(r)$  and  $g_{dc}(r)$ , shown in Fig. 4.10, we demonstrate that the contribution from pairs in the same cell decreases as  $\eta$  becomes smaller. In contrast, the contribution from pairs in neighboring cells increases. When

$\eta \leq 0.5$ , the value of  $g_{sc}(r \approx 0)$  starts to be comparable or even smaller than  $g_{dc}(r \approx 0)$ . Consequently, the behavior of  $g(r \approx 0)$  is dominated by the  $g_{dc}(r \approx 0)$ , making the  $g(r \approx 0)$  to grow again.

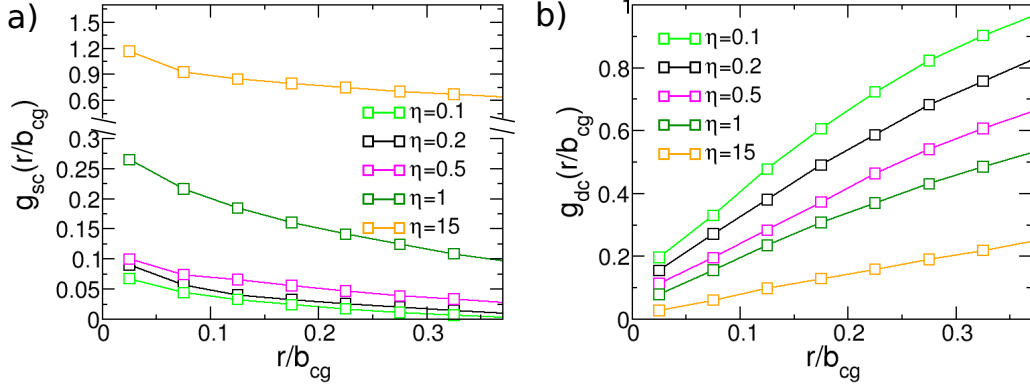


FIGURE 4.10: The decomposed radial distribution functions obtained from mesoscopic models mapped from B2c. The mesoscopic models have the same repulsion strength  $\nu_k = 3$  and different average number of overlapping particles (see legends). Panel a shows the radial distribution function  $g_{sc}(r)$  between pairs within the same cell. Panel b shows the radial distribution function  $g_{dc}(r)$  between pairs involving two different neighboring cells. The values of  $r/b_{cg}$  range from 0 to the smallest cell, i.e.  $\Delta L/b_{cg} = 0.37$  when  $n^* = 0.1$ .

Different from the local liquid structure, the mesoscopic features of the reference microscopic melt can be accurately reproduced by our mesoscopic model. To illustrate this point, we calculate three typical properties which characterize the features on mesoscopic scales: radial distribution function of the COM of chains, mean-squared internal end-to-end distance, and autocorrelation function of bond vectors. In particular, radial distribution function of the COM of chains quantifies the mesoscopic liquid structure within the melts. Mean-squared internal end-to-end distance and autocorrelation function of bond vectors explicitly take into account chain conformations and, similar to knotting properties, contain the features on both local and mesoscopic scales.

The results of radial distribution function of the COM of chains  $g_{chain}(r)$  are shown in Fig. 4.11. Panel a) contains the results obtained from mesoscopic models with constant  $\eta$  and varied  $\nu_k$ , while panel b) contains the results obtained from mesoscopic models with constant  $\nu_k$  and varied  $\eta$ . In both panels, the  $g_{chain}(r)$  obtained from mesoscopic melts are compared with that of the corresponding microscopic melt (red line). The radial distances  $r$  are

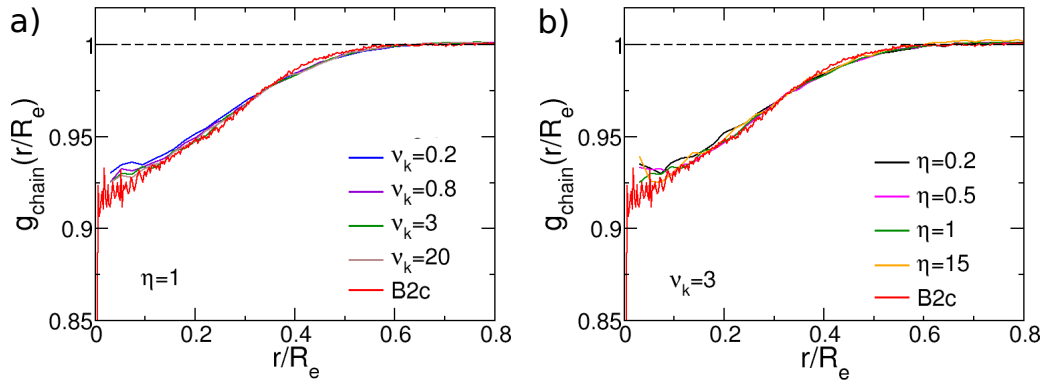


FIGURE 4.11: Radial distribution function  $g_{\text{chain}}(r/R_e)$  of COM of polymer chains. The radius  $r$  is normalized by the end-to-end distance  $R_e$  of the chains.  $g_{\text{chain}}(r/R_e)$  are obtained from mesoscopic melts mapped from the B2c melt (red solid line). The mesoscopic models with a) different repulsion strength  $v_k$ , or b) different average number of overlapping particles  $\eta$  are used to generate these equivalent melts.

normalized by end-to-end distance  $R_e$ . It can be seen that the  $g_{\text{chain}}(r)$  of mesoscopic melts follow closely the  $g_{\text{chain}}(r)$  of microscopic melt. The largest deviation,  $\sim 1.5\%$ , is observed for the mesoscopic melt with  $\eta = 0.2$ .

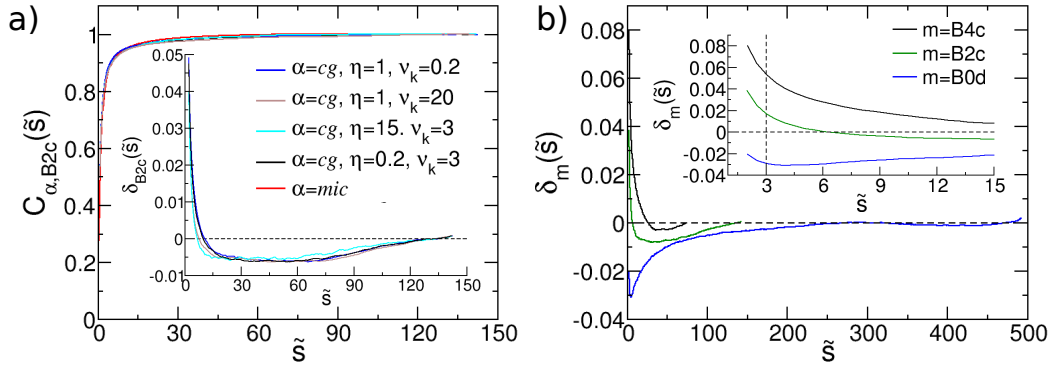


FIGURE 4.12: a) Internal distance plot  $C_{\alpha,B2c}(\tilde{s})$ , presented as a function of  $\tilde{s}$  for mesoscopic melts mapped from the B2c melt. The results obtained from mesoscopic models with several representative parameters are compared with the reference B2c melt (red solid line). The inset shows the relative deviation  $\delta_{B2c}(\tilde{s})$  between mesoscopic and microscopic melts. b)  $\delta_m(\tilde{s})$  of mesoscopic melts mapped from microscopic melts containing chains with different stiffness. The inset shows the enlarged plot at small  $\tilde{s}$ . The vertical dash line indicates the relative deviations at  $\tilde{s} = 3$ .

Fig. 4.12 shows the internal distance plot  $C_{\alpha,m}(s)$ , which is defined as,

$$C_{\alpha,m}(s) \equiv \langle R_{\alpha,m}^2(s) \rangle / s \quad (4.21)$$

where  $\langle R_{\alpha,m}^2(s) \rangle$  is mean squared internal end-to-end distance.  $s$  is chemical distance between monomers  $i$  and  $j$  along the same chain, i.e.,  $s = |i - j|$ .  $\alpha = cg$  or  $mic$ , which indicates a microscopic melt or a mesoscopic melt, respectively. The subscript  $m$  denotes a specific system listed in table 4.1, e.g., B2c.  $C_{\alpha,m}(s)$  is considered as one of the most sensitive quantifiers of polymer conformations<sup>261,262</sup>. In Fig. 4.12a, we compare the  $C_{cg,B2c}(s)$  for several representative mesoscopic analogs of B2c melt with  $C_{mic,B2c}(s)$  obtained from the B2c melt. Although the mesoscopic and microscopic chains have different discretization, i.e.,  $N_{mic} \neq N_{cg}$ , we can compare the  $C_{\alpha,B2c}(s)$  on a common graph using a rescaled chemical distance  $\tilde{s} = s \cdot b_{\alpha} / l_k$ . To better quantify the difference between  $C_{cg,B2c}(s)$  and  $C_{mic,B2c}(s)$ , we define a relative deviation  $\delta_m(\tilde{s})$ ,

$$\delta_m(\tilde{s}) = \frac{C_{cg,m}(\tilde{s}) - C_{mic,m}(\tilde{s})}{C_{mic,m}(\tilde{s})} \quad (4.22)$$

The results of  $\delta_{B2c}(\tilde{s})$ , shown in the inset of Fig. 4.12a, demonstrate that for chemical distances that are equal or larger than three Kuhn segments, the deviation between the internal distance of mesoscopic melts and the reference B2c system is already reduced to  $\sim 3\%$  at most. Such conformational deviation is considered small in other areas of polymer modeling, e.g., hierarchical backmapping<sup>263,264</sup>. For  $\tilde{s} < 3$ ,  $\langle R_{cg,B2c}^2 \rangle$  is much larger than  $\langle R_{mic,B2c}^2 \rangle$ . This large deviation stems from the difference of local chain structure between mesoscopic and microscopic chains.

To better clarify the difference of local chain structure of mesoscopic and microscopic chains, we mapped two additional microscopic melts containing more flexible or stiffer chains, B0d and B4c. The parameters of the corresponding mesoscopic models are listed in table 4.3. Note that  $\epsilon$  of the mesoscopic melt mapped from B0d is very small. This is because the lattice size  $\Delta L$  in the mesoscopic melt representing B0d melt is comparable with bond length  $b_{cg}$ . Then the repulsive interactions between monomers that are nearest neighbors along the chain contribute substantially to local stiffness. Therefore we need to employ smaller  $\epsilon$ .

Fig. 4.12b presents the relative deviation for mesoscopic melts representing B0d and B4c. Because these mesoscopic melts are generated by models with

$\nu_k = 3$  and  $\eta = 1$ , we have added the the relative deviation for B2c when  $\nu_k = 3$  and  $\eta = 1$  to facilitate comparison. From the main plot of Fig. 4.12b, we can see that our mesoscopic melts accurately reproduce the  $\langle R_e^2 \rangle$  of the corresponding microscopic melts, i.e.,  $\delta_m(\tilde{s} = N_k) \sim 0$ . For smaller  $\tilde{s}$ , the relative deviation is small ( $< 3\%$ ) for the most part of the chains. Especially the most flexible chain with  $B = 0$  exhibits the best agreement:  $\delta_{B0d}(\tilde{s}) \approx 0$  within a relatively large range of  $\tilde{s}$ . The deviation at local scales can be seen from the inset of Fig. 4.12b. Compared with  $\delta_{B2c}$ , the relative deviations  $\delta_{B0d}$  and  $\delta_{B4c}$  are somewhat larger. For example, the deviations at  $\tilde{s} = 3$ , indicated by the dash vertical line, are about 3%, 2% and 5% for melts representing B0d, B2c and B4c.

TABLE 4.3: The parameters of mesoscopic melts mapped from the B0d and B4c microsopic melts.

systems	$\nu_k$	$\eta$	$\bar{\rho}_0$ ( $\sigma^{-3}$ )	$\kappa$	$\Delta L$ ( $\sigma$ )	$N_{cg}$	$b_{cg}$ ( $\sigma$ )	$\epsilon$
B0d	3	1	0.65	3	1.15	976	1.01	0.5
B4c			0.19	3	1.7	144	3.5	1.0

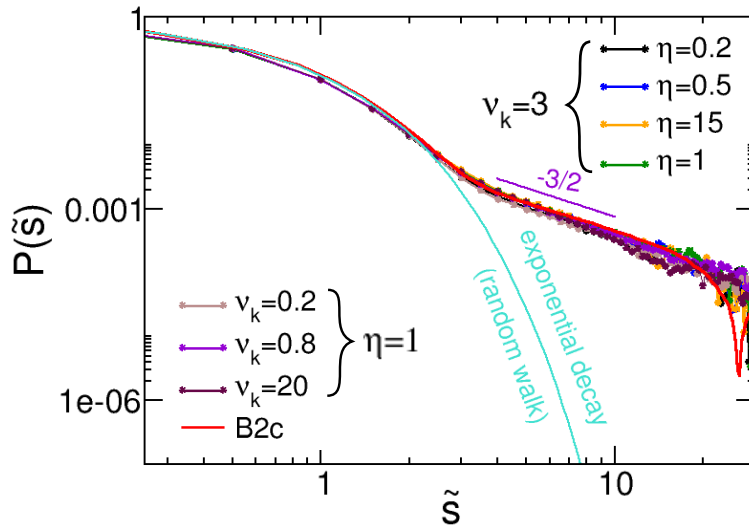


FIGURE 4.13: Bond-bond autocorrelation function for mesoscopic melts mapped from B2c melt. The results obtained from mesoscopic models with different average number of overlapping particles  $\eta$  and repulsion strength  $\nu_k$  are compared with the reference B2c melt (red solid line). The expected power law decay in polymer melts with exponent  $-3/2$  is shown with a purple solid line. The exponential decay of random walks is also shown in the plot.

Fig. 4.13 shows the autocorrelation function of bond vectors  $P(\tilde{s}) = \langle \mathbf{u}(s_0) \mathbf{u}(s_0 + s) \rangle$ . Here  $\mathbf{u}(s_0)$  and  $\mathbf{u}(s_0 + s)$  are vectors oriented along the  $s_0$  and  $s_0 + s$  bonds. For random walks,  $P(s)$  decays exponentially as a function of chemical distance  $s$ . Recent studies<sup>246,247</sup> have demonstrated that in polymer melts  $P(s)$  does not decay exponentially at large  $s$  (as predicted by the Flory Hypothesis) but follows the scaling  $P(s) \sim s^{-3/2}$ . Fig. 4.13 shows the  $P(s)$  calculated for all equivalent mesoscopic representations of B2c melt. To compare with the  $P(s)$  of microscopic melts (red line), we again use the rescaled chemical distance  $\tilde{s}$ . For the region  $0 < \tilde{s} < 10$ , where the statistics are fairly good, we observe that the decay of bond-bond correlations obtained from mesoscopic melts reproduces the correct power-law decay and follows closely the reference data.

## 4.6 Properties of knots in mesoscopic models

From the discussion of structural and conformational properties, we can see that local liquid structure of mesoscopic melts is very coarse compared to the equivalent microscopic melts. Moreover, the local liquid structure of mesoscopic melts with different parameters is also different from each other, although these melts are mesoscopically equivalent to the same reference system. Therefore our mesoscopic melts are well suited for verifying our qualitative predictions based on the simple free-energy model.

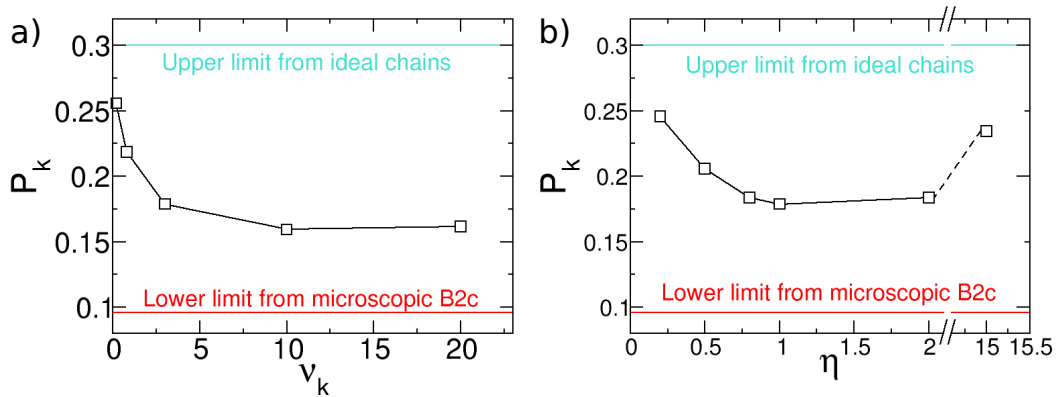


FIGURE 4.14: The influence of a) repulsion strength  $v_k$  and b) average number of overlapping particles  $\eta$  on the knotting probability  $P_k$  of mesoscopic melts. All the mesoscopic melts are mesoscopically-equivalent to the B2c system. The knotting probabilities in the reference B2c, and in random walks with same  $N_k$  are shown with two horizontal solid lines.

We first summarize the knotting probability  $P_k$  in mesoscopic melts mapped from B2c system. According to the reference data provided in ref. [47], the knotting probability in B2c system and the random walks having the same  $N_k$  is 9.58% and 30.05%, respectively. Based on the discussion in section 4.2, this large difference of  $P_k$  between chains in the melt and ideal random walks indicates that the microscopic chains with  $B = 2$  are rather flexible and our mesoscopic model is not expected to reproduce accurately the knotting properties.

In Fig. 4.14, the knotting probability of reference B2c melt and corresponding random walks are indicated by two horizontal solid lines. Indeed, the  $P_k$  in mesoscopic melts (black squares) interpolate between the reference lines. From Fig. 4.14a, we observe that  $P_k$  decreases as repulsion strength  $\nu_k$  becomes larger but converges to a value that is  $\sim 65\%$  larger than the  $P_k$  in the reference B2c melt. This behavior of  $P_k$  stems from the zeroth-order PM scheme which cannot completely avoid close-packed beads even at strong repulsion strengths (see Fig. 4.7). This effect reduces the effective excluded volume, i.e., the parameter  $\tilde{w}$ , speaking in terms of the simple free-energy model.

Fig. 4.14b compares the  $P_k$  in mesoscopic melts generated by models with the same  $\nu_k$  but different average number of overlapping particles  $\eta$ . The dependence of  $P_k$  on  $\eta$  is non-monotonous.  $P_k$  starts from a high value at  $\eta \ll 1$ , decreases as the  $\eta$  increases, then reaches a broad minimum at  $\eta \approx 1$ , and grows again (presumably towards the limit of the ideal chain). As mentioned earlier,  $\eta$  is increased by using larger  $\Delta L$ . Within the regime of weak overlapping ( $\eta < 1$ ), enlarging lattice size  $\Delta L$  increases the effective range of excluded volume  $\tilde{w}$  within mesoscopic melts, which can be seen from the width of correlation hole in  $g(r)$  (see Fig. 4.9). According to the prediction of simple free-energy model, the knotting probability  $P_k$  decreases as the  $\tilde{w}$  increases. Therefore,  $P_k$  decreases with the increasing of  $\eta$  within the regime of weak overlapping. Within the regime of strong overlapping ( $\eta \gg 1$ ), a test bead finds itself in a uniform "background field" of other beads. Because there is no penalty for overlapping, the effective range of excluded volume is not mainly determined by  $\Delta L$ , but highly influenced by the degree of overlapping. Larger  $\eta$  leads to smaller effective range of excluded volume, although  $\Delta L$  is getting larger. Therefore  $P_k$  increases with the increasing of  $\eta$  within the regime of strong overlapping.



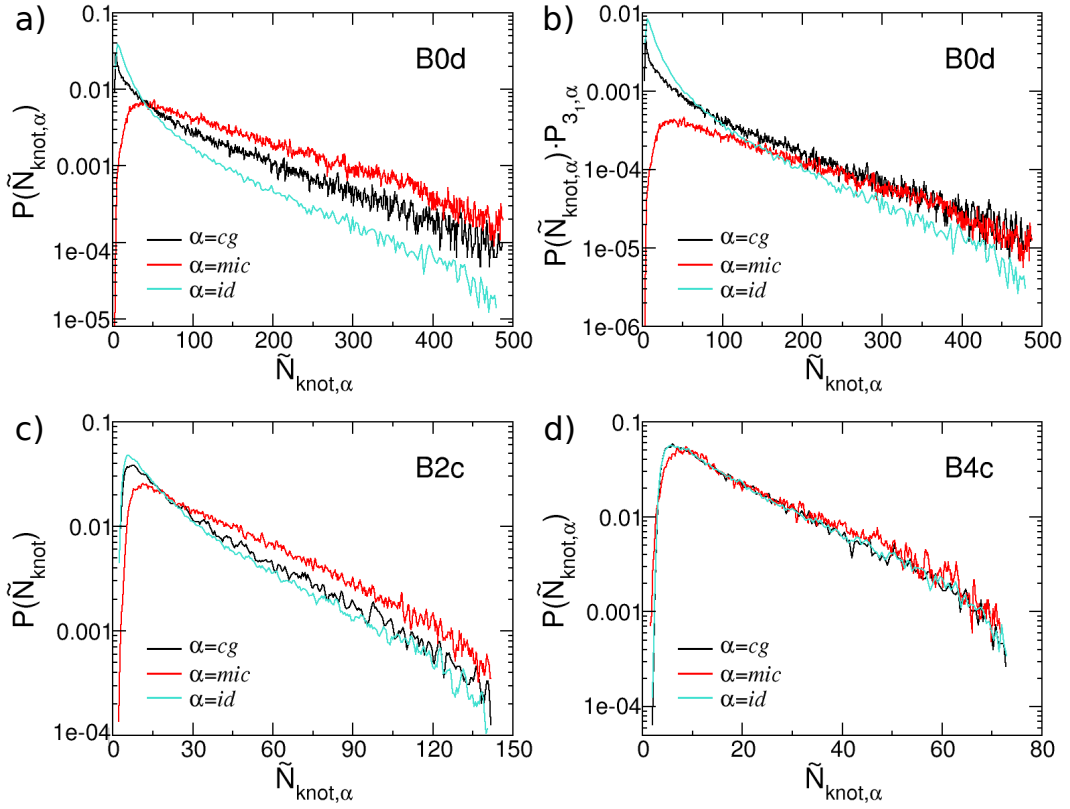


FIGURE 4.15: Comparison of distributions of the size of trefoil knots in microscopic (mic) melts, the equivalent mesoscopic (cg) melts and the ideal chains (id) with the same  $N_k$ . The distributions obtained from the systems mapped from the B0d are presented in the panels a and b considering different ways of normalization. The integrals of distributions in panel a and b are unity and knotting probability of trefoil knots  $P_{3_1, \alpha}$ , respectively. The distributions obtained from the systems mapped from B2c and B4c melts are presented in the panels c and d, respectively. These distributions are normalized to unity.

We now focus on trefoil knots ( $3_1$ ). The distributions of trefoil knot sizes in mesoscopic melts  $P(\tilde{N}_{\text{knot}, cg})$  are shown in Fig. 4.15. Three different mesoscopic melts mapped from microscopic melts B0d, B2c and B4c are considered. All these mesoscopic melts are generated by using the same  $\nu_k$  and  $\eta$ , i.e.,  $\nu_k = 3$  and  $\eta = 1$ . For comparison, Fig. 4.15 also shows the distributions in the reference microscopic melts  $P(\tilde{N}_{\text{knot}, mic})$  and in ideal chains with the same chain length  $P(\tilde{N}_{\text{knot}, id})$ . In panels a, c and d, the distributions are normalized to unity. In panel b, the distributions are normalized to the probability  $P_{3_1, \alpha}$  that a randomly picked chain forms a trefoil knot in the corresponding systems. The necessity of considering two different ways of normalization will become clear in the following discussions.



To better understand the results shown in Fig. 4.15, we discuss the distributions based on their two main features, the peak position and the decay of tail part, which reflects the behavior of relatively small and large knots, respectively. Fig. 4.15a compares the distributions obtained from the B0d melt containing the most flexible chains (mic), and its equivalent systems generated by mesoscopic model (cg) and ideal chain model (id). We first focus on the peaks of the distributions, which correspond to the sizes of the most probable knot  $\tilde{N}_{\text{knot},\alpha}^*$  formed in these models. Comparing to the  $\tilde{N}_{\text{knot,mic}}^*$  of microscopic B0d melt, the sizes of the most probable knot formed in ideal chains and in mesoscopic melts are much smaller. This result is consistent with the prediction obtained from the free-energy model that the size of the most probable knot formed in thicker chains is larger. Additionally, the value of  $\tilde{N}_{\text{knot,cg}}^*$  is very close to the  $\tilde{N}_{\text{knot,id}}^*$  in ideal chains, where the chain thickness is zero. This indicates that the close-packed non-interacting beads in mesoscopic model (see Fig 4.7), which effectively have no repulsion between each other, promote the formation of small knots with size comparable with  $\tilde{N}_{\text{knot,id}}^*$  and dominate the size of the most probable knot. These closed-packed beads stem from the zeroth-order PM scheme and are independent of parameters of the mesoscopic model.

The knots corresponding to the tails of the distributions are no longer tight. Therefore, the simple free-energy model cannot be applied in this regime and simulations become crucial for understanding the behavior of these large knots. The results shown in Fig. 4.15a suggest that the tails of distributions in mesoscopic and microscopic melts are parallel with each other, while the tail part of the distribution in ideal chains has a slightly steeper slope. This point can be better illustrated when the distributions are normalized to the knotting probability of trefoil knots  $P_{3_1,\alpha}$ , shown in Fig. 4.15b. It is clear that the tails of  $P(\tilde{N}_{\text{knot,cg}}) \cdot P_{3_1,\text{cg}}$  and  $P(\tilde{N}_{\text{knot,mic}}) \cdot P_{3_1,\text{mic}}$  overlap with each other, and they are both above the ideal chain curve. Moreover, by normalizing the size distributions to  $P_{3_1,\text{cg}}$ , one obtains the distributions of the probability to obtain a trefoil knot with a certain size. Therefore, Fig. 4.15a also demonstrates that the probability that a randomly picked chain forms a relatively large trefoil knot in ideal chains is smaller than that of polymer melts.

From previous studies, it is expected that the trefoil size distributions follow universal limiting behavior when  $\tilde{N}_{\text{knot},\alpha}$  is very large. For example, for trefoil knots formed in an isolated closed self-avoiding loop, it is known that

the size distribution follows a power-law decay<sup>265</sup> when knot size is substantially larger than the size of the most probable knot. The power-law decay also can be observed in distributions obtained from linear ideal chains<sup>47</sup> after appropriate chain end corrections have been applied. However, the limiting behavior of  $P(\tilde{N}_{\text{knot},\alpha})$  in polymer melts has not been investigated so far. We cannot conclude on the limiting behavior in polymer melts based on our results, although the slopes of the tails of  $P(\tilde{N}_{\text{knot},\text{mic}})$  and  $P(\tilde{N}_{\text{knot},\text{cg}})$  are different from that of  $P(\tilde{N}_{\text{knot},\text{id}})$ . The reason is that the difference in the behavior of tail parts observed in Fig. 4.15 can be caused by two different reasons.

First of all, it is possible that the chain length  $N_k$  of systems in Fig. 4.15a is not long enough to show the limiting behavior, and the difference in tail parts only indicates different cross-overs from the behavior of small knots to that of very large knots. Within the cross-over regime, the distributions are still influenced by the behavior of relatively small knots and have not fully shown the limiting behavior. We already know that the behavior of small knots is different in ideal chains and polymer melts. Therefore, if  $N_k$  is not large enough, the observed difference in tail parts of the distributions in ideal chains and polymer melts is simply caused by the strong deviation between the behavior of small knots, and the limiting behavior might be not shown at all.

On the other hand, it is also possible that the limiting behavior in ideal chains and melts is indeed different. This can be understood when we consider an important property of polymer melts, the invariant degree of polymerization  $\sqrt{\bar{N}}$ . For the B0d melts, the  $\sqrt{\bar{N}}$  is very small and only 59.8 (see table 4.1). By default, the chain conformations in such melts strongly deviate from the ideal chain statistics. Therefore, the behavior of large knots formed in ideal chains can be very different from that of knots formed in melts, which results in different limiting behavior of the distributions in ideal chains and polymer melts.

Note that the difference in tail parts observed in Figs. 4.15a and b also can be a result of a synergy of both two influencing factors, i.e., cross-over and  $\sqrt{\bar{N}}$ . To draw a solid conclusion on the limiting behavior of distributions obtained from polymer melts, one needs to model melts containing much longer chains.

Figs. 4.15c and d shows the distributions obtained from mesoscopic melts

mapped from B2c and B4c, respectively. For the tight knots, as expected by the simple free-energy model, the influence of local liquid structure on knotting properties is weaker as chains become stiffer. Especially in Fig. 4.15d, we observe that  $\tilde{N}_{\text{knot,id}}^* \approx \tilde{N}_{\text{knot,cg}}^*$  and these two values are only slightly smaller than  $\tilde{N}_{\text{knot,mic}}^*$ . To better quantify the deviation, we define a relative deviation  $\delta_{\text{knot}}$ . For example, when comparing mesoscopic and microscopic melts the  $\delta_{\text{knot}}$  is,

$$\delta_{\text{knot}} = \frac{2(\tilde{N}_{\text{knot,mic}}^* - \tilde{N}_{\text{knot,cg}}^*)}{\tilde{N}_{\text{knot,mic}}^* + \tilde{N}_{\text{knot,cg}}^*} \quad (4.23)$$

In panel d, the relative deviation between mesoscopic and microscopic melts  $\delta_{\text{knot}}$  is 38%, which is smaller than the relative deviation observed in panels a and c, where  $\delta_{\text{knot}}$  is 162 % and 52 %, respectively.

Interestingly, for the tail parts of distributions in Fig. 4.15d, all three models agree with each other. We can understand this observation from two perspectives. First of all, the similar behavior of small tight knots (local regime) makes the behavior within cross-over regime of  $P(\tilde{N}_{\text{knot,id}})$  and  $P(\tilde{N}_{\text{knot,cg}})$  close to that of  $P(\tilde{N}_{\text{knot,mic}})$ . Second, because the  $\sqrt{N}$  of B4c melt is already very large, i.e.,  $\sqrt{N} = 256.9$ , the chain conformations approach the ideal chain limit. Therefore, both ideal chain and mesoscopic model can describe the knotting behavior of B4c melt quite well. Fig. 4.15c shows an intermediate case. The chains are stiffer than the chains in B0d melt but more flexible than chains in B4c melt. The  $\sqrt{N} = 94.8$  (see table 4.1). In both local and tail parts of the distributions, the deviations of  $P(\tilde{N}_{\text{knot,id}})$  and  $P(\tilde{N}_{\text{knot,cg}})$  with respect to the  $P(\tilde{N}_{\text{knot,mic}})$  are weaker than the deviations in Fig. 4.15a but stronger than that in Fig. 4.15d.

From the results shown in Fig. 4.15, we can draw an important conclusion: the stiffer the chains in microscopic melts, the better the agreement between knotting properties in mesoscopic and microscopic melts. However, this conclusion is based on the results of the simplest trefoil knots. It is important to investigate whether this conclusion holds for more complex knots. Therefore, we mapped all the microscopic melts listed in table 4.1 by employing  $\nu_k = 3$  and  $\eta = 1$ . The total knotting probability (Fig. 4.16) is analyzed, which takes into account all the possible knots types in the systems. We observe that, indeed the difference between  $P_k$  in mesoscopic and microscopic melts decreases as the chains in microscopic melts become stiffer. For the

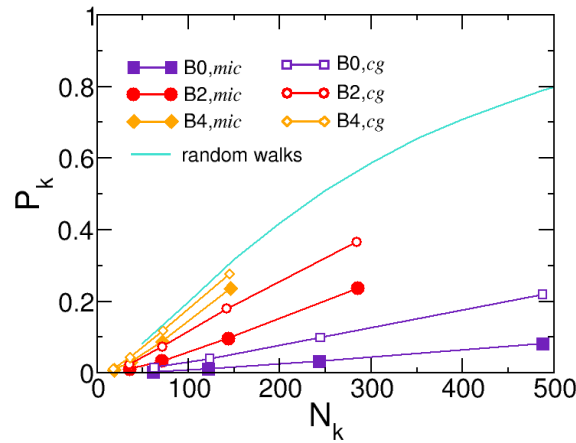


FIGURE 4.16: Comparison of knotting probabilities in microscopic melts (lines with filled symbols) and mesoscopic melts (lines with open symbols). The results of random walks are shown by a solid line. The reference results obtained from microscopic melts and random walks are taken from ref [47].

melts containing the most stiff chains ( $B = 4$ ), the  $P_k$  obtained from microscopic, mesoscopic, and ideal chain models are very close to each other. Accordingly, we can expect that, as the microscopic chains become stiffer, the mesoscopic model also can reproduce the behavior of knots with more complex topologies.

## 4.7 Summary and conclusions

Our work focused on a fundamental question, whether and under which condition mesoscopic models with soft potentials can describe the knotting behavior of polymer melts. We employed a typical mesoscopic model representing polymers by wormlike chains and defining the non-bonded interactions through a generic soft repulsive potential based on a PM scheme. We chose the PM-based non-bonded potential to deliberately create melts with crude local liquid structure. The model was parameterized to accurately reproduce mesoscopic structure and conformations of melts that have been previously modeled<sup>47</sup> with a bead-spring model. The latter captures<sup>51</sup> generic features of polymer conformations and structures at all length scales and provides, therefore, reliable reference data on knots.

We compared characteristic knotting properties in mesoscopic and reference microscopic melts. Different microscopic melts containing chains with different stiffness were considered. For the simplest possible knot, the trefoil knot, we analyzed the distributions of knot sizes (length of chain contour involved in the knot). Regarding general knotting properties, we compared the probability that a chain is in knotted state.

The main conclusion in this work is that mesoscopic models can accurately reproduce the knotting properties of microscopic melts when the characteristic length scale associated with the stiffness of microscopic chains is substantially larger than the size of excluded volume. This conclusion was first illustrated by considering the size distribution of trefoil knots in polymer melts. The size distributions were discussed by focusing on their peak position and tail part. The position of peak reflects the knotting behavior of relatively small trefoil knots, while the behavior of larger trefoil knots is described by the tail part of distributions.

For relatively small trefoil knots, our simulation results indicated that, the knotting behavior is sensitive to local liquid structure, but this sensitivity decreases as the microscopic chains become stiffer. The local liquid structure in mesoscopic melts was found to be different from that of the traditional bead-spring model with hard excluded-volume and is very crude. Therefore, mesoscopic models can accurately reproduce the behavior of relatively small trefoil knots in microscopic melts only if the microscopic chains are sufficiently stiff.

The knotting behavior of small trefoil knots was qualitatively explained through a simple free-energy model. This model is developed for relatively small trefoil knots formed in single chains<sup>241,248</sup>. It claims that the free energy cost for forming such a trefoil knot includes the bending energy and the entropy loss caused by confining chain contour into the knot core. The bending energy is independent of the local liquid structure, while the entropy loss due to confinement is influenced by how the length scale of chain stiffness, e.g., the length of Kuhn segment  $l_k$ , compares with the chain thickness  $w$ , which is determined by the size of monomer-monomer excluded volume. When the ratio  $\tilde{w} = w/l_k$  is very small, the behavior of relatively small trefoil knots formed in microscopic melts is close to that in the ideal chains, meaning the influence of local liquid structure on knotting behavior is marginal. Therefore, in such systems, mesoscopic models can accurately describe knots

even though the local liquid structure is simplified compared to microscopic melts.

For larger trefoil knots, the free-energy model is not valid and our simulations provided important insights for understanding the corresponding knotting behavior. According to earlier studies of single chains<sup>265</sup>, one can expect that very large knots formed in polymer melts may follow certain universal limiting behavior. Though the size of knots observed in our study is not large enough, and we cannot conclude on the limiting behavior in polymer melts. For the range of  $\tilde{N}_{\text{knot}}$  involved in this study, we expect there are two possible reasons that may influence the behavior of large knots observed in our study, because the behavior of observed large knots mainly corresponds to the behavior within cross-over regime. Within the cross-over regime, the corresponding knotting behavior gradually approaches the limiting behavior, but is still influenced by the behavior of smaller knots. Accordingly, on the one hand, the ability of mesoscopic model to describe the behavior of observed large knots is influenced by the agreement between the behavior of small knots in mesoscopic and microscopic melts. On the other hand, the behavior of the observed large knots can also be influenced by the quantity  $\sqrt{\tilde{N}}$ , which frequently enters the universal functions of conformational and structural properties of polymer melts. Because mesoscopic models can easily reproduce the  $\sqrt{\tilde{N}}$  of microscopic melts, the behavior of large knots formed in reference microscopic melts can be accurately reproduced by mesoscopic models when the chains in microscopic melts are sufficiently stiff, so that the agreement between the behavior of small knots in mesoscopic and microscopic melts is good enough.

Additionally, to demonstrate that the discussions on trefoil knots can be applied to more complex knots, we considered another property, total knotting probability  $P_k$ . It is affected by all the possible knot types formed in the systems. We observed that the knotting probability of mesoscopic melts is closer to that of microscopic melts when the microscopic chains are stiffer. This observation is consistent with the conclusion obtained from the analysis of trefoil knots. Therefore, we expect the same conclusion also holds for more complex knot types and mesoscopic models can accurately reproduce the properties of all the knots formed in microscopic melts when the microscopic chains are substantially stiff.

A corollary of our main conclusion is that knotting properties in melts of

chains with excluded volume converge to their counterparts in ideal chains, as  $\tilde{w}$  decreases. This trend has been observed in an earlier modeling study<sup>47</sup> but was not linked to knot thermodynamics. In our study the trends of all knotting properties as a function of  $\tilde{w}$  are consistent with this expectation.

Interestingly, for flexible chains with non-negligible  $\tilde{w}$ , the deviation of knotting properties between mesoscopic and microscopic melts has been observed even though other conformational descriptors matched very well. Specifically, the deviation of internal distance plots at chemical distances larger than a few Kuhn segments was less than 2%. This observation is important methodologically, because it suggests that knots provide an additional sensitive quantifier of chain conformations.

To summarize, one encouraging message that our study conveys is that mesoscopic models with soft potentials can be used to study polymer knots in melts where the characteristic length scale of chain stiffness is substantially larger than the size of the monomer-monomer excluded volume. In this way, it is possible to benefit from the computational efficiency of mesoscopic models and study open questions related to the fundamental physics of knots in polymers. For example, as mentioned earlier, one can simulate melts containing extremely long chains and investigate the limiting behavior of very large knots. Besides, it would be of interest to explore the behavior of knots in confinement, in mixtures, in chains with special structures, etc.





## Chapter 5

# Summary and conclusions

In this thesis, we focused on modeling polymeric systems using drastically CG mesoscopic models. These models use CG beads to represent a large number of microscopic degrees of freedom. Consequently, these CG beads interact with each other via soft potentials<sup>20–22</sup>. The reduced degrees of freedom and soft potentials allow drastically CG models to access large length and time scales, which are frequently involved in polymeric systems.

However, drastically CG mesoscopic models are designed to accurately reproduce features on mesoscopic scales, and many features on small scales in these models are simplified, such as local features of polymer chains and local molecular arrangement (packing) of the materials. Yet many interesting properties of polymeric systems are affected not merely by mesoscopic features, but also by features on small scales. Therefore, a basic methodological question arises: can one use drastically CG models to study properties affected by features on multiple scales (multiscale properties)? Motivated by this question, we considered two cases in which a typical mesoscopic model is employed to study representative multiscale properties.

The employed model belongs to a class of mesoscopic models that have been successfully used to address a broad range of questions in polymers<sup>99,101–103</sup>. These models are developed through a functional-based approach and consist of separated bonded and non-bonded potentials. The bonded potential describes the chain connectivity explicitly through particle coordinates. The non-bonded potential is expressed by a functional of local density fields. After defining the local density fields through particle coordinates, the functional-based interaction is further converted into a particle-based interaction. In the studies presented in this thesis, we used generic discrete

WLC model to describe polymer chains, and a particle-to-mesh scheme was used to define local density fields based on particle coordinates. The systems described by the mesoscopic model were studied using MC simulation method.

In Chapter 3, we used the mesoscopic model to simulate disordered morphologies in blend- and BCP-based active layers of PLEDs and correlated the morphologies with properties related to charge transport. The properties related to charge transport are affected by multiscale features and here we call them charge transport properties in short. The simulated disordered morphologies were characterized by analyzing the local composition around particles. Our results suggested that the morphologies within active layers based on BCPs and equivalent blends are structurally different, and BCPs show stronger local segregation when systems approach the order-disorder transition. These morphologies were linked to charge transport properties through a simple percolation analysis, which identifies the clusters providing conductive pathways. Because we have accessed experiment-relevant scales with the mesoscopic model, the results obtained from the analysis provided useful guidance for future experiments. For example, the impact of processing temperatures, compositions, and finite size of active layers on charge transport properties was discussed based on our percolation analysis.

To illustrate how the results of charge transport properties are influenced by the simplified description of local features in the mesoscopic model, we considered different approaches of performing the percolation analysis. In the first approach, the structure on small scales within the model was used to define percolation, e.g., distances between CG beads. The second approach defined percolation only based on the density distribution on substantially larger scales. Interestingly, the two approaches produced quantitatively different but qualitatively same results. This observation indicates that our mesoscopic model cannot quantitatively reproduce charge transport properties of active layers, but is still useful for qualitatively predicting their dependence on mesoscopic features of the morphology within the layers.

In Chapter 4, we employed the mesoscopic model to investigate the knotting properties of polymer melts. In an earlier study<sup>47</sup>, the knotting properties in polymer melts were found to be influenced not only by mesoscopic chain features but also by the excluded volume of beads. We compared the knotting properties of microscopically-resolved polymer melts generated in this

earlier study with that of mesoscopically-equivalent melts generated by our mesoscopic model. In the earlier study, they employed a bead-spring model which accounts for excluded volume and reproduces the general features on both small and large scales. From the comparison, we observed that the influence of excluded volume on the knotting properties can be either significant or weak depending on specific features of melts. When another local feature of melts, the length scale describing the stiffness of chains, e.g., the Kuhn length, is substantially larger than the size of excluded volume, the local feature influencing the knotting properties is not the excluded volume, but the chain stiffness. Otherwise, the knotting properties are highly influenced by the excluded volume. This finding is complementary to the earlier study. Because the WLC model was parameterized to accurately reproduce the chain stiffness of polymer melts, our mesoscopic model can quantitatively reproduce the knotting properties of those polymer melts where the chain stiffness is substantially larger than the size of excluded volume.

These two studies demonstrated that, the accuracy of mesoscopic models reduces as we approach the microscopic scales. Still, some of the microscopic features can be described reasonably well by mesoscopic models. Usually it is easier to reproduce with mesoscopic models some key properties related to chain conformations, e.g., chain stiffness, than the local molecular arrangement. Therefore, mesoscopic models describe better those phenomena and properties that are dominated on small scales by the behavior of chain conformations and not the liquid structure. The case of polymer knots considered in this thesis is an illustrative example.

In any case, to rigorously study multiscale properties, mesoscopic models should be incorporated into hierarchical back-mapping schemes<sup>93–95</sup>. Then the mesoscopic model delivers an accurate description of the material on large scales, and the underlying microscopic picture is recovered through the insertion of atomistic degrees of freedom. Of course, one requirement for performing hierarchical back-mapping is the appropriate design of mesoscopic models<sup>95</sup>. The mesoscopic models should be designed in a way to accurately reproduce the conformational and structural features that are mandatory for the insertion of finer details. Note that this requirement is not fulfilled by the specific mesoscopic model employed in this thesis. In the future, to simulate multiscale properties of polymeric systems, it is important to develop mesoscopic models, which facilitate the hierarchical back-mapping, especially for complex multi-component systems.



# Appendix

## Results for dilution 1:2

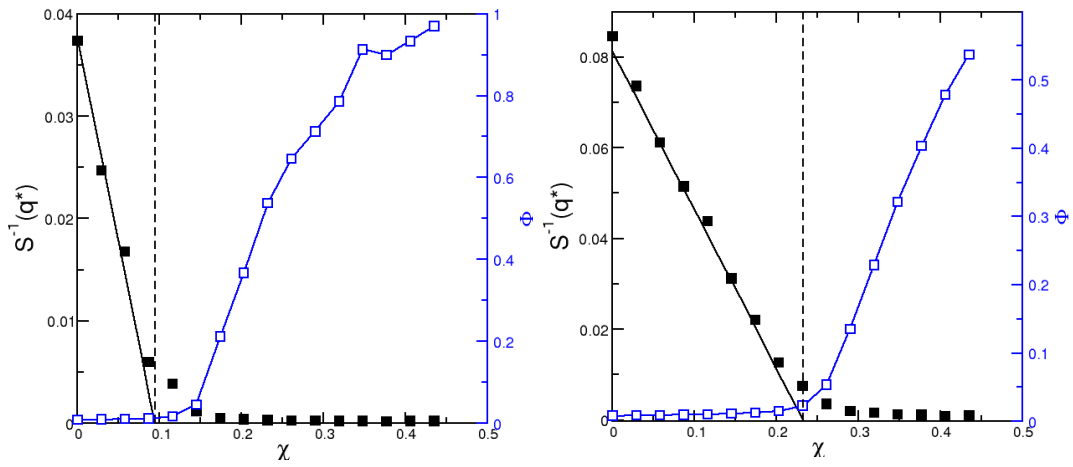


FIGURE A.1: Structure factors (black squares) and order parameters (blue open squares) calculated from MC simulations for blends (left panel) and BCPs (right panel) at dilution 1:2. Black solid lines show the RPA prediction:  $1/S_{\text{RPA}}(q^*, \lambda\chi_s)$  where  $\lambda$  is a renormalization coefficient (see main paper). Black dashed lines indicate the location of RPA spinodals,  $\chi_s = 0.085$  (blend) and  $\chi_s = 0.232$  (BCP).

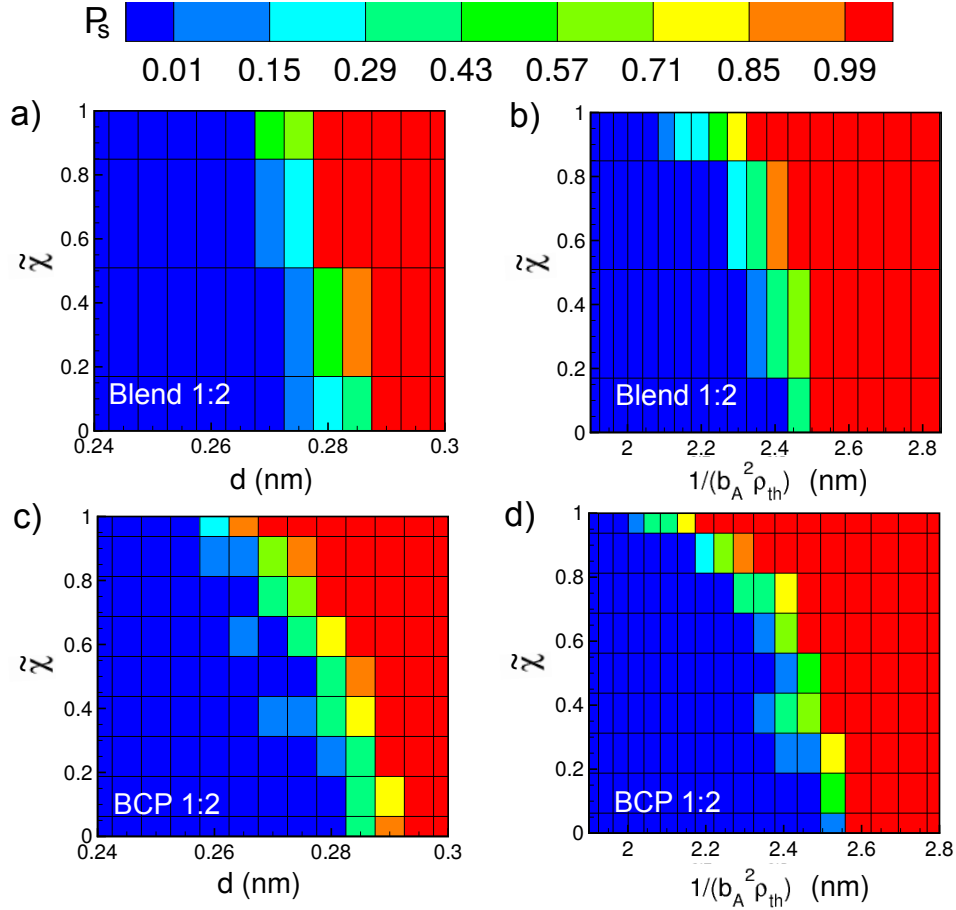


FIGURE A.2: Contour plots quantifying the probability,  $P_s$ , to observe a spanning PPV cluster in disordered blends and BCPs with dilution 1:2. Blue and red colors correspond to low and high probabilities, respectively. Panels a and c demonstrate the  $P_s$  calculated for various normalized  $\chi$  and hopping thresholds  $d$  using the continuum-space percolation analysis. The type of the mixture is indicated at each panel. Panels b and d demonstrate the  $P_s$  calculated for the same mixtures but using the lattice-based percolation approach. The PPV density threshold used in this analysis is denoted by  $\rho_{th}$  (see main paper for details).

# Acknowledgements

Since my first day in the Theory Group of Max-Planck-Institute for Polymer Research on 1st August 2016, I always want to thank dozens of individuals, who have helped me in various stages of my journey to pursue my PhD. It is a pleasant opportunity for me to acknowledge them in this section publicly.

First of all, I would like to express my sincere gratitude to my supervisor Prof. Kurt Kremer. I am privileged to have had the opportunity to join his group and share his exceptional scientific knowledge. All the support and guidance he gave me have been invaluable in encouraging me to pursue scientific works.

I would also like to extend my deepest gratitude to my patient and supportive project leader Dr. Kostas Daoulas, without whom, this thesis could not have been completed. Over the last four years, he has generously shared his time and vast experience of research with me. During the most challenging times when writing this thesis, his persistent nurturing and professional advice helped me in all the time of writing. I have learned a lot from him, especially about how to do interesting and rigorous research, which will be kept as my lifelong treasure.

Additionally, I would like to thank my co-supervisor Prof. Björn Baumeier, for his warm encouragement and helpful feedback on my studies. Thanks should also go to my mentor Dr. Jasper Michels for providing me thoughtful comments and recommendations on the study related to polymeric light-emitting diodes.

I would also like to express my great appreciation to Dr. Peter Virnau for his constructive suggestions during the planning and development of the study of knotting properties. He has also provided great assistance in knot analysis. The successful completion of the study of knotting properties also inevitably depended upon the generous help of Dr. Hendrik Meyer, who has provided me not only important source data but also insightful suggestions.

Furthermore, I really appreciate the friendly environment in our group and have received tremendous, selfless help from my colleagues. Among them, I want to especially thank Saeed Najafi and Jan Smrek for providing various help when I just started the work in this group, thank Cristina Greco

and Jianguo Zhang for helping with many technical questions, thank Hsiao-Ping Hsu and Leanne Paterson for giving suggestions on my studies, and also thank Bin Song, Chan Liu, Stanard Mebwe Pachong and Yani Zhao for inspirational discussions and their friendship.

Lastly, I owe many thanks to my family, Chao Liu, Anping Zhang, Rongzhen Guo, Shuangan Liu, and Huifang Zhao. Their unconditional love, trust, and support helped me get through my doctoral studies in the most positive way. They have given up many things for me to pursue my PhD. My most heartfelt thanks to each of them.



# Bibliography

- [1] M. F. Maitz, *Biossurf. Biotribol.*, 2015, **1**, 161–176.
- [2] M. T. DeMeuse, *High Temperature Polymer Blends*, Woodhead Publishing, 2014.
- [3] I. Botiz and B. Darling, *Mat. Today*, 2010, **13**, 42–51.
- [4] Prateek, V. K. Thakur and R. K. Gupta, *Chem. Rev.*, 2016, **116**, 4260–4317.
- [5] P. Bacova, A. N. Rissanou and V. Harmandaris, *Procedia Comput. Sci.*, 2018, **136**, 341–350.
- [6] T. E. Gartner and A. Jayaraman, *Macromolecules*, 2019, **52**, 755–786.
- [7] M. W. Matsen, *J. Phys.: Condens. Matter*, 2002, **14**, R21–R47.
- [8] A. J. Schultz, C. K. Hall and J. Genzer, *Macromolecules*, 2005, **38**, 3007–3016.
- [9] V. Ortiz, S. O. Nielsen, M. Klein and D. E. Discher, *J. Poly. Sci. Part B: Polym. Phys.*, 2006, **44**, 1907–1918.
- [10] L. Ye, H. Hu, M. Ghasemi, T. Wang, B. Collins, J.-H. Kim, K. Jiang, J. Carpenter, H. Li, Z. Li, T. McAfee, J. Zhao, X. Chen, J. Lai, T. Ma, J.-L. Brédas, H. Yan and H. Ade, *Nat. Mater.*, 2018, **17**, 253–260.
- [11] S. Gali, G. D’Avino, P. Aurel, G. Han, Y. Yi, T. Papadopoulos, V. Coropceanu, J.-L. Brédas, G. Hadziioannou, C. Zannoni and L. Muccioli, *J. Chem. Phys.*, 2017, **147**, 134904.
- [12] A. A. Guilbert, M. Zbiri, A. D. Dunbar and J. Nelson, *J. Chem. Phys.*, 2017, **121**, 9073–9080.
- [13] D. M. Huang, R. Faller, K. Do and A. J. Moulé, *J. Chem. Theory Comput.*, 2009, **6**, 526–537.
- [14] R. Bhowmik, R. J. Berry, V. Varshney, M. F. Durstock and B. J. Leever, *J. Chem. Phys. C*, 2015, **119**, 27909–27918.

- [15] C. I. Wang, C. H. Hsu and C. C. Hua, *J. Polym. Res.*, 2013, **20**, 188.
- [16] A. R. Ashrafi, K. Shankar and P. Choi, *ACS Appl. Mater. Interfaces.*, 2013, **5**, 4617–4624.
- [17] A. Gooneie, S. Schuschnigg and C. Holzer, *Polymers*, 2017, **9**, 16.
- [18] J. A. Pomoposo, *Single-chain Polymer Nanoparticles: Synthesis, Characterization, Simulations, and Applications*, John Wiley & Sons, 2017.
- [19] P. de Gennes, *Scaling Concepts in Polymer Physics*, Cornell University Press, Ithaca, 1979.
- [20] S. H. L. Klapp, D. J. Diestler and M. Schoen, *J. Phys.: Condens. Matter*, 2004, **16**, 7331–7352.
- [21] M. Müller, *J. Stat. Phys.*, 2011, **145**, 967–1016.
- [22] M. Dinpojooh and M. Guenza, *Soft Matter*, 2018, **35**, 7331–7352.
- [23] F. Schmid, in *Handbook of Multiphase Polymer Systems*, Wiley, 2011, pp. 1–63.
- [24] M. Müller, in *Hybrid Particle-Continuum Methods in Computational Materials Physics*, NIC Series, 2013, pp. 127–232.
- [25] F. J. Martinez-Veracoechea and F. A. Escobedo, *Macromolecules*, 2005, **38**, 8522–8531.
- [26] K. Daoulas, M. Müller, J. J. de Pablo, P. F. Nealey and G. D. Smith, *Soft Matter*, 2006, **2**, 573–583.
- [27] J. Glaser, P. Medapuram, T. M. Beardsley, M. W. Matsen and D. C. Morse, *PRL*, 2014, **113**, 068302.
- [28] J. Feng and E. Ruckenstein, *J. Chem. Phys.*, 2007, **126**, 124902.
- [29] J. Houdayer and M. Müller, *Macromolecules*, 2004, **37**, 4283–4295.
- [30] K. Daoulas and M. Müller, *J. Chem. Phys.*, 2006, **125**, 184904.
- [31] F. A. Detcheverry, H. Kang, K. Daoulas, M. Müller, P. F. Nealey and J. J. de Pablo, *Macromolecules*, 2008, **41**, 4989–5001.
- [32] W. Li and M. Müller, *Annu. Rev. Chem. Biomol. Eng.*, 2015, **6**, 187–216.
- [33] L. Schneider and M. Müller, *Macromolecules*, 2019, **52**, 2050–2062.
- [34] M. Müller, *Prog. Polym. Sci.*, 2020, **10**, 101198.

- [35] W. Brütting and C. Adachi, *Physics of Organic Semiconductors*, Wiley-VCH, 2012.
- [36] D. J. Gaspar and E. Polikarpov, *OLED Fundamentals: Materials, Devices and Processing of Organic Light-Emitting Diodes*, CRC Press, 2015.
- [37] J. Brédas, D. Beijonne, V. Coropceanu and J. Cornil, *Chem. Rev.*, 2004, **104**, 4971–5003.
- [38] H. Bässler, *Polym. Advan. Technol.*, 1998, **9**, 402–418.
- [39] H. T. Nicolai, M. Kuik, G. A. H. Wetzelaer, B. de Boer, C. Campbell, C. Risko, J. L. Brédas and P. W. M. Blom, *Nat. Mater.*, 2012, **11**, 882–887.
- [40] M. W. Wu and E. M. Conwell, *Chem. Phys. Lett.*, 1997, **266**, 363–367.
- [41] B. Baumeier, F. May, C. Lennartz and D. Andrienko, *J. Mater. Chem.*, 2012, **22**, 10971–10976.
- [42] V. Rühle, A. Lukyanov, F. May, M. Schrader, T. Vehoff, J. Kirkpatrick, B. Baumeier and D. Andrienko, *Chem. Theory Comput.*, 2011, **11**, 3335–3345.
- [43] N. C. H. Lim and S. E. Jackson, *J. Phys.: Condens. Matter*, 2015, **27**, 354101.
- [44] A. Narros, A. J. Moreno and C. N. Likos, *Macromolecules*, 2013, **46**, 3654–3668.
- [45] L. Dai, B. W. Soh and P. S. Doyle, *Macromolecules*, 2019, **52**, 6792–6800.
- [46] A. V. Vologodskii, A. V. Lukashin, M. D. Frank-Kamenetskii and V. V. Anshelevich, *Sov. Phys. JETP*, 1974, **39**, 1059–1063.
- [47] H. Meyer, E. Horwath and P. Virnau, *ACS Macro. Lett.*, 2018, **7**, 757–761.
- [48] P. Flory, *J. Chem. Phys.*, 1949, **17**, 303–310.
- [49] J. J. de Pablo, *Annu. Rev. Phys. Chem.*, 2011, **62**, 555–574.
- [50] S. J. Marrink, H. J. Risselada, S. Yefimov, D. P. Tieleman and A. H. de Vries, *J. Phys. Chem. B*, 2007, **111**, 7812–7824.
- [51] K. Kremer and G. S. Grest, *J. Chem. Phys.*, 1990, **92**, 5057–5086.
- [52] K. Kremer and G. S. Grest, in *Monte Carlo and Molecular Dynamics Simulations in Polymer Science*, Oxford University Press, 1995, pp. 194–271.
- [53] H. P. Hsu and K. Kremer, *J. Chem. Phys.*, 2016, **144**, 154907.

- [54] S. O. Nielsen, C. F. Lopez, G. Srinivas and M. L. Klein, *J. Phys. Condens. Matter*, 2004, **16**, R481.
- [55] C. Peter and K. Kremer, *Soft Matter*, 2009, **5**, 4357–4366.
- [56] W. G. Noid, *J. Chem. Phys.*, 2013, **139**, 090901.
- [57] M. Praprotnik, L. D. Site and K. Kremer, *Annu. Rev. Phys. Chem.*, 2008, **59**, 545–571.
- [58] W. Paul, D. Y. Yoon and G. D. Smith, *J. Chem. Phys.*, 1995, **103**, 1702–1709.
- [59] G. Milano and F. Müller-Plathe, *J. Chem. Phys. B*, 2005, **109**, 18609–18619.
- [60] I. Y. Lyubimov, J. McCarty, A. Clark, and M. G. Guenza, *J. Chem. Phys.*, 2010, **132**, 224903.
- [61] P. Depa, C. Chen and J. K. Maranas, *J. Chem. Phys.*, 2011, **134**, 014903.
- [62] J. G. Kirkwood, *J. Chem. Phys.*, 1935, **3**, 300–313.
- [63] D. A. McQuarrie, *Statistical Mechanics*, University Science Books, Sausalito, CA, USA, 2000.
- [64] W. Tschöp, K. Kremer, O. Hahn, J. Batoulis and T. Bürger, *Acta Polym.*, 1998, **49**, 61–74.
- [65] D. Reith, M. Pütz and F. Müller-Plathe, *J. Comput. Chem.*, 2003, **24**, 1624–1636.
- [66] S. Izvekov and G. A. Voth, *J. Chem. Phys. B*, 2005, **109**, 2469–2473.
- [67] B. L. Peters, K. M. Salerno, A. Agrawal, D. Perahia and G. S. Grest, *J. Chem. Theory Comput.*, 2017, **13**, 2890–2896.
- [68] C. Scherer and D. Andrienko, *Phys.Chem.Chem.Phys.*, 2018, **20**, 22387–22394.
- [69] T. D. Potter, J. Taschea and M. R. Wilson, *Phys. Chem. Chem. Phys.*, 2019, **21**, 1912–1927.
- [70] S. J. Marrink, A. H. de Vries and A. E. Mark, *J. Phys. Chem.*, 2004, **108**, 750–760.
- [71] E. Brini, E. A. Algaer, P. Ganguly, C. Li, F. Rodriguez-Ropero and N. F. A. van der Vegt, *Soft Matter*, 2013, **9**, 2108–2119.

- [72] T. C. Moore, C. R. Iacovella and C. McCabe, *J. Chem. Phys.*, 2014, **140**, 224104.
- [73] M. Müller, K. Katsov and M. Schick, *J. Polym. Sci., Part B, Polym. Phys.*, 2003, **41**, 1441–1450.
- [74] M. Müller, K. Katsov and M. Schick, *Phys. Rep.*, 2006, **434**, 113–176.
- [75] B. J. Reynwar, G. Illya, V. A. Harmandaris, M. M. Müller, K. Kremer and M. Deserno, *J. Phys. Chem.*, 2007, **108**, 750–760.
- [76] T. D. Potter, J. Tasche, E. L. Barrett, M. Walker and M. R. Wilson, *Liquid Crystals*, 2017, **44**, 1979–1989.
- [77] M. Müller and J. J. de Pablo, *Annu. Rev. Mat. Res.*, 2013, **43**, 1–34.
- [78] W. G. Noid, *Systematic Methods for Structurally Consistent Coarse-grained Models*, Humana Press, 2013.
- [79] V. A. Harmandaris, D. Reith, N. F. A. van der Vegt and K. Kremer, *Macromol. Chem. Phys.*, 2007, **208**, 2109–2120.
- [80] V. A. Harmandaris, N. P. Adhikari, N. F. A. van der Vegt and K. Kremer, *Macromolecules*, 2006, **39**, 6708–6719.
- [81] N. F. A. van der Vegt, C. Peter and K. Kremer, *Coarse-Graining of Condensed Phase and Biomolecular Systems*, CPC Press, Chapman and Hall, 2008.
- [82] C. Peter, L. D. Site and K. Kremer, *Soft Matter*, 2008, **4**, 859–869.
- [83] M. P. Allen and D. J. Tildesley, *Computer Simulation of Liquids*, Oxford University Press, 1987.
- [84] R. L. Henderson, *Phys. Lett.*, 1974, **49A**, 197–198.
- [85] S. Jain, S. Garde and S. K. Kumar, *Ind. Eng. Chem. Res.*, 2006, **45**, 5614–5618.
- [86] M. Guenza, *Eur. Phys. J. Special Topics*, 2015, **224**, 2177–2191.
- [87] Q. Sun, J. Ghosh and R. Faller, in *Coarse-Graining of Condensed Phase and Biomolecular Systems*, CPC Press, 2008, p. 69.
- [88] D. Q. Pike, F. A. Detcheverry, M. Müller and J. de Pablo, *J. Chem. Phys.*, 2009, **131**, 084903.

- [89] H. Kang, F. A. Detcheverry, A. N. Mangham, M. P. Stoykovich, K. Daoulas, R. Hamers, M. Müller, J. J. Pablo and P. F. Nealey, *Phys. Rev. Lett*, 2009, **100**, 148303.
- [90] M. W. Matsen and M. Schick, *Phys. Rev. Lett.*, 1994, **72**, 2660–2663.
- [91] S. F. Edwards, *Proc. Phys. Soc.*, 1965, **85**, 613.
- [92] P. Gemünden, C. Pölking, K. Kremer, D. Andrienko and K. Daoulas, *Macromolecules*, 2013, **46**, 5762–5774.
- [93] G. Zhang, L. A. Moreira, T. Stühn, K. Daoulas and K. Kremer, *ACS Macro Lett.*, 2014, **3**, 198–203.
- [94] G. Zhang, T. Stühn, K. Daoulas and K. Kremer, *J. Chem. Phys*, 2015, **142**, 221102.
- [95] G. Zhang, A. Chazirakis, V. A. Harmandaris, T. Stühn, K. Daoulas and K. Kremer, *Soft Matter*, 2019, **15**, 289–302.
- [96] G. Fredrickson, *The Equilibrium Theory of Inhomogeneous Polymers*, Oxford University, Clarendon, 2006.
- [97] K. Daoulas, in *Handbook of Materials Modeling*, Springer, 2018, pp. 1–19.
- [98] M. Laradji, H. Guo and M. J. Zuckermann, *Phys. Rev. E*, 1994, **49**, 3199–3206.
- [99] M. Müller, *Phys. Rev. E*, 2002, **65**, 030802.
- [100] S. Qi and F. Schmid, *Soft Matter*, 2017, **13**, 7938–7947.
- [101] M. P. Stoykovich, M. Müller, S. O. Kim, H. H. Solak, E. W. Edwards, J. J. de Pablo and P. F. Nealey, *Science*, 2005, **308**, 1442–1446.
- [102] M. Müller and G. D. Smith, *J. Poly. Sci. B: Poly. Phys*, 2005, **43**, 934–958.
- [103] C. Greco, A. Melnyk, K. Kremer, D. Andrienko and K. Daoulas, *Macromolecules*, 2019, **52**, 968–981.
- [104] K. Daoulas, V. Rühle, and K. Kremer, *J. Phys-Condens. Mat.*, 2012, **24**, 284121.
- [105] I. Pagonabarraga and D. Frenkel, *Mol. Simulat.*, 2000, **25**, 167–175.
- [106] S. Y. Trofimoov, E. L. F. Nies and M. A. J. Michels, *J. Chem. Phys.*, 2002, **117**, 9383–9394.
- [107] M. Hömberg and M. Müller, *J. Chem. Phys.*, 2010, **132**, 155104.

- [108] R. Parr and W. Yang, *Density-functional Theory of Atoms and Molecules*, Oxford University, New York, 1989.
- [109] P. Hohenberg and W. Kohn, *Phys. Rev.*, 1964, **136**, B864.
- [110] K. Daoulas and M. Müller, *Adv. Polym. Sci.*, 2010, **224**, 197–233.
- [111] Y. Jiang, C. Greco, K. Daoulas and J. Z. Y. Chen, *Polymers*, 2017, **9**, 48.
- [112] M. Doi and S. F. Edwards, *The Theory of Polymer dynamics*, Oxford University Press, 1986.
- [113] M. Rubinstein and R. H. Colby, *Polymer Physics*, Oxford Univ Press, 2003.
- [114] L. Livadaru, R. R. Netz and H. J. Kreuzer, *Macromolecules*, 2003, **36**, 3732–3744.
- [115] J. Mark, *Physical Properties of Polymers Handbook*, Springer, 2007.
- [116] G. Zhang, K. C. Daoulas and K. Kremer, *Macromol. Chem. Phys.*, 2013, **214**, 214–224.
- [117] B. Steinmüller, M. Müller, K. R. Hambrecht, G. D. Smith and D. Bedrov, *Macromolecules*, 2011, **45**, 1107–1117.
- [118] P. J. Flory, *J. Chem. Phys.*, 1941, **9**, 660–661.
- [119] M. L. Huggins, *J. Chem. Phys.*, 1941, **9**, 440.
- [120] Z.-G. Wang, *J. Chem. Phys.*, 2002, **117**, 481–500.
- [121] D. Ryu, M. Park, S. Chae, J. Jang, J. Kim and T. Russell, *Macromolecules*, 2002, **35**, 8676–8680.
- [122] V. Abetz and P. Simon, *Adv. Polym. Sci.*, 2005, **189**, 125–212.
- [123] H. Eitouni and N. Balsara, in *Physical Properties of Polymers Handbook*, ed. J. Mark, Springer, 2007, ch. 19, pp. 339–357.
- [124] M. Müller and K. Daoulas, *Macromol. Symp.*, 2007, **252**, 68–75.
- [125] M. Deserno and C. Holm, *J. Chem. Phys.*, 1998, **109**, 7678–7693.
- [126] M. Müller and G. Smith, *J. Polym. Sci., Part B. Polym. Phys.*, 2005, **43**, 934–958.
- [127] S. H. L. Klapp, D. J. Diestler and M. Schön, *J. Phys.: Condens. Matter*, 2004, **16**, 7331–7352.

- [128] G. Zhang, K. C. Daoulas and K. Kremer, *Macromol. Chem. Phys.*, 2013, **214**, 214–224.
- [129] A. J. Clark and M. G. Guenza, *J. Chem. Phys.*, 2009, **132**, 044902.
- [130] Y. Norizoe, K. Daoulas and M. Müller, *Faraday Discuss*, 2009, **144**, 369–391.
- [131] M. Müller, *J. Stat. Phys.*, 2011, **145**, 967–1016.
- [132] W. Bruns, L. Motoc and K. F. O'Driscoll, *Monte Carlo Applications in Polymer Science*, Springer-Verlag, Heidelberg, 1981.
- [133] S. K. Kumar, M. Vacatello and D. Y. Yoon, *J. Chem. Phys.*, 1988, **89**, 5206–5215.
- [134] V. G. Mavrantzas and D. N. A. Theodorou, *Macromolecules*, 1998, **31**, 6310–6332.
- [135] M. Doi and S. F. Edward, *The Theory of Polymer Dynamics*, Oxford University Press, 1986.
- [136] F. T. Wall and F. Mandel, *J. Chem. Phys.*, 1975, **63**, 4592–4595.
- [137] D. Frenkel and B. Smit, *Understanding Molecular Simulation: From Algorithms to Applications*, Academic Press, 1996.
- [138] N. Metropolis, A. W. Rosenbluth, M. N. Rosenbluth, A. H. Teller and E. Teller, *J. Chem. Phys.*, 1953, **21**, 1087.
- [139] S. Kumar, M. Vacatello and D. Yoon, *J. Chem. Phys.*, 1988, **89**, 5206–5215.
- [140] V. Mavrantzas and D. Theodorou, *Macromolecules*, 1998, **31**, 6310–6332.
- [141] F. T. Wall and F. Mandell, *J. Chem. Phys.*, 1975, **63**, 4592–4595.
- [142] H. Flyvbjerg and H. G. Petersen, *J. Chem. Phys.*, 1989, **91**, 461–466.
- [143] K. Hong and J. Noolandi, *Macromolecules*, 1981, **14**, 727–736.
- [144] E. Helfand and Y. Tagami, *J. Chem. Phys.*, 1972, **56**, 3592–3601.
- [145] B. Hammouda, *Journal of Non-Crystalline Solids*, 1994, **172–174**, 927–931.
- [146] G. H. Fredrickson, *The Equilibrium Theory of Inhomogeneous Polymer*, Clarendon Press, Oxford, 2006.
- [147] L. Leibler, *Macromolecules*, 1980, **13**, 1602–1617.
- [148] M. Müller and F. Schmid, *Adv. Polym. Sci.*, 2005, **185**, 1–58.



- [149] J. Zhang, K. Kremer, J. J. Michels and K. Daoulas, *Macromolecules*, 2020, **53**, 523–538.
- [150] F. Schmid, *J. Phys.: Condens. Matter*, 1998, **10**, 8105–8138.
- [151] Q. Wang, *J. Chem. Phys.*, 2008, **129**, 054904.
- [152] M. Matsen, in *Soft Matter: Polymer Melts and Mixtures*, ed. G. Gompper and M. Schick, Wiley-VCH, Weinheim, 2006, vol. 1, pp. 87–178.
- [153] J. Hubbard, *Phys. Rev. Lett.*, 1954, **3**, 77–78.
- [154] R. L. Stratonovich, *Sov. Phys. Solid State*, 1958, **2**, 1824.
- [155] S. F. Edwards, *Philis. Mag.*, 1959, **4**, 1171–1182.
- [156] M. Kac, *Phys. Fluids*, 1959, **2**, 8–12.
- [157] S. F. Edwards, *Proc. Phys. Soc.*, 1966, **8**, 265–280.
- [158] K. M. Hong and J. Noolandi, *Macromolecules*, 1981, **14**, 736–742.
- [159] A.-C. Shi, in *Encyclopedia of Polymeric Nanomaterials*, ed. S. Kobayashi and K. Müllen, Springer, Berlin, Heidelberg, 2015, pp. 2199–2203.
- [160] T. Ahmed, *Reservoir Engineering Handbook*, Gulf Professional Publishing, 2018.
- [161] J. H. Kwak and S. Hong, *Linear Algebra*, Springer Science+Business Media, 1997.
- [162] M. Geoghegan and G. Hadziioannou, *Polymer Electronics*, Oxford University Press, Oxford, United Kingdom, 2013.
- [163] M. Kuik, G.-J. Wetzelaer, H. Nicolai, N. Craciun, D. D. Leeuw and P. Blom, *Adv. Mater.*, 2014, **26**, 512–531.
- [164] D. Abbaszadeh, A. Kunz, N. Kotadiya, A. Mondal, D. Andrienko, J. Michels, G.-J. Wetzelaer and P. Blom, *Chem. Mater.*, 2019, **31**, 6380–6386.
- [165] D. Abbaszadeh, A. Kunz, G.-J. Wetzelaer, J. Michels, N. Crăciun, K. Koynov, I. Lieberwirth and P. Blom, *Nat. Mater.*, 2016, **15**, 628–633.
- [166] P. Mark and W. Helfrich, *J. Appl. Phys.*, 1962, **33**, 205–215.
- [167] A. Kunz, P. Blom and J. Michels, *J. Mater. Chem. C*, 2017, **5**, 3042–3048.
- [168] A. Semenov, *Zh. Eksp. Teor. Fiz.*, 1985, **88**, 1242–1256.

- [169] F. Bates and G. Fredrickson, *Annu. Rev. Phys. Chem.*, 1990, **41**, 525–557.
- [170] E. Helfand and Z. Wasserman, *Macromolecules*, 1976, **9**, 879–888.
- [171] P. de Gennes, *J. Phys. (Paris) Lett.*, 1977, **38**, 441–443.
- [172] K. Binder, in *Theories and Mechanism of Phase Transitions, Heterophase Polymerizations, Homopolymerization, Addition Polymerization*, Springer, 1994, pp. 181–299.
- [173] A. Sariban and K. Binder, *J. Chem. Phys.*, 1987, **86**, 5859–5873.
- [174] D. Schwahn, K. Mortensen and H. Yee-Madeira, *Phys. Rev. Lett.*, 1987, **58**, 1544–1546.
- [175] F. Bates, J. Rosedale, P. Stepanek, T. Lodge, P. Wiltzius, G. Fredrickson and R. Hjelm, *Phys. Rev. Lett.*, 1990, **65**, 1893–1896.
- [176] S. Brazovskii, *Sov. Phys. JETP*, 1975, **41**, 85–89.
- [177] G. Fredrickson and E. Helfand, *J. Chem. Phys.*, 1987, **87**, 697–705.
- [178] A. Mayes and M. de la Cruz, *J. Chem. Phys.*, 1991, **95**, 4670–4677.
- [179] I. Hamley and V. Podneks, *Macromolecules*, 1997, **30**, 3701–3703.
- [180] U. Micka and K. Binder, *Macromol. Theory Simul.*, 1995, **4**, 419–447.
- [181] S. Lee, T. Gillard and F. Bates, *AIChE Journal*, 2013, **59**, 3502–3513.
- [182] M. Yadav, F. Bates and D. Morse, *Phys. Rev. Lett.*, 2018, **121**, 127802.
- [183] K. C. Daoulas, V. Rühle and K. Kremer, *J. Phys.: Condens. Matter*, 2012, **24**, 284121.
- [184] J. Martin, E. C. Davidson, C. Greco, W. Xu, J. H. Bannock, A. Agirre, J. de Mello, R. A. Segalman, N. Stingelin and K. Daoulas, *Chem. Mater.*, 2018, **30**, 748–761.
- [185] C. W. T. Bulle-Lieuwma, W. J. H. van Gennip, J. K. J. van Duren, P. Jonkheijm, R. A. J. Janssen and J. W. Niemantsverdriet, *Appl. Surf. Sci.*, 2003, **203-204**, 547–550.
- [186] B. Hsieh, Y. Yu, A. VanLaeken and H. Lee, *Macromolecules*, 1997, **30**, 8094–8095.
- [187] F. Louwet, D. Vanderzande and J. Gelan, *Synth. Met.*, 1992, **52**, 125–130.

- [188] O. Olabisi and K. Adewale, *Handbook of Thermoplastics*, CRC Press, 2015.
- [189] C. L. Gettinger and A. J. Heeger, *Mol. Cryst. Liq. Cryst.*, 1994, **256**, 507–512.
- [190] T. Tadano, R. Zhu, Y. Muroga, T. Hoshi, D. Sasaki, S. Yano and T. Sawaguchi, *Polym. J.*, 2014, **46**, 342–348.
- [191] N. Sato, M. Lögdlund, R. Lazzaroni, W. Salaneck, J.-L. Brédas, D. Bradley, R. Friend and K. Ziemelis, *Chem. Phys.*, 1992, **160**, 299–306.
- [192] U. M. Apel, R. Hentschke and J. Helfrich, *Macromolecules*, 1995, **28**, 1778–1785.
- [193] D. Wu, G. Fredrickson, J. Carton, A. Ajdari and L. Leibler, *J. Polym. Sci., Part B. Polym. Phys.*, 1995, **33**, 2373–2389.
- [194] K. Daoulas and M. Müller, *J. Chem. Phys.*, 2006, **125**, 184904.
- [195] T. Lodge, in *Structure and Dynamics of Polymer and Colloidal Systems*, ed. R. Borsali and R. Pecora, Springer, Netherlands, 2002, pp. 225–262.
- [196] J. Zhang, D. Mukherji, K. Kremer and K. Daoulas, *Soft Matter*, 2018, **14**, 9282–9295.
- [197] I. Szleifer, *Curr. Opin. Colloid In.*, 1996, **1**, 416–423.
- [198] K. Vollmayr, J. Reger, M. Schencher and K. Binder, *Z. Phys. B*, 1993, **91**, 113–125.
- [199] K. Binder, *Rep. Prog. Phys.*, 1997, **60**, 487–559.
- [200] W. Janke, in *Computer Simulations of Surfaces and Interfaces*, ed. B. Dümweg, D. Landau and A. Milchev, Springer, Netherlands, 2003, pp. 111–135.
- [201] M. Müller, in *Soft Matter: Polymer Melts and Mixtures*, ed. G. Gompper and M. Schick, Wiley-VCH, Weinheim, 2006, ch. 3, pp. 179–283.
- [202] D. Morse and J. Chung, *J. Chem. Phys.*, 2009, **130**, 224901.
- [203] J. Glaser, J. Qin, P. Medapuram and D. Morse, *Macromolecules*, 2014, **47**, 851–869.
- [204] T. Beardsley and M. Matsen, *J. Chem. Phys.*, 2019, **150**, 174902.
- [205] M. Müller and K. Binder, *Macromolecules*, 1995, **28**, 1825–1834.

- [206] J. Glaser, P. Medapuram, T. Beardsley, M. Matsen and D. Morse, *Phys. Rev. Lett.*, 2014, **113**, 068302.
- [207] T. Beardsley and M. Matsen, *J. Chem. Phys.*, 2017, **147**, 044905.
- [208] D. Schwahn, K. Mortensen, T. Springer, H. Yee-Madeira and R. Thomas, *J. Chem. Phys.*, 1987, **87**, 6078–6087.
- [209] O. Vassiliev and M. Matsen, *J. Chem. Phys.*, 2003, **118**, 7700–7713.
- [210] S. Salaniwal, R. Kant, R. Colby and S. Kumar, *Macromolecules*, 2002, **35**, 9211–9218.
- [211] P. Medapuram, J. Glaser and D. Morse, *Macromolecules*, 2015, **48**, 819–839.
- [212] R. Noriega, A. Salleo and A. J. Spakowitz, *PNAS*, 2013, **110**, 16315–16320.
- [213] P. Carbone and A. Troisi, *J. Phys. Chem. Lett.*, 2014, **5**, 2637–2641.
- [214] C. Greco, A. Melnyk, K. Kremer, D. Andrienko and K. Daoulas, *Macromolecules*, 2019, **52**, 968–981.
- [215] R. Dewar and C. K. Harris, *J. Phys. A: Math. Gen.*, 1987, **20**, 985–993.
- [216] A. Miller and E. Abrahams, *Phys. Rev.*, 1960, **120**, 745–755.
- [217] H. Bässler, *Phys. Stat. Sol. B*, 1993, **175**, 15–56.
- [218] P. Blom and M. Vissenberg, *Mater. Sci. Eng.*, 2000, **27**, 53–94.
- [219] C. Groves, *Rep. Prog. Phys.*, 2017, **80**, 026502.
- [220] N. Johner, C. Grimaldi, I. Balberg and P. Ryser, *Phys. Rev. B*, 2008, **77**, 174204.
- [221] W. Pasveer, J. Cottaar, C. Tanase, R. Coehoorn, P. Bobbert, P. Blom, D. de Leeuw and M. Michels, *Phys. Rev. Lett.*, 2005, **94**, 206601.
- [222] D. S. Sivia and J. Skilling, in *Data Analysis*, Oxford University Press, 2006, ch. 2, pp. 14–34.
- [223] L. Schneider and M. Müller, *Macromolecules*, 2019, **52**, 2050–2062.
- [224] M. Doi and S. Edwards, in *The Theory of Polymer Dynamics*, New York: Oxford University Press, 1986, ch. 9, pp. 324–343.

- [225] M. Laradji, H. Guo and M. Zuckermann, *Physical Review E*, 1994, **49**, 3199–3206.
- [226] F. Detcheverry, H. Kang, K. Daoulas, M. Müller, P. Nealey and J. de Pablo, *Macromolecules*, 2008, **41**, 4989–5001.
- [227] M. Schwab and B. Stühn, *Phys. Rev. Lett.*, 1996, **76**, 924–927.
- [228] E. Dormidontova and T. Lodge, *Macromolecules*, 2001, **34**, 9143–9155.
- [229] P. Kordt, J. van der Holst, M. A. Helwi, W. Kowalsky, F. May, A. Badinski, C. Lennartz and D. Andrienko, *Adv. Funct. Mater.*, 2015, **25**, 1955–1971.
- [230] D. Andrienko, in *Multiscale Concepts in Simulations of Organic Semiconductors*, Springer, 2018, pp. 1–12.
- [231] D. L. Cheung and A. Troisi, *Phys. Chem. Chem. Phys.*, 2008, **10**, 5941–5952.
- [232] G. Fredrickson, *Macromolecules*, 1987, **20**, 2535–2542.
- [233] A. Hariharan, S. Kumar and T. Russell, *J. Chem. Phys.*, 1993, **99**, 4041–4050.
- [234] S. Anastasiadis, T. Russell, S. Satija and C. Majkrzak, *Phys. Rev. Lett.*, 1989, **62**, 1852–1855.
- [235] G. Krausch, *Mater. Sci. Eng.*, 1995, **R14**, 1–94.
- [236] M. Irwin, R. Hickey, S. Xie, S. So, F. Bates and T. Lodge, *Macromolecules*, 2016, **49**, 6928–6939.
- [237] S. B. Darling, *Energy Environ. Sci.*, 2009, **2**, 1266–1273.
- [238] F. Liu, Y. Gu, J. Jung, W. Jo and T. Russell, *J. Polym. Sci. Pol. Phys.*, 2012, **50**, 1018–1044.
- [239] D. Kipp, R. Verduzco and V. Ganesan, *Mol. Syst. Des. Eng.*, 2016, **1**, 353–369.
- [240] J. Zhang, H. Meyer, P. Virnau and K. Daoulas, *to be submitted*.
- [241] L. Dai, C. B. Renner and P. S. Doyle, *Macromolecules*, 2014, **47**, 6135–6140.
- [242] L. Dai, B. C. Renner and P. S. Doyle, *Phys. Rev. Lett.*, 2015, **114**, 037801.
- [243] A. Y. Grosberg, *Phys. Rev. Lett.*, 2000, **85**, 3858–3861.

- [244] V. Peter, K. Yacov and K. Mehran, *J. Am. Chem. Soc.*, 2005, **127**, 15102–15106.
- [245] P. J. Flory, *Statistical Mechanics of Chain Molecules*, Oxford University Press, 1988.
- [246] J. P. Wittmer, P. Beckrich, H. Meyer, A. Cavallo, A. Johner and J. Baschnagel, *Phys. Rev. E*, 2007, **76**, 011803.
- [247] J. P. Wittmer, P. Beckrich, A. Johner, A. N. Semenov, S. P. Obukhoov, H. Meyer and J. Baschnagel, *EPL*, 2007, **77**, 56003.
- [248] A. Y. Grosberg and Y. Rabin, *PRL*, 2007, **99**, 217801.
- [249] P. Pieranski, S. Przybyl and A. Stasiak, *Eur. Phys. J. E*, 2001, **6**, 123–128.
- [250] J. P. Wittmer, P. Beckrich, H. Meyer, A. Cavallo, A. Johner and J. Baschnagel, *Phys. Rev. E*, 2007, **76**, 011803.
- [251] J. Glaser, J. Qin, P. Medapuram and D. C. Morse, *Macromolecules*, 2014, **47**, 851–869.
- [252] A. J. Clark, J. McCarty and M. G. Guenza, *J. Chem. Phys.*, 2013, **139**, 124906.
- [253] T. Ohkuma, K. Kremer and K. Daoulas, *J. Phys.: Condens. Matter*, 2018, **30**, 174001.
- [254] M. L. Mansfield, *Macromolecules*, 1994, **27**, 5934–5936.
- [255] C. C. Adams, *The Knot Book: An Elementary Introduction to the Mathematical Theory of Knots*, American Mathematical Society, 2004.
- [256] P. Virnau, *Physics Procedia*, 2010, **6**, 117–125.
- [257] C. Livingston, *Knot Theory*, American Mathematical Society, 1993.
- [258] J. Hoste, M. Thistlethwaite and J. Weeks, *Math. Intell.*, 1999, **20**, 33–47.
- [259] J. T. Siebert, A. N. Kivel, L. P. Atkinson, T. J. Stevens, E. D. Laue and P. Virnau, *Polymers*, 2017, **9**, 317.
- [260] J. W. Alexander, *Trans. Amer. Math. Soc.*, 1928, **30**, 275–306.
- [261] R. Auhl, R. Everaers, G. S. Grest, K. Kremer and S. J. Plimpton, *J. Chem. Phys.*, 2003, **119**, 12718–12728.
- [262] L. A. Moreira, G. Zhang, F. Müller, T. Stühn and K. Kremer, *Macromol. Theory Simul.*, 2015, **24**, 419–431.

- 
- [263] G. Zhang, L. A. Moreira, T. Stühn, K. Daoulas and K. Kremer, *ACS Macro Lett.*, 2014, **3**, 198–203.
- [264] G. Zhang, T. Stühn, K. Daoulas and K. Kremer, *J. Chem. Phys.*, 2015, **142**, 221102.
- [265] L. Tubiana, A. Rosa, F. Fragiaco and C. Micheletti, *Macromolecules*, 2013, **46**, 3669–3678.





# Curriculum Vitae

Name: Jianrui Zhang

Age: 29

Place of birth: Shanxi, China

Email: Jianrui.Zhang@mpip-mainz.mpg.de

Address: Jakob-Welder-Weg 40, 55128, Mainz, Germany

---

## Education

### PhD in nature of science

Max-Planck-Institute for Polymer Research

Prof. Kurt Kremer's group

Thesis title: "Studying polymeric materials with mesoscopic models. Focus: multiscale properties"

08.2016 until now  
Mainz, Germany

### Master of Dynamic Engineering and Engineering Thermo-physics

University of Science and Technology Beijing (USTB)

School of Mechanical Engineering

Thesis title: "Thermal properties of MOFs-based phase change materials"

Cumulative GPA: 3.78/4.0

09.2013-01.2016

Beijing, China

### Bachelor of Thermal Energy and Dynamic Engineering

University of Science and Technology Beijing (USTB)

School of Mechanical Engineering

Thesis title: "Thermal conductivity of cubic boron nitride (cBN) nano-film"

Cumulative GPA: 3.84/4.0

09.2009-06.2013

Beijing, China

## Honours and Awards

### Honours:

"Wang Buxuan" Excellent Academic Paper of Young Scientist, Second Prize

2015

Academic Speech Competition of Engineering Thermophysics Society, Second Prize

2015

Merit Student of USTB

2010 ~ 2014

Outstanding graduate of USTB

2013

Outstanding Student Leader of USTB

2011

### Scholarships:

National Scholarship

2015

Jian Long scholarship

2014

Third class scholarship of people

2012 ~ 2013

Elite scholarship of USTB

2011

Top class scholarship of people

2010